8-1-2018

Computational Study of Desalination by Membranes

Mustafa USTA
Lehigh University, mmmustafausta@gmail.com

Computational Study of Desalination by Membranes

by

Mustafa Usta

Presented to the Graduate and Research Committee

of Lehigh University

in Candidacy for the Degree of

Doctor of Philosophy

in

Mechanical Engineering

Lehigh University

August 2018

DISSERTATION SIGNATURE SHEET

Approved and recommended for acceptance as a dissertation in partial fulfillment of the requirements for the degree of Doctor of Philosophy.

Date

Dr. Alparslan Oztekin
Dissertation Director

Accepted Date

Committee Members:

Dr. Alparslan Oztekin

Dr. Edmund Webb III

Dr. Jacob Kazakia

Dr. Xuanhong Cheng

Acknowledgements

I would like to express my highest possible appreciation to my advisor Dr. Alparslan Oztekin, who puts tremendous effort to perfect my core understanding of the research and professional development. His unique communication and attitude broadened not only my research but also other aspects of my life.

I would also like to thank the doctoral committee members Dr. Edmund Webb, Dr. Jacob Kazakia, and Dr. Xuanhong Cheng for their insightful advise and comments which widens the perspective of this research.

I do not know how much I can thank to Dr. Ali Anqi, who provides his endless and immense support in terms of research and makes this dissertation possible.

Nevertheless I am also grateful to many friends for sharing their valuable time and helping me to solve many issues I face during my research.

I felt and will always feel eternal gratitude to my wife Merve for her endless support and patience during this arduous Ph.D. study. I would also thank my five-months old son Mahir Alp for sharing his unwitting but precious support. Very special gratitude goes out to my parents and my siblings who have supported me along the way.

Contents

List of Tables

List of Figures

Nomenclature

α	Liquid-solid contact angle
α_1	Turbulence closure coefficient
β	Turbulence closure coefficient
β^*	Turbulence closure coefficient
$\Delta\pi$	Osmotic pressure difference
Δp	Transmembrane pressure difference
Δ	LES subgrid scale filter size
δ	Membrane thickness
ϵ	Turbulence dissipation rate
γ	Turbulence closure coefficient
γ_i	Activity coefficient
γ_{ls}	Liquid surface tension
κ	Osmotic pressure coefficient
λ	Mean free path
μ	Dynamic viscosity
μ_i	Chemical potential
μ_t	Turbulent eddy viscosity
μ_{sgs}	Subgrid scale eddy viscosity
ν	Kinematic viscosity
Ω	Vorticity magnitude

ω	Specific turbulent dissipation rate
ϕ	Product recovery rate
π	Osmotic pressure
ρ	Density
σ	Molecule collision diameter
$\sigma_{\omega 2}$	Turbulence closure coefficient
σ_{ω}	Turbulence closure coefficient
τ	Membrane tortuosity
τ_w	Wall shear stress
τ_{ij}	Reynolds stress tensor
τ_{max}	Maximum wall shear stress
θ	Temperature polarization coefficient
ε	Membrane porosity
ε_s	Membrane surface porosity
φ	Concentration polarization coefficient
$\vec{n}$	Surface normal vector
$\vec{V}$	Velocity vector
A	Water permeability
A_c	Cross-section area
B	Salt permeability
c	Salt concentration
c_0	Inlet salt concentration
c_b	Bulk salt concentration
c_f	Feed salt concentration
C_k	k-equation model constant
c_m	Membrane surface concentration

c_p	Specific heat
C_s	Smagorinsky model constant
C_w	WALE model constant
C_ϵ	k-equation model constant
COP	Coefficient of performance
D	Diffusivity
d	Hydraulic diameter
f	Friction coefficient
F_1	k-ω SST model blending function
F_2	k-ω SST model blending function
G	Geometric factor
h_m	Local mass transfer coefficient
h_{fg}	Water vaporization enthalpy
J_k	Knudsen flux
J_t	Total molar flux
J_v	Viscous flux
k	Turbulent kinetic energy
k_B	Boltzmann constant
k_f	Thermal conductivity
K_i	Sorption coefficient
Kn	Knudsen number
L	Module length
L_{ij}	Leonard stress
LEP	Liquid entry pressure
M_w	Water molecular weight
N_t	Total mass flux

p	Pressure
p_d	Differential pressure
p_v	Vacuum pressure
P_w	Wetted perimeter
p_{sat}	Saturation pressure
Q_m	Total heat transfer
R	Gas constant
r_p	Membrane pore radius
r_{max}	Maximum membrane pore radius
S	Strain rate tensor
S_{ij}^*	Trace-less strain rate tensor
Sh	Sherwood number
T	Temperature
t	Time
T_f	Feed temperature
T_{sat}	Saturation temperature
U_{ave}	Uniform averaged inlet velocity
v_i	Molar volume
v_w	Suction rate
X	Mole fraction
$\dot{m}_i$	Inlet mass flow rate
$\dot{m}_m$	Product mass flow rate
$\overline{g}_{ij}$	Velocity gradient tensor

Abstract

Water desalination by membranes constitutes the majority of the low-quality water purification systems that extends across many different techniques. This study considers transport phenomena in reverse osmosis (RO) and vacuum membrane distillation (VMD) modules using computational techniques. Reverse osmosis is a pressure-driven separation method using semi-permeable membranes featuring nanoporous structures. Vacuum membrane distillation is another emerging separation method relying on the temperature difference across the microporous hydrophobic membranes.

The membrane separation process intrinsically gives rise to temperature polarization (TP) and concentration polarization (CP) which could be severe limitations in these systems. To eliminate these polarizations and increase the module performance various design adaptations are suggested, and the effectiveness of this modifications are investigated using incompressible laminar/turbulent steady/unsteady computational fluid dynamics simulations. Fully coupled membrane transport models, which is Solution-Diffusion model for RO and Dusty Gas model for VMD, are employed where the local flow properties - concentration, temperature, pressure, and suction rate - are implicitly solved along the membrane surface to predict the permeate flux accurately.

It is shown how a simple design adaptation is achieved by twisting the hollow fiber membrane module that creates desirable flow structures result in dramatic per-

formance enhancement of hollow fiber membrane (HFM) RO water desalination modules. Twisted HFM bundles induce swirling flow structures inside desalination modules that increase momentum mixing throughout. It is found that the twisted HFM module mitigates concentration polarization (CP) effects and increases transmembrane permeate flux by $5-9\%$ for three flow rates considered. Frictional energy losses and increased pumping power associated with this subtle design alteration are small relative to projected gains in clean water production and there are in principle no additional required components associated with this geometry.

Complex nature of the permeate transport through the hydrophobic membranes in VMD process is modeled, and the effect of membrane properties and spacers on the TP and CP mitigation are explored. Large-Eddy Simulations (LES) are employed to gain more insight into the unsteady nature of the flow phenomena. It is found that coupling not only the local temperature but also the local concentration along the membrane surface affects the permeate flux since elevated concentration reduces the water vapor pressure. Membrane pore size is the dominant membrane parameter which mandates the true transport mechanisms. TP and CP are more pronounced in higher feed temperatures, and spacers dramatically mitigate these polarizations by inducing turbulent and momentum mixing. Submerging the spacers into feed channel also increases the pressure drop which is a potential threat for membrane wetting so that it needs to be examined along with other performance criteria while designing an optimum VMD module.

Chapter 1

Introduction

1.1 Motivation

With an increase in the world population and decrease in the water resources, water scarcity becomes one of the major issues we started to face today and expected to get even worse in the near future in the regions human population intensified. When we also consider the fact that the demand for water per person is also doubling at every 20 years, the potential remedies have to emerge to slow down the transition to drought. As an essential measure, the water usage should be decreased, and clean water production should be increased to deal with the mismatch between demand and supply. Increasing the supply side of the scenarios has gained significant momentum, and different techniques are invented to increase the quality of existing low-quality water such as wastewater and seawater. One way to categorize the existing methods is based on the driving forces - temperature, electrical, and pressure. To elucidate the implementation of these driving forces to the practical applications/processes, the methods can be categorized as thermal desalination, membrane desalination or combination of both. Membrane desalination and its combination with thermal de-

salination constitute the majority of water desalination.

Membrane separation technologies have broadened the horizons of desalination processes by sidestepping the hurdle of solution heating above the boiling temperatures, common to many water purification processes, thereby ushering in the emergence of new freshwater production systems. The developing manufacturing capabilities of synthetic membranes, simply a porous medium, gave rise to a wide range of membranes used in commercial applications. Membranes are constructed in either flat sheet or hollow fiber form to be used in different types of desalination methods. They basically separate the water from a feed mixture solution by means of concentration, temperature or pressure differences where forward osmosis, reverse osmosis, and membrane distillation are corresponding techniques, respectively. Although these methods are widely used in commercial applications, there are many challenges waiting for a resolution for better systems. Concentration polarization, temperature polarization, and fouling arouse as the main issues that limit the operational performance of these systems. It is considered that modification and optimization of these modules along with an accurate computational methodology has a significant potential to improve the performance of these systems.

1.2 Reverse Osmosis

Reverse osmosis is one of the widely used membrane desalination method driven by the pressure difference across a semi-permeable synthetic membrane. To be able to understand the mechanism it is better to start with naturally occurring osmosis process. As seen in the Figure 1.1a, when we place a saline solution and pure water separated by a semi-permeable membrane, the water passes through the membrane and migrates to the higher concentrated side by the effect of chemical potential.

The critical detail which makes this process possible is that water molecules are significantly smaller than Na^+ and Cl^- ions dissolved in the water. Keeping the membrane pore size smaller than these ion diameters will assure the selective diffusion of solvent. As the process continues, the solution keeps rising on its side of the u-shaped tube column until mechanism reaches to an equilibrium state. When the system reaches to an equilibrium condition, illustrated in Figure 1.1b, the difference in the height of both side constitutes the osmotic pressure.

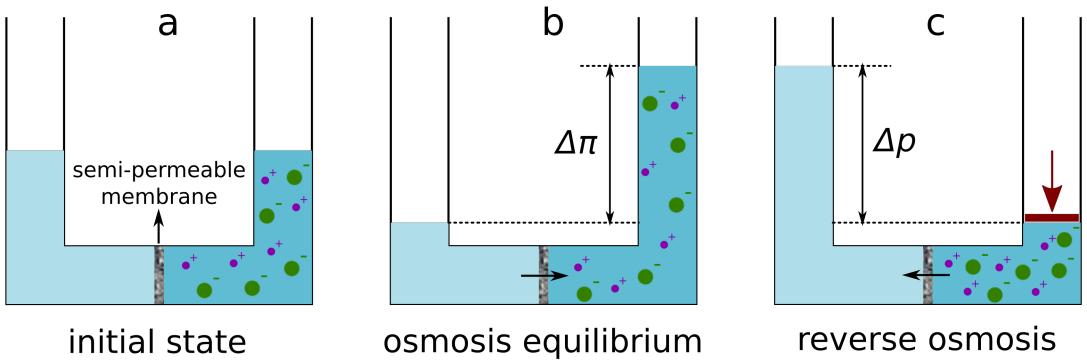

Figure 1.1: Reverse osmosis principle diagram, (a) initial state, (b) osmosis equilibrium, and (c) reverse osmosis.

When pressure is applied to the right side, illustrated in Figure 1.1c, that is larger than its osmotic pressure, clean water is removed from the solution and passes through a semi-permeable membrane while dissolved salts, and other impurities are left behind. This process is called reverse osmosis (RO), and it is a dominant method for water desalination because it can be scaled up to very large systems to produce mass amount of clean water to meet the demand.

Reverse osmosis desalination modules are usually constructed in two different configurations; spiral wound membrane modules (see Figure 1.2a) (SWMM) using flat sheet membrane and hollow fiber membrane module (see Figure 1.2b) (HFMM) using hollow fiber membranes, as evident by the name. In the spiral wound membrane

modules, the membranes are enveloped and attached to product channel located at the center. The same process can be applied to the multiple envelopes by separating with spacers and coiling around the center product channel. In the hollow fiber membrane module, thousands of fibers are packed as a bundle and placed in tube shell. Based on the desired flow configuration, feed inlet/outlet and product outlet locations vary accordingly.

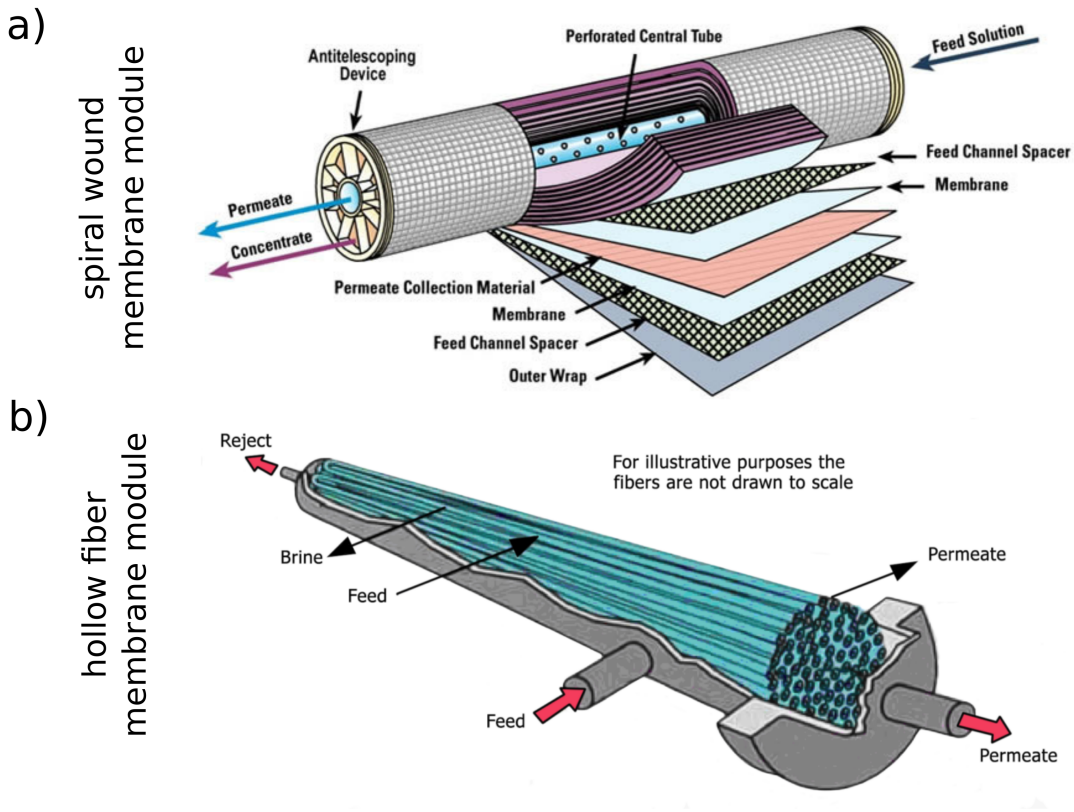

Figure 1.2: Reverse osmosis desalination modules, (a) spiral wound membrane module and (b) hollow fiber membrane module.

During clean water production, the salts, organic, and inorganic molecules left behind tend to congregate along membrane surfaces if the surrounding flow is unable to carry them away, which makes the local solute concentration in these regions very high relative to the bulk flow. As operation continues, particle accumulation along

membrane surfaces turns to fouling and scaling, which will eventually prevent clean water production altogether. In that case, the operation must be interrupted to flush away the deposited crusts, or they must be removed by other physical means prior to continuing clean water production.

1.3 Vacuum Membrane Distillation

Vacuum membrane distillation is a unique method, which combines the advantages of membrane desalination and thermal desalination, in terms of separating the water in low temperatures with the help of hydrophobic membranes. The inclusion of the microporous membrane to the operation is the major difference makes this method entirely apart from pervaporation [4]. This separation process creates a high and low water vapor pressure across the microporous membrane, to drive the water vapor through the cavities of the membrane. It should be added that water vapor pressure is a function of temperature so that calling temperature as the driving force still becomes a valid description. The primary advantage in this method comes from the hydrophobicity of the membranes where the liquid solution cannot penetrate into the membrane, and just water vapor passes through. This enables the pore size of the membrane to be considerably larger, in the ranger of $0.2 - 1\ \mu m$.

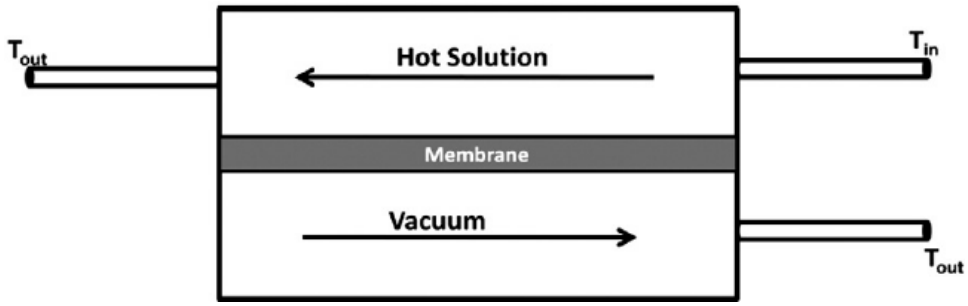

Figure 1.3: Vacuum membrane distillation diagram [1].

Figure 1.3 shows the schematic of flow configuration in a typical vacuum membrane distillation module. The heated feed solution comes into the module, and vacuum pressure is applied to the other side of the membrane. As the water vapor pressure in the feed side of membrane exceeds the applied pressure on the production side, water vapor start to evaporate and migrate to the vacuum side of the channel. Once the water vapor is collected in the vacuum channel, it is transferred to condensation unit to produce pure liquid water.

In the vacuum membrane distillation, mechanical properties of the membrane are not demanding, and there is no need to increase the hydrostatic pressure. Thus, the operating cost decreases considerably when compared to other desalination methods. Furthermore, the applied vacuum in the product side decreases the heat conductivity and performs like an isolator which limits the conductive heat losses substantially.

Evaporation heat losses constitute the major part of the heat transfer through membranes. The amount heat transferred to evaporation is monotonically related to permeate flux. Therefore, the increase in the vapor flux results in lower temperatures at the membrane surface. Such behavior is defined as the temperature polarization which is the major issue to be addressed in these systems. Quantification of temperature polarization and other relevant details is discussed in Chapter 2.3.2.

1.4 Literature Review

Reverse osmosis has been widely used to produce clean water by desalination for over 50 years. The modules, using a flat sheet and hollow fiber membranes, have been designed to separate water from different levels of saline solutions. To improve the performance of these systems, many researchers investigated the concentration polarization, fouling, scaling, and other phenomena occurring in these modules. While

most of the studies revolve around the experimental exploration, the computational investigation has gained momentum as well thanks to the increasing computational capabilities and advancing mathematical models describing the physical phenomena. In addition to reverse osmosis, another relatively new method, vacuum membrane distillation, started to emerge with the fundamental studies in this field dating back to 1990s [4]. Since then, many experimental studies and recently computational studies have attempted to uncover the physics of these systems and seek ways to scale up these modules for commercial utilization. Although concentration polarization and fouling are still an issue for these systems, there are other challenges, such as temperature polarization and membrane wetting, under investigation by many researchers. The state-of-the-art of reverse osmosis and vacuum membrane distillation process are detailed in the following two sections, respectively.

1.4.1 Reverse Osmosis

Regions along HFM surfaces where the local salt concentration is large relative to the bulk are said to exhibit concentration polarization (CP), which is a precursor to fouling. Herein, we focus on CP mitigation in order to abate losses due to fouling. One way to mitigate CP is by increasing the momentum mixing in the module, which increases mass transport of accumulated retentate along membrane surfaces back into the bulk flow and disrupts local concentration fields along and near to HFM surfaces [5]. The increased momentum mixing appears to be an effective method of CP mitigation because of the strong correlation between high wall shear stress and low CP, independent of membrane type [6–11]. The importance of accurately representing local salt concentrations in numerical studies is well exemplified by Marcovecchio et al. [12], who presented a model to predict the permeation performance in HFM desalination modules by means of appropriate flow and concentration field discretization. Salt

concentration accumulation along HFM surfaces was examined, and it was reported that the transmembrane concentration gradient depends on the feed-side surface concentration as well as the permeate side surface concentration, which varies along the length of the membrane. The production-side salt concentration was nearly uniform but nonetheless decreased slightly along the module length.

Accurately capturing local changes in concentration near to and along HFM surfaces is also very important because fouling has been shown to increase the system pressure drop, thereby demanding increased pumping power. Ghidossi et al. [13] conducted numerical simulations to elucidate the relationship between pressure drop and operating/design parameters such as inlet velocity, inlet pressure, internal diameter, and permeability for an HFM ultrafiltration system. Their model relates the pressure drop across the module length, or energy loss, to membrane fouling. The model they employed is experimentally validated and suggests that higher flow speeds increase system performance. Villafafila and Mujtaba [14] also discussed the relation of fouling to pressure drop. They carried out simulations using algebraic equations to optimize design and operating parameters for HFM water desalination modules. In that study, simulations were conducted by specifying the output of one HFM module as the input of a subsequent module. This approach helped them understand the physical behavior of an optimal parameter selection for the RO-driven water desalination process using HFMs. However, their algebraic model must be improved in order to incorporate the effects of concentration polarization accurately.

Our approach to increasing momentum mixing throughout the module involves the introduction of a twist to the traditional HFM module design. Others have studied similar design alterations and varying operating parameters. Pak et al. [15] employed finite difference methods to solve for the flow and concentration fields in a two-dimensional HFM to investigate the effects of different operating conditions on CP.

They reported that concentration boundary layer thickness decreases with increasing Reynolds numbers. Anqi et al. [16] investigated the effect of various flow speeds and HFM arrangements in modules of the radial flow configuration. They carried out steady-state and transient CFD simulations in two-dimensional domains using the k-ω Shear Stress Transport (SST) turbulence model. As for the membrane transport model, they have successfully implemented a fully coupled Solution-Diffusion model to predict the permeate flux. They found that transient effects profoundly influence CP and higher wall shear stress is related to lower CP. Motevalian et al. [17] used CFD simulations to determine the flow characteristics inside a twisted, elliptical, and helically-coiled cylindrical single hollow tube for Reynolds number of up to 200. In that study, the flow field was characterized, but not the concentration field, and special attention was given to the wall shear stress and vorticity. Also, they considered no-slip and no-penetration boundary condition by neglecting the permeate suction along the membrane surfaces. They found that twisted, elliptical tubes provide more wall shearing than its helically-coiled and straight counterparts, but with the penalty of a 50% greater pressure drop. Motevalian et al. showed that these geometric tube adaptations induce flow instabilities and vortical activity which are expected to enhance mass transfer by re-suspending particles accumulated along membrane surfaces back into the bulk flow and facilitate more clean water passage through membrane surfaces. Teoh et al. [18] experimentally investigated the effect of twisted, braided, and baffled HFMs on the heat-transfer coefficient for direct contact membrane distillation modules. They reported 36% flux enhancements for braided and twisted HFMs without any additional mixing promoters.

1.4.2 Vacuum Membrane Distillation

The development of hydrophobic polytetrafluoroethylene (PTFE) membranes adds a new dimension to water treatment methods and allows the feed water to be purified by heating under the boiling point. Membrane distillation (MD) is a membrane separation process in which the transmission of water vapor through a hydrophobic membrane is achieved by thermally driven differences in partial pressure on the feed and permeate sides. MD has been studied using a variety of techniques such as direct contact membrane distillation (DCMD), air gap membrane distillation (AGMD), sweeping gas membrane distillation (SGMD), and vacuum membrane distillation (VMD).

In the last two decades, researchers have focused more on studying MD. El-Bourawi et al. [19] have reported that the increase of the literature number in MD since the 1990s, and they showed the rapid increase of the published papers in the 2000s. Most of these research papers have studied the application of MD in water desalination [19]. Lawson and Lloyd [4] have shown that the Dusty Gas Model (DGM) describes well the mass transfer in MD process. By applying the Dusty Gas Model, the mass transport through the membrane pores takes place by on three mechanisms: Knudsen diffusion, molecular diffusion or viscous diffusion. In some cases, the mass diffuses by a combination of two all three mechanisms [4, 20, 21]. Due to the nature of the process in MD, the heat transfer simultaneously associates the mass transfer. The mass and heat transfer are interdependent in MD. Schofield et al. [22–24] conducted theoretical and experimental studies to investigate MD process. The authors noticed that temperature polarization adversely influences MD process, and tubular and hollow fiber membranes exhibit less temperature polarization than flat sheet membranes [22]. They also noticed that the application of vacuum pressure on the permeate side increases the temperature polarization on the feed side [23]. Gryta and Barancewicz [25] experimentally studied the membrane morphology and wettability. The wetta-

bility decreases as the membrane hydrophobicity level increases. The authors also noticed that the permeate flux improves by reducing the membrane thickness. Song et al. [26] performed an experiment to study the effect of the feed concentration and temperature on the permeate production. They observed that the feed concentration and temperature affect the permeate flux. In fact, the membrane thickness effect differs by the membrane material. Mourgues et al. [27] investigated MD process using hydrophobic metallic membranes. The experiment and simulations showed the permeate flux increases when the metallic membrane is thicker. Qtaishat et al. [28] analyzed the heat and mass transfer in the DCMD. The mass transfer obeys Knudsen diffusion mechanism when Knudsen number, Kn, greater than 1. The molecular diffusion mechanism dominates if $Kn < 0.01$. For $0.01 < Kn < 1$, the mass diffusion is a combination between Knudsen mechanism and molecular mechanism in the direct contact configuration. Martinez et al. [29] used two different membranes and two module designs. In the theoretical analysis, heat and mass transfer are calculated by the Dusty Gas Model and film theory. The results were validated by experimental measurements. Martinez et al. recommended that the production flux enhance when both membrane properties and module design are optimized. To help evaluate the energy consumption in membrane distillation, Criscuoli et al. [30] conducted experiments for DCMD and VMD. The study found that VMD consumes less energy to produce fresh water than DCMD.

Different MD configurations have advantages and disadvantages. Air gap membrane distillation configuration operates at high thermal efficiency, but it yields low permeate flux [31]. Consequently, AGMD is less attractive than direct contact membrane distillation and vacuum membrane distillation. Few researchers have studied AGMD. Guijt et al. [32] have theoretically analyzed the heat and mass transfer in air gap membrane distillation by considering the three diffusion mechanisms: Knudsen

diffusion, molecular diffusion, and viscous diffusion. According to Liu et al. [33] the operating conditions and membrane properties affect the permeate flux more than the concentration polarization in AGMD. The concentration polarization has a limited effect which is attributed to the low permeate flux. The other MD configurations might behave differently. Sweeping gas membrane distillation has the least attention from researchers. The design of the SGMD is influenced by the process where the high volume flow rate of inert gas in the permeate side requires huge condenser to extract the water vapor [31, 34].

Vacuum membrane distillation has a wide range of applications [35–46]. Specifically, VMD approach adopts a liquid feed mixture in the upstream of the membrane and a vacuumed vapor product in the downstream of the membrane. In order for the process to remain operational, the temperature at the feed side of the membrane surface has to be higher than the saturation temperature corresponding to applied vacuum pressure. The performance of VMD modules is significantly affected by membrane properties such as membrane pore size, porosity, and thickness [21, 31]. Izquierdo-Gil and Jonsson [47] carried a theoretical and experimental investigation to evaluate the effects of operating conditions and membrane material on the permeate flux. The theoretical analysis considered Knudsen diffusion and viscous diffusion and neglected the molecular diffusion due to the air absence by vacuum. Izquierdo-Gil and Jonsson recorded that the flux exponentially increases as the feed temperature rises. They also reported some deviation between the theoretical model and the experimental results. Similar findings were reported by Mengual et al. [48] and conducted a comparison between the experimental results and the empirical correlations of heat transfer. The experimental results of the heat transfer deviate from the empirical correlations results, especially at the laminar flow regime.

Computational fluid dynamics (CFD) has become an effective and efficient method

for designing and evaluating performance. CFD has the capability of solving simultaneous phenomena such as heat and mass transfer in MD where temperature, concentration and permeate are interdependent [4]. Researchers have deployed this method to evaluate and predict the performance of MD modules in different approaches. The majority of the CFD studies in the literature have considered only the momentum and energy equations without the mass transport [49–57]. At the membrane surface, the absence of concentration was replaced by empirical correlation. Zuo et al. [57] considered the optimization of four design and operation parameters feed temperature, hollow fiber length, feed volume flow rate, vacuum pressure of hollow fiber VMD modules by means of numerical approach. They reported that temperature significantly affects the permeate flux rate and 38.1% reduction in the water production cost is estimated for an optimized system. Zhang et al. [58] employed three-dimensional CFD simulations to study the effects of operating conditions and module dimensions on heat transfer process in hollow fiber VMD. They found out that thermal efficiency is very sensitive to feed temperature and increasing fiber length decreases the thermal efficiency considerably. Mericq et al. [59] experimentally investigated further distillation of seawater reverse osmosis brines by means of flat-sheet VMD. Although the scaling of calcium crystals over the membrane surface because of the highly concentrated reverse osmosis brines, the coupling of two methods increases the overall product recovery rate considerably. Liu et al. [60] have conducted numerical simulations for hollow fiber vacuum membrane distillation. The simulations considered momentum, energy and mass transport. The membrane was treated as a functional surface, but the concentration effect on the vapor pressure was not involved in the boundary condition equations of the membrane.

In order to predict permeate flux and membrane distillation module performance, including pressure drop and polarizations, more accurate modeling for momentum,

energy, and concentration is required. The mass flux model for vapor transport through the membrane needs to involve simultaneously the membrane properties and the flow properties - temperature, permeate flux and concentration - along the membrane surface.

1.5 Research Objectives

The aforementioned studies, mostly experimental, in Reverse Osmosis and Membrane Distillation desalination processes provide insight into the complex nature of separation by membranes. With the contribution of simplified computational studies, it is revealed that fluid dynamics of the membrane module has an undeniable effect on the membrane separation performance and significant improvements can be achieved over the existing module designs by modeling and computationally investigating the membrane separation phenomena. The overall objective of this study is to implement proper flow and more accurate membrane transport models to computationally investigate and improve the performance of common desalination modules. The explicit research objectives of this study are as follows.

(1) *Investigate the effect of hollow fiber membrane arrangement and flow speed on the performance of reverse osmosis hollow fiber membrane for cross-flow configuration.* This study introduces a perpendicularly arranged hollow fiber membrane bank and computationally characterizes the flow and concentration field in the three-dimensional domain to find an optimum design for hollow fiber membrane arrangement.

(2) *Design a novel twisted hollow fiber membrane RO module and investigate its' effectiveness.* This study shows how a simple novel design adaptation elevates the momentum mixing in the hollow fiber membrane modules to improve existing

axial-flow configured hollow fiber membrane desalination modules and explores the potential performance gain provided by the proposed design adaptation.

(3) *Derive and implement a mathematical model to predict the permeate flux in the vacuum membrane distillation process.* A new membrane transport model derivation is achieved that couples the local flow properties -temperature, salt concentration, suction rate, and pressure- along the membrane surface, first in the literature, to predict the permeate flux accurately in VMD process.

(4) *Study the effect of PTFE membrane properties on the performance of vacuum membrane distillation module.* In this project, a parametric study is carried out to understand the effect of membrane properties on the permeate flux performance and polarization issue. The simulations are designed for 27 different scenarios to investigate the effect of each parameter separately.

(5) *Study the effect of spacers, feed temperature, and feed flow rate on the performance of vacuum membrane distillation module.* In this project, submerged spacers are proposed to mitigate concentration and temperature polarization occurring in these systems. Time-depended high fidelity LES simulations are designed to uncover the fundamental physics regarding the effect of turbulent mixing and temporal flow structures on the polarization mitigation.

1.6 Thesis structure

A brief description of the following chapters of this dissertation are given as follows.

Chapter 2 presents the details of conservations equations, turbulence models and membrane transport models used to accomplish this investigation. Chapter 3 discusses the computational methodology of the simulations. It starts with the dis-

cretization of both domain and equations then provides solver algorithms to address velocity-pressure coupling properly. Furthermore, it includes the basic information about OpenFOAM and finally lists the computational resources used. Chapter 4 and 5 include the results and discussion of the findings for reverse osmosis and vacuum membrane distillation, respectively. Specifically, Chapter 4 introduces a novel twisting approach to HFM modules and Chapter 5 presents and discusses results of vacuum membrane distillation simulations by coupling the suction rate, temperature, and concentration, first time in the literature, along with the membrane surface. Finally, Chapter 6 summarizes the findings through these investigations and provides a projection for the future work.

Chapter 2

Mathematical Model

2.1 Conservation Equations

Incompressible, laminar and Newtonian fluid motion is governed by the Navier-Stokes equations. Conservation of mass and momentum equations yield:

$$\nabla \cdot \vec{V} = 0 \tag{2.1}$$

$$\rho \left[\frac{\partial \vec{V}}{\partial t} + \left(\vec{V} \cdot \nabla \right) \vec{V} \right] = -\nabla p + \mu \nabla^2 \vec{V} \tag{2.2}$$

The equations governing solute mass transport through the feed channel is described by:

$$\frac{\partial c}{\partial t} + \left(\vec{\mathrm{V}} \cdot \nabla \right) c = D \nabla^2 c \tag{2.3}$$

In vacuum membrane distillation simulations in addition to the solute mass transport, energy transport has to evaluated accurately to determine temperature distri-

bution. The energy transport equation for transient incompressible flows is written as:

$$\frac{\partial T}{\partial t} + \left(\vec{\mathrm{V}} \cdot \nabla\right) T = \frac{k_f}{\rho c_p} \nabla^2 T \tag{2.4}$$

In the above, ρ is the binary mixture density, p is pressure, μ is viscosity, T is temperature, k_f is thermal conductivity of feed solution, c_p is specific heat, c is scalar salt concentration, and D is the diffusion coefficient. $\vec{V}$ is the velocity vector with components in the x, y, and z directions, respectively, which measure the channel length, height, and width.

2.2 Turbulence Modeling

In many diverse engineering applications, Computational Fluid Dynamics (CFD) emerge as a very crucial tool in determining characteristics of fluid flows. CFD essentially replaces the partial differential equations (PDE) governing the flows by a set of algebraic equations which can be solved using computers. The journey of understanding physical events that occur in the flow of fluids around and within specific objects depends on including but not limited to flow speed and complexity of the designated flow domain. A basic approach to classification of flows can be satisfied by considering laminar, transition to turbulent and fully turbulent flows.

Turbulent flows constitute most of the fluid flow which we encounter in many processes. It is characterized by velocity fluctuations in all directions and has an infinite number of degrees of freedom. Solving the Navier-Stokes equations analytically for such flows become one of the most impractical and expensive preference due to elliptic, nonlinear and coupled (pressure-velocity, temperature-velocity) nature of the

equations. Although the definition of turbulent flow is not clear, it can be identified by a number of characteristic futures such as irregularity, intermittency, three dimensional, diffusive, dissipative and continuum [61].

In a turbulent flow, numerically solving the all scales of motion requires the construction of a grid with an overwhelmingly higher number of nodes. Despite the tremendous development of computational capabilities over the several decades, accurate modeling and simulation of such flows have remained challenging, and in some cases, even inaccessible. Theoretically, Direct Numerical Simulations (DNS) provides all scales of the properties of interest. However, the realization of DNS in high Reynolds numbers and complex flows scenarios is inaccessible due to demanding computational resources. As we introduce turbulence modeling into the problem, there are several approaches, such as Large Eddy Simulations (LES) and Reynolds Averaged Navier Stokes (RANS), to make reasonable predictions in the flows where DNS information is not there. LES method introduces a filter - low pass, box, or Gaussian - and it models the scales of motion smaller than filter size and solves the large eddies. Such characteristic of the model essentially provides time-dependent predictions to capture the phenomenon in the flow unsteady in nature. For the modeling of sub-grid scales of motion, there are many approaches offering solutions for different types of problems. Another way to get some insight into the turbulent flows is RANS methods. It essentially decomposes the velocity into averages and fluctuating components and reforms the Navier-Stokes models by dropping the time dependency. The detailed description of these methods is discussed in the following sections, in the order of increasing complexity.

2.2.1 Reynolds Averaged Navier-Stokes Turbulence Models

Solving the conservation equations (2.1, 2.2, 2.3, 2.4) for the infinite number of scales becomes impractical for turbulent flows. In order to reduce the degree of freedoms, it is preferable to use Reynolds averaging. Reynolds averaging method decomposes any instantaneous property (whether a scalar or a vector), $\phi(x,t)$, which is a function of time and space, into a mean and fluctuating components as given by

$$\phi(x,t) = \Phi(x) + \phi'(x,t) \tag{2.5}$$

where the capital letter denotes the time average and the second term denotes the fluctuation of the property. For stationary turbulence, the average is calculated by

$$\Phi(x) = \lim_{\tau\to\infty} \frac{1}{\tau} \int_t^{t+\tau} \phi(x,t)dt \tag{2.6}$$

To obtain a stationary average τ needs to be much greater than the time scale of turbulent fluctuations. It is worth adding that, by definition, the average of the fluctuations is zero. Once the Reynolds decomposed properties used to derive NS equations the resultant set of equations are called the Reynolds Averaged Navier Stokes (RANS). The time-averaged continuity equation and Navier-Stokes equations read

$$\frac{\partial U_i}{\partial x_i} = 0 \tag{2.7}$$

$$\rho\frac{\partial U_i U_j}{\partial x_j} = -\frac{\partial P}{\partial x_i} + \frac{\partial}{\partial x_j}\left[\mu\left(\frac{\partial U_i}{\partial x_j} + \frac{\partial U_j}{\partial x_i}\right) - \rho\overline{u_i' u_j'}\right] \tag{2.8}$$

When equation 2.8 compared to equation 2.2, a new unknown term $\rho(\overline{u_i' u_j'})$ appears on the right side of the equation which is called the Reynolds stress tensor. It is required to introduce additional equations to close this problem, which is called closure

problem. This is the step where turbulence modeling comes on the stage to model Reynolds stress term. Some of the common turbulent models are seen in the Figure 2.1, in the order of increasing complexity.

- Algebraic (zero equation) models: mixing length (first order model)
- One equation models: k-model, μ_t-model (first order model)
- Two equation models: k-ε, k-kl, k-ω^2, low Re k-ε (first order model)
- Algebraic stress models: ASM (second order model)
- Reynolds stress models: RSM (second order model)

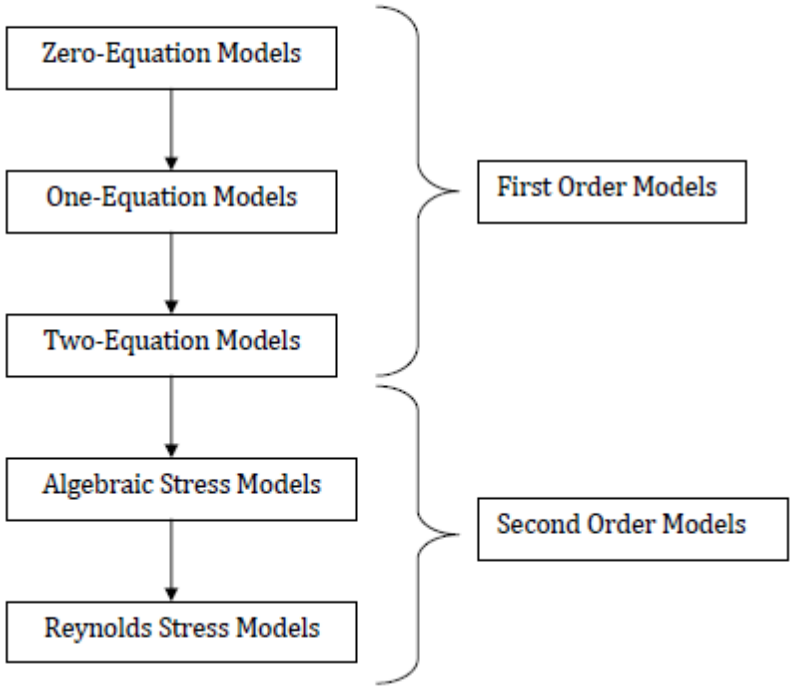

Figure 2.1: List of turbulence model for RANS closure problem.

First order models are defined and called as Eddy Viscosity Models (EVM) based on the analogy between laminar and turbulent flows. The eddy viscosity RANS models rely on the Boussinesq hypothesis,

$$\tau_{ij} = -\rho\overline{u_i' u_j'} = 2\mu_t S_{ij}^* - \frac{2}{3}\rho k \delta_{ij} \tag{2.9}$$

$$S_{ij}^{*} = \frac{\partial U_i}{\partial x_j} + \frac{\partial U_j}{\partial x_i} - \frac{2}{3}\frac{\partial U_k}{\partial x_k}\delta_{ij} \tag{2.10}$$

where u_i' is the ith component of the velocity field fluctuations, μ_t is turbulent eddy viscosity, k is the turbulent kinetic energy, and S_{ij}^{*} is the trace-less mean strain rate tensor. It has to be noted that $\frac{\partial U_k}{\partial x_k} = 0$ for incompressible flow.

As opposed to the Boussinesq hypothesis, second-order models directly employ the governing equations for the second-order moments. It overcomes the limits of first order models at the expense of solving additional transport equations. The additional cost of these methods has kept it less attractive result in less development against to first order models [62]. In the current study, a two-equation eddy viscosity model, k-ω Shear Stress Transport (SST), is employed to characterize the flow in low Reynolds numbers turbulent flows.

k-omega Shear Stress Transport Model

Menter's k-ω Shear Stress Transport model is a model that merges the k-ϵ and k-ω turbulence models to characterize the flows including boundary layer [63]. It essentially solves two transport equations; one for turbulent kinetic energy, k, and another for turbulence specific dissipation, ω, to account for history effects of convection and diffusion of turbulent energy. As a unique advantage of SST, it introduces a blending function to switch k-ϵ in free-stream regions and k-ω in near-wall regions so that it deals with adverse pressure gradients and flow separations reasonably. The equations governing the k and ω are described as

$$\frac{D}{Dt}(\rho k) = \tau_{ij}\frac{\partial u_i}{\partial x_j} - \beta^{*}\rho\omega k + \frac{\partial}{\partial x_j}\left[(\mu + \sigma_k\mu_t)\frac{\partial k}{\partial x_j}\right] \tag{2.11}$$

$$\frac{D}{Dt}(\rho\omega) = \tau_{ij}\frac{\gamma}{\nu_t}\frac{\partial u_i}{\partial x_j} - \beta\rho\omega^2 + \frac{\partial}{\partial x_j}\left[(\mu + \sigma_\omega\mu_t)\frac{\partial\omega}{\partial x_j}\right] + 2(1-F_1)\frac{\rho\sigma_{\omega 2}}{\omega}\frac{\partial k}{\partial x_j}\frac{\partial\omega}{\partial x_j} \quad (2.12)$$

where ν_t is the turbulent kinematic viscosity, F_1 is the blending function and β, β^*, σ_k, σ_ω, $\sigma_{\omega 2}$, and γ are closure coefficients. The turbulent eddy viscosity is computed from:

$$\mu_t = \frac{\rho\alpha_1 k}{\max(\alpha_1\omega, \Omega F_2)} \quad (2.13)$$

Here, Ω is the vorticity magnitude and α_1 is the closure coefficient. A detailed description of the model can be found in Ref [63].

2.2.2 Large Eddy Simulations Subgrid-Scale Models

Turbulence is an unsteady and three-dimensional phenomenon where the fluctuations occur in a wide range of length and time scales. These scales are strictly dependent on Reynolds number and flow characteristics and are required to be resolved for a complete solution of fluid dynamics which is called direct numerical solutions. Large eddy simulation method is a natural simplification of direct numerical simulations in a way that it offers a sub-grid model to govern the fluctuations of properties smaller than a length scale, δ and directly solves the motions of larger scales. The method was first proposed by Smagorinsky in 1963 [64] and explored by Deardorff in 1970 [65]. LES decreases the computational cost significantly while capturing unsteady nature of turbulence. In a turbulent flow, larger eddies carry most of the turbulence energy and the energy cascades to smaller scales. As the large eddies are anisotropic and responsible for most of the momentum transfer and mixing, LES provides accurate predictions when compared to RANS which governs the Reynolds stress with isotropic models.

The very first step to accomplish LES simulations is applying spatial and temporal

filters to Navier-Stokes equation to determine which scales to be solved or modeled. Using the Reynolds averaging analogy a property can be split up into a large-scale component and a sub-grid scale component which reads

$$\phi(x,t) = \overline{\phi}(x,t) + \phi'(x,t) \tag{2.14}$$

where $\overline{\phi}(x,t)$ is the resolvable larger eddies and $\phi'(x,t)$ is subgrid-scale eddies to model. By deriving the Navier-Stokes equation with this velocity decomposition, the filtered equation yields

$$\rho\left[\frac{\partial \overline{u}_i}{\partial t} + \frac{\partial}{\partial x_j}(\overline{u}_i\overline{u}_j)\right] = \frac{\partial \overline{p}}{\partial x_i} + \frac{\partial}{\partial x_j}\left[\mu\left(\frac{\partial \overline{u}_i}{\partial x_j} + \frac{\partial \overline{u}_j}{\partial x_i}\right)\right] - \rho\frac{\partial \tau_{ij}}{\partial x_j} \tag{2.15}$$

where τ_{ij} denotes the subgrid scale stress defined by eddy viscosity assumption which reads

$$\tau_{ij} = \overline{u_i u_j} - \overline{u}_i\overline{u}_j = -2\mu_{sgs}S^*_{ij} \tag{2.16}$$

Here, regarding the velocities, the first term stands for the random force produced by sub-grid scale exerted on the large scales and second term is responsible for the sub-grid scale Reynolds stresses. To close equation 2.15 different types of sub-grid scale (SGS) models, considering zero-equation or multiple equation approaches, have been developed.

Smagorinsky

Smagorinsky SGS model is one of the oldest approaches in terms of zero-equation (algebraic) eddy viscosity approach to calculate the sub-grid scale stress tensor. The turbulent eddy viscosity is defined as

$$\mu_{sgs} = \rho(C_s\Delta)^2 S \tag{2.17}$$

where $\Delta = (\Delta x \Delta y \Delta z)^{1/3}$ is the filter size determined by cubic root of cell volume, $S = \sqrt{(2\overline{S}_{ij}\overline{S}_{ij})}$ is the strain rate tensor. C_s is the Smagorinsky constant and it depends on the flow type. Tuning the C_s for different flow types is crucially important for the accuracy of the simulations. The major drawback related to this constant is that it may need to change locally which requires a dynamic approach. It is also realized that at near wall regions this model tends to over-predict the turbulent eddy viscosity due to the fact that second invariant of $\overline{S}$ lead to the non-physical behavior $\mu_{sgs} = O(1)$ at the wall.

Wall-Adapting Local Eddy-Viscosity (WALE) Model

Classical Smagorinsky formulation falls short in the regions where vorticity dominates the irrotational strain. Such behavior makes the Smagorinsky approach inaccurate at the vicinity wall boundaries in which the dominant deformation occurs. Wall adapting scheme basically adjust the calculation of strain rate by including the rotation rate tensor in the sub-grid scale viscosity formulation. This modification makes the model more sensitive the to both strain and rotation rate of the small turbulent structures. The Wall-Adapting Local Eddy-viscosity model for the eddy-viscosity reads as [66]:

$$\mu_{sgs} = \rho \Delta^2 \frac{(S^d_{ij} S^d_{ij})^{3/2}}{(\overline{S}_{ij}\overline{S}_{ij})^{5/2} + (S^d_{ij} S^d_{ij})^{5/4}} \tag{2.18}$$

$$S^d_{ij} = \frac{1}{2}\left(\overline{g}^2_{ij} + \overline{g}^2_{ji}\right) - \frac{1}{3}\delta_{ij}\overline{g}^2_{kk} \tag{2.19}$$

where, $\overline{g}_{ij} = \frac{\partial \overline{u}_i}{\partial x_j}$ is the velocity gradient tensor, $\overline{g}^2_{ij} = \overline{g}_{ik}\overline{g}_{kj}$, $\Delta = C_w(\Delta x \Delta y \Delta z)^{1/3}$ is the filter size, $\overline{S}_{ij}$ is the rate of strain tensor for the resolved scale, and C_w is the model constant.

k-Equation

So far in the Smagorinsky and WALE models, listed above, the turbulent kinetic energy is calculated based on the local equilibrium. If the resulting model coefficient leads to negative values tracking of the energy transfer between sub-grid scales and resolved scales becomes impossible. To address this issue, one-equation eddy-viscosity models are proposed to solve a separate transport equation for turbulent kinetic energy [67]. The k_{sgs} transport equation reads as:

$$\frac{\partial(\rho k_{sgs})}{\partial t} + \frac{\partial(\rho \overline{u}_j k_{sgs})}{\partial x_j} \frac{\partial}{\partial x_j} \left[(\mu + \mu_{sgs}) \frac{\partial k_{sgs}}{\partial x_j} \right] = -\rho \tau_{ij} : \overline{D}_{ij} - C_\epsilon \frac{\rho k_{sgs}^{3/2}}{\Delta} \tag{2.20}$$

where the operator : is a double inner product, ρ is the density, μ is the dynamic viscosity, and $\overline{D}_{ij}$ is the resolved-scale strain rate tensor. The terms in equation (2.20) are, starting from the left, the time derivative term, convective term, diffusion term, production term and dissipation term. Based on the resolved sub-grid turbulent kinetic energy the eddy-viscosity can be determined as:

$$\mu_{sgs} = \rho C_k \sqrt{k_{sgs}} \Delta \tag{2.21}$$

where C_ϵ and C_k are models constants and Δ is the filter size.

dynamic k-Equation

The dissipation rate and proportionality coefficient are set to be constant in a typical k-Equation SGS model. These limitations are removed by introducing a dynamic approach which adjusts the constants locally based on the local flow properties [68]. The basic idea behind this approach it that it applies a second filter, where the filter

size is larger than that of the grid size, to calculate Leonard stress reads as:

$$L_{ij} = \overline{\overline{u}_i \overline{u}_j} - \overline{\overline{u}}_i \overline{\overline{u}}_j \tag{2.22}$$

This approach provides better prediction in wall-bounded flow due to dynamic adjustment of model coefficients.

2.3 Membrane Transport Models

Membranes are selective barriers that allow the passage of certain component whereas it blocks or limits the other components. Such behavior is attractive for desalination application since it allows water molecules to pass while rejecting the passage of salt ions. Before integrating the membranes to the practical applications, the next concern would be identifying the proper model that predicts the amount of permeate passing through the membrane. Membrane transport models are an essential part of the computational investigation of desalination by membranes as it explores the transport mechanism and determines the corresponding permeate fluxes. The transport phenomena substantially change by the change in membrane properties such as pore size, porosity, and tortuosity.

Reverse osmosis and membrane distillation employ substantially different membranes which yield a significantly different transport mechanism. Reverse osmosis uses dense membranes that has nanoporous structures whereas membrane distillation requires hydrophobic membranes featuring microporous medium. To predict water permeation through the membrane, there are many models proposed for both reverse osmosis and membrane distillation. In the following two sections, the description of the models used in this study is provided.

2.3.1 Reverse Osmosis

Reverse osmosis is a pressure-driven process using a semi-permeable membrane that separates water from dissolved constituents - salt ions - present in the feed water. As long as the applied pressure difference, Δp, is larger than the osmotic pressure difference, $\Delta\pi$, water flows from concentrate to the dilute side. Although there is not a deterministic model to describe what controls reverse osmosis process, there are many proposed membrane transport models derived from the non-equilibrium thermodynamics principles which can be considered into two main groups [69]:

(i) Pore flow model

(ii) Solution-Diffusion model

The models relying on the porous approach assumes that transport through the tiny membrane pores is realized by the contribution of both diffusion and convection. The model considers that permeate molecule slowly migrates through straight cylindrical pores which has a certain radius and length. The model proposed by Okada and Matsuura [70], introduce two more assumptions: (1) there is a continuous gradient of the chemical potential, and (2) chemical potential gradient across the membrane can be expressed as a pressure gradient. Considering the semi-permeable porous membranes, mass transport of solvent is described by Darcys law. As the solute concentration is comparably small inside the pores, within this model the mass transport equation is solved just for solvent flux. Solute flux and rejection mechanism is expected to be affected by pore shape relative to solute shape. In the pore-flow models, this issue is not addressed clearly. Thus modern pore models are under development to give a better explanation to two major points: (1) using separate wall correction functions for diffusion and convection, and (2) avoiding using the same concentration on both sides of the membrane as the transport equation is integrated across the

membrane [71]. While the pore-flow model approach is developing, it is found that Solution-Diffusion models describe the transport phenomena more accurately [72]. The main difference between these two methods is that the Solution-Diffusion model assumes the chemical potential is a function of concentration and the pore-flow model assumes chemical potential is a function of pressure. The consequences of this main differentiation are illustrated in Figure 2.2 [69].

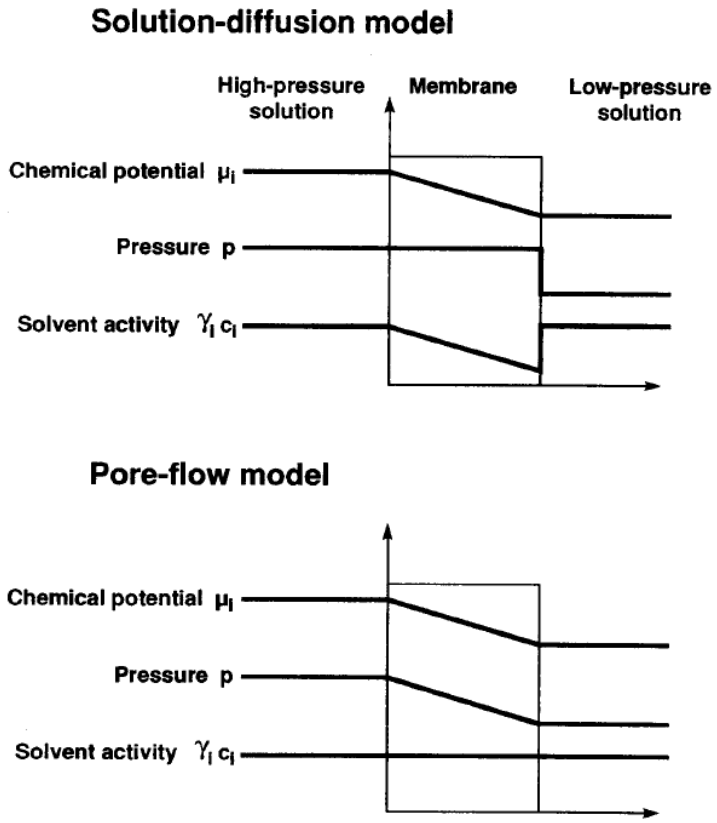

Figure 2.2: Permeating of a one-component solution through a membrane according to solution-diffusion and pore-flow models.

The Solution-Diffusion model relies on the irreversible thermodynamics phenomenon where the basic premise of the model is that permeates first dissolve into the membrane then diffuse through it by means of concentration gradient [72]. The starting point of this model is considering the membrane as a black box where the active layer

is a very dense membrane without pores. Based on such assumption the diffusion mechanism is attempted to be formulated in the form of Fick's laws expression, and it reads as:

$$J_i = -L_i \frac{d\mu_i}{dx} \tag{2.23}$$

where $d\mu_i/dx$ is the chemical potential gradient of component i and L_i is a coefficient of proportionality which can be considered as diffusion coefficient. Any type of driving force can be reduced to the chemical potential gradient, and it is inherently possible to merge multiple driving forces into one chemical potential gradient. Within the concentration and pressure framework the correlation between these two forces and chemical potential for incompressible liquid can be expressed as:

$$\mu_i = \mu_i^o + RT \ln(\gamma_i c_i) + v_i(p - p_{i_{sat}}) \tag{2.24}$$

where, γ_i is the activity coefficient linking concentration with the activity, μ_i^o is the chemical potential of pure i at a reference pressure p^0, c_i is the molar concentration of component i, p is the pressure, $p_{i_{sat}}$ is the saturation vapor pressure, and v_i is the molar volume of component i. By deriving the Fick's law in terms of the chemical potential defined in equation (2.24) the flux of water permeate reduces to [69],

$$J_w = \frac{D_i K_i c_{i_o} v_i (\Delta p - \Delta \pi)}{lRT} \tag{2.25}$$

where D_i is the diffusion coefficient, K_i is the sorption coefficient, c_{i_o} is the concentration at feed side of the membrane, v_i is the molar volume, l is the membrane thickness, R is gas constant, and T is temperature. This equation can be simplified

by introducing a constant water (solvent) permeability, $A = D_i K_i c_{i_o} v_i / lRT$, to

$$J_w = A(\Delta p - \Delta\pi) \tag{2.26}$$

A similar flux for salt (solute) diffusion can also be expressed as:

$$J_s = B(c_{j_o} - c_{j_l}) \tag{2.27}$$

where $B = D_j K_j / l$ is the salt permeability and $c_{j_o} - c_{j_l}$ is the salt concentration difference between upstream and downstream of the membrane.

So far, the missing piece of this model is the osmotic pressure. The thermodynamic definition of osmotic pressure reads [73]

$$\pi = -\frac{RT}{V_b} \ln(x_w) \tag{2.28}$$

with the gas constant R, the temperature T, the molar volume of water V_b, and the mole fraction of water x_w. For dilute solution osmotic pressure, using van't Hoff's law, can be written as

$$\pi = i\phi c_j RT \tag{2.29}$$

where i is the dissociation parameter equal to number of ions and ϕ is the correction factor. This equation can be simplified by introducing a constant osmotic pressure coefficient $\kappa = i\phi RT$ and it reads

$$\pi = \kappa c_j \tag{2.30}$$

and the osmotic pressure difference reduces to

$$\Delta\pi = \kappa \left(c_{j_o} - c_{j_l}\right) \tag{2.31}$$

In the current study while implementing the Solution-Diffusion model a flux condition described in equation 2.26 is applied to the membrane boundaries. To increase the accuracy of the flux prediction, local pressure, local concentration, and local permeate suction rate along the membrane surface is coupled and implicitly solved.

2.3.2 Vacuum Membrane Distillation

Vacuum membrane distillation is a temperature-driven process for separation using hydrophobic microporous membranes where the upstream side of the membrane is in contact with the liquid feed solution and the downstream side is subjected to a vacuum condition. Due to the hydrophobicity of the membrane, the liquid feed solution cannot penetrate into cavities of the membrane unless the liquid entry pressure (LEP) is exceeded. As long as the temperature at the feed side of the membrane is larger than the saturation temperature of the applied vacuum, a liquid-vapor interface forms at the entrance of the pores and the water evaporates, and superheated water vapor passes through the membrane. Finally, the produced water vapor is collected from vacuum channel and condensed using cooling to obtain the clean water.

LEP is a critical pressure that determines the membrane wetting. If the pressure exerted along the membrane surface exceeds this threshold, the feed solution essentially penetrates into the membrane. Once the membrane gets flooded, the liquid flux turns into a mechanism described by Darcy's law. In order to make the membrane operational again, it is required to be dried and cleaned completely [74]. If we consider the fact that the maximum LEP for the state-of-the-art membranes is typically around $200 - 250$ [kPa], this condition arises as one of the main limitations to scale up these modules.

LEP is a characteristic membrane property which is dependent of many factors including but not limited to pore size, geometric factor, and the liquid surface tension.

An estimate relationship between the membrane's maximum allowable pore size and operating conditions is given by the Young-Laplace equation:

$$LEP = \frac{-2G\gamma_{ls}cos(\alpha)}{r_{max}} \tag{2.32}$$

where G is the geometric factor determined by the pore structure, γ_{ls} is the liquid surface tension, α is the liquid-solid contact angle, and r_{max} is the largest pore radius. However the equation (2.32) relies on a few assumptions, such as the pore shapes has to be uniform, which may lead to unignorable errors while inferring the LEP of a real membrane. Thus, experimental measurement of LEP is still more reliable due to the lack of information for liquid surface tension and liquid-solid contact angle.

The explicit driving force in the vacuum membrane distillation mechanism is the vapor pressure difference across the membrane. In the VMD process, the pressure difference is attained by elevating temperature in the feed side and applying vacuum to the permeate side. This is not necessarily the case in other forms of membrane distillation. The application of the vacuum is the distinguishing factor for VMD. It should be noted here that the liquid-vapor interface kinetic effects are negligible. In the permeate channel, the applied vacuum eliminates the presence of any substance other than water vapor so that applied vacuum pressure can be taken as the actual vapor pressure for the production side of the membrane. However, calculating the vapor pressure is not trivial for the feed side since we are interested in estimating water vapor pressure in a non-ideal liquid mixture. To start with pure liquids, the partial pressure of the water vapor in the water liquid is the saturation pressure, P^o, of the corresponding temperature. This is defined by the Antoine equation:

$$p_i = P^o = \exp\left[A - \frac{B}{C+T}\right] \tag{2.33}$$

where T is the temperature, A, B, and C are constants varying for different substances and it is readily available for water ($A = 23.1964,\ B = 3816.44,\ C = -46.13$) [75]. The partial pressure of water vapor in the non-ideal binary mixtures is determined from:

$$p_i = y_i p = X_i \alpha_i P^o \tag{2.34}$$

where y_i and X_i are the vapor and liquid mole fractions of solvent respectively, p is the total pressure and P^o is the saturation pressure of pure water which is determined by Antoine equation (2.33). The activity coefficient, α_i, is modeled by various approaches. Schofield [76] determined the activity of water in NaCl solutions, based on experimental measurements, which reads:

$$\alpha_{water} = 1 - 0.5 X_{\mathrm{NaCl}} - 10 X_{\mathrm{NaCl}}^2 \tag{2.35}$$

where X_{NaCl} is the mole fraction of NaCl. This approximation is considered to calculate activity coefficient in this study since it is rooted in the experimental measurements.

Gas transport through porous membranes have been widely studied, and specifically, in membrane distillation, there are several models attempting to shed light on this complicated phenomenon. Lawson and Lloyd [4] proposed a well-accepted model called Dusty Gas Model (DGM) which defines the transport to take place by means of the combination of several mechanisms and resistances, as illustrated in Figure 2.3.

The DGM describes the mechanism in a combination of four different resistances, but surface diffusion is negligible due to the low surface diffusion area when compared to pore area in typical MD membranes. The remainder of the resistances - viscous, Knudsen, and molecular - occur in most of the membrane distillation types. In the case of the vacuum membrane distillation process, the molecular resistance is also

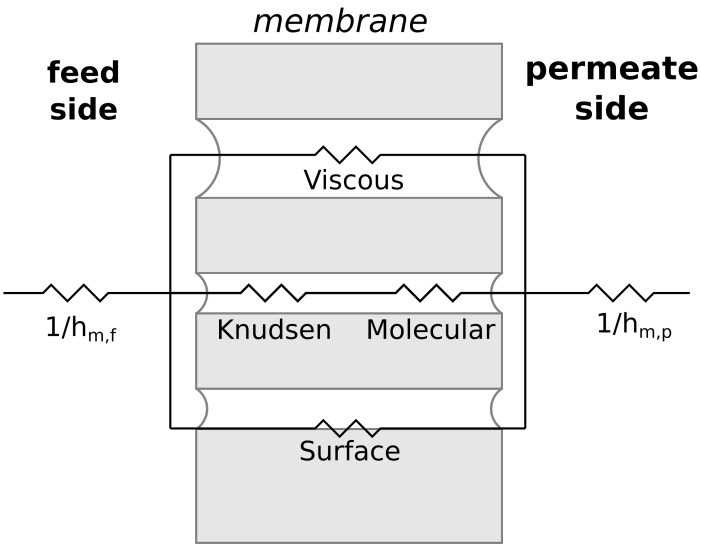

Figure 2.3: Mass transfer resistances in Membrane Distillation

negligible. Since the applied vacuum removes all of the air molecules trapped in the cavities of the membrane, the water vapor is the only substance contained within the membrane [77]. From this fact, neglecting the molecular resistance can be justified. The degree to which diffusion resistance is enacted can be determined by calculating the Knudsen number, $Kn = \lambda/2r_p$, which is the ratio of the mean free path, λ, to the ratio of the pore diameter, $2r_p$. Mean free path is the average distance between successive molecule collisions and from the kinetic theory the expression for the mean free path is given as [78, 79]:

$$\lambda = \frac{k_B T}{\overline{p}\sqrt{2}\pi\sigma^2} \tag{2.36}$$

where σ is the collision diameter of the water molecules, $\overline{p}$ is the mean pressure within the membrane pores, T is the absolute temperature, and k_B is the Boltzmann constant. Matsuura [78] suggested a range for Knudsen number to determine mechanism

dominant or comparable and it is given as:

$$\text{Mechanism} = \begin{cases} \text{viscous}, & \text{if } Kn < 0.01 \\ \text{viscous and Knudsen}, & \text{if } 0.01 \leq Kn \leq 10 \\ \text{Knudsen}, & \text{if } Kn > 10 \end{cases} \tag{2.37}$$

It should be noted that nonuniform distribution of pores in the membrane structure may change the range of Knudsen number determined above. In the current study, Kn mostly happens to be in the transition regime where both viscous and Knudsen flow occurs simultaneously.

In the Knudsen mechanism, the molecule-pore wall collisions dominate the gas transport mechanism, and molar flux of water vapor can be estimated by [21],

$$J_k = \frac{2}{3}\frac{\varepsilon_s r_p}{\tau RT\delta}\sqrt{\frac{8RT}{\pi M_w}}(p_{w,f} - p_v) \tag{2.38}$$

where r_p is the pore size, τ is the membrane tortuosity, δ is the membrane thickness, R is the gas constant, T is the temperature, M_w is the molecular weight of water, $p_{w,f}$ is partial pressure of the water vapor at the upstream of the membrane, and p_v is vacuum pressure at the downstream of the membrane.

The second mechanism for water vapor transport can be classified as viscous flow, which is basically a Poisseuille flow, where molecule-molecule collisions occur due to larger membrane pore sizes. Under this mechanism, the expression to calculate molar flux through the membrane reads

$$J_v = \frac{1}{8\mu_w}\frac{r_p^2\varepsilon_s\overline{p}}{\tau RT\delta}(p_{w,f} - p_v) \tag{2.39}$$

where μ_w is the viscosity of water vapor and $\overline{p}$ is the mean pressure within the mem-

brane pores. Eventually, total molar flux through the membrane can be determined as

$$J_t = J_k + J_v \tag{2.40}$$

Membrane porosity and tortuosity are two key parameters which have an effect on the molar flux, and their interdependency has been long discussed and several approaches proposed. To start with the definitions, porosity, ε, is basically the volume fraction of void inside the membrane and tortuosity, τ, is the curvature of or deviation from cylindrical pores. It is defined as the ratio of the fluid path to the geometrical distance between two points. To ease the conceptualization, $\tau = 1$ (possible minimum) refers to straight pores and higher values refer to convoluted pores. As it is seen, increased tortuosity increases the resistance as well. Regarding the relationship between porosity and tortuosity, Macki-Meares [80] suggested,

$$\tau = \frac{(2-\varepsilon)^2}{\varepsilon} \tag{2.41}$$

and Matyka et al. [81] suggested,

$$\tau = 1 - 0.8 \ln \varepsilon \tag{2.42}$$

It is found the relation suggested by Matyka et al. produces better results when compared to experimental measurements.

Membrane porosity, ε, and membrane surface porosity, ε_s, should not be confused. As expected, considering permeate flux to happen through total membrane area will lead to significant errors. To address this issue, the parameter called membrane surface porosity is introduced [21] and it is an essential one to determine active pore

area which is smaller than the total membrane area. The relation between the surface porosity and the porosity, in terms of tortuosity, is proposed by Martinez et al. [82] which reads

$$\varepsilon_s = \frac{\varepsilon}{\tau} \tag{2.43}$$

As the Membrane Distillation is temperature-driven process evaluation of heat transport is an essential part of the modeling to determine temperature distribution which mandates the water vapor pressure. Figure 2.4, illustrates the possible heat transfer resistances in the process. As one of the major advantage of the vacuum membrane distillation process, the higher degree of vacuum works as an insulator so that conductive heat transfer through the membrane walls can be neglected. At the liquid-vapor interface, the water liquid evaporates by taking energy from the feed stream. Therefore, the total heat transfer through the membrane reduces to

$$Q_m = N_t \Delta h_{fg} \tag{2.44}$$

where $N_t = J_t M_w$ is the total mass flux, M_w is the molecular weight of water, and Δh_{fg} is the enthalpy of water vaporization.

Permeate flow through the membrane leaves the salt ions behind and absorbs energy for evaporation. This results in temperature reduction and increased salt concentration near the upstream surface of the membrane. These phenomena are called temperature polarization and concentration polarization, respectively. To assess the level of polarization various metrics developed. The temperature polarization coefficient (TPC), θ, proposed by Khayet [21] used in this study which reads as

$$\theta = \frac{T - T_{sat}}{T_f - T_{sat}} \tag{2.45}$$

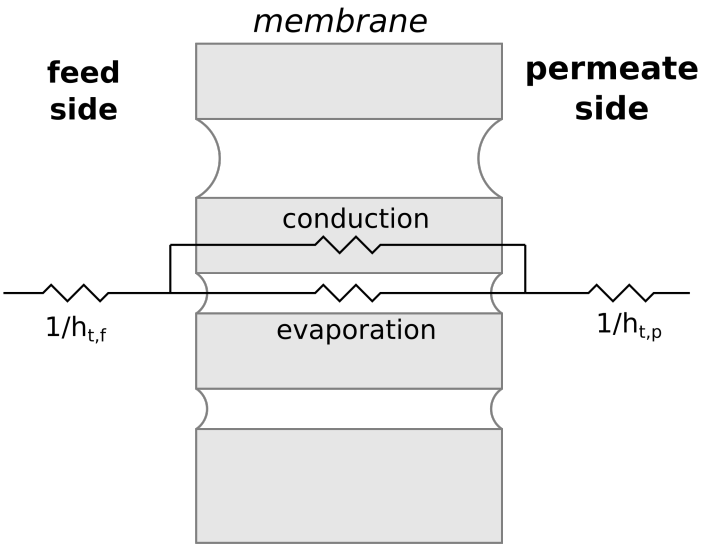

Figure 2.4: Heat transfer resistances in Membrane Distillation

where T_f is the feed temperature and T_{sat} is the corresponding saturation temperature of vacuum pressure. This coefficient varies between 0 and 1 whereas 1 is the ideal case. To keep the membrane functional temperature at the membrane surface has to be larger than saturation temperature.

The concentration polarization coefficient (CPC), φ, straightforward defined as

$$\varphi = \frac{c}{c_f} \tag{2.46}$$

where c is the concentration at the membrane surface and c_f is the bulk concentration. Ideally, unity is desired, and elevated values indicate the severity of concentration polarization.

As discussed above in the DGM, water vapor flux through the membrane is dependent of local pressure, temperature, concentration, and suction rate. In the current study, these four variables implicitly coupled along the membrane boundaries, first in the literature, while evaluating the total permeate flux.

Chapter 3

Computational Methodology

Fluid dynamics can be determined and characterized by several approaches including theoretical, experimental, and computational methods. Each approach has certain limitations and advantages over others. The theoretical approach starts with the first principles of fluid motion and explores analytical solution methods to identify physical phenomena. As long as the mathematical model governs the physical phenomena, this approach produces the most accurate results. However the analytical solution is very limited and mostly inaccessible for including but not limited to complex flow geometries, turbulent flows, multiphase flows. Beyond the limitations of the theoretical method, the experimental approach emerges as an alternative tool to understand flow physics in complex situations. The major disadvantages of the experiments are limited measurement capability, scaling issue, cost, and resolution. Another way to get deep insight into the fluid dynamics is computational methods. These methods rely on the numerical evaluation of physical models, mostly partial differential equations, for a domain of interest. Although the computational fluid dynamics (CFD) approach is limited by computational resources and numerical errors, it is a very promising approach as it enables the observation of details of local flow

properties and parameters.

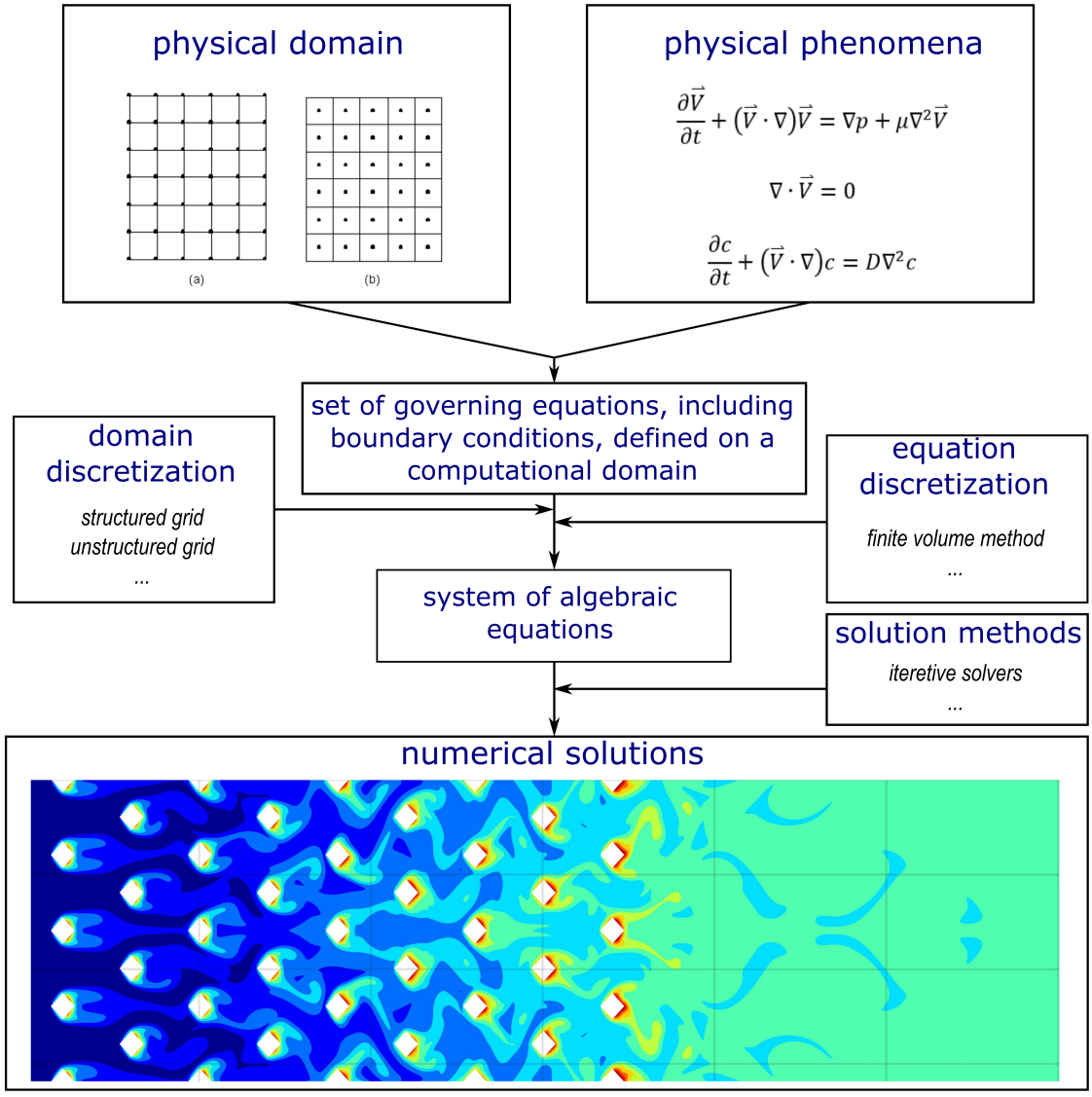

Figure 3.1: Schematic of computational methodology

The computational methodology of fluid dynamics can be considered as a multiple step process, as illustrated in Figure 3.1, which starts with discretization. Discretization is an essential and important step that dramatically dictates the computational resource requirements and the accuracy of numerical results. It is divided into two subfields: domain discretization and equations discretization.

This chapter introduces the methods used to discretize the domain and followed by finite volume method which is an equation discretization method. Then it gives the details of several finite volume method (FVM) solver algorithms. Finally explains the basics of OpenFOAM which is an open-source FVM solver and lists the computational resources to produce results presented in Chapter 4 and 5.

3.1 Domain Discretization

Domain discretization or grid generation is an initial step for the numerical evaluation of fluid dynamics in a geometry of interest which is basically called as a computational domain. The discretization of the computational domain is a subdivision of physical geometry into discrete non-overlapping cells, volumes, or elements where the type depends on the equation discretization method selected. The end result of this process is a grid or mesh system that can be classified as structured or unstructured and has specific properties, such as skewness, orthogonality, which can be used as a measure to assess the quality of the mesh. As finite volume method is adopted for equation discretization, further details of mesh types will be revealed in accordance.

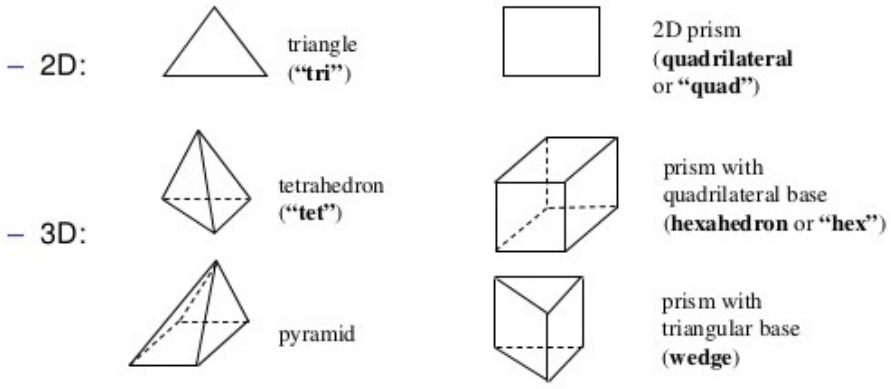

Figure 3.2: Two-Dimensional and three-dimensional mesh types.

Subdivision of a physical domain can be achieved by using different types of control

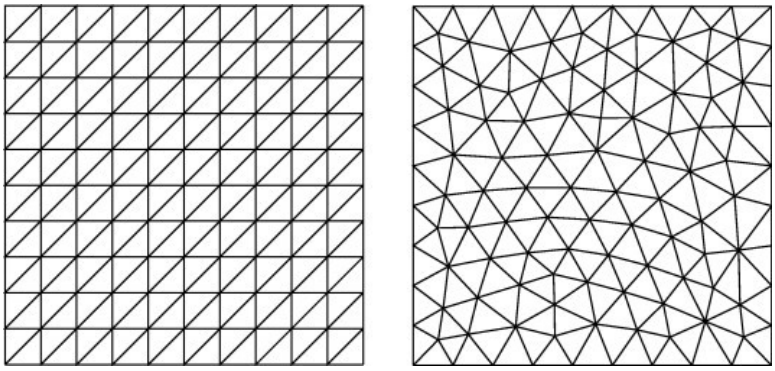

Figure 3.3: Structured (left) and unstructured (right) mesh patterns.

volumes or mesh geometries, as illustrated in Figure 3.2. In all mesh types, the volume is defined by a set of vertices and bounded by faces. Figure 3.3 shows a sample two-dimensional grid in structured and unstructured patterns using the triangle mesh type. The structured grids can also be classified as a single block and multiple block mesh. The critical feature that differentiates the structured mesh from unstructured mesh is that the grid lines must pass all through the block. It is worth adding that special attention needs to be given in multiple block mesh for the interfaces of blocks. The topology of both volume and grid patterns carries important information, such as element to element relations, volume, surface area, surface normal directions, and face to element relations, which has a significant effect on the rate of convergence, solution accuracy, and CPU time required.

As briefly discussed earlier, the quality of the mesh can be measured by many parameters. Based on the impact on the accuracy of numerical solutions, skewness, orthogonality, aspect ratio and expansion ratio can be considered as essential parameters. Figure 3.4 illustrates the definition of these parameters by exemplifying with different mesh types. Increased skewness of the mesh causes a shift between the face center and intersection of the link which will reduce the accuracy of the face value calculation of flow properties. Violation of orthogonality introduces an angle between

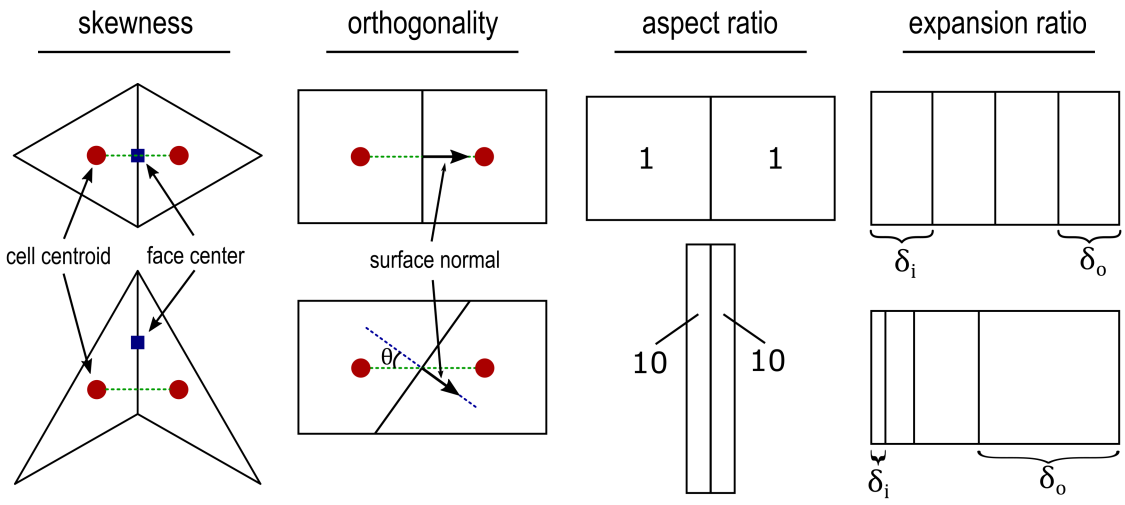

Figure 3.4: Schematic of mesh skewness, orthogonality, aspect ratio, and expansion ratio.

surface normal direction and link direction. Such behavior will require an additional calculation to predict the surface flux properly. The cell aspect ratio should be near unity especially in the regions where the flow is multidimensional. If there is a need for higher aspect ratio, the direction should be adjusted based on the flow conditions. Also, if one is employing an LES subgrid-scale model, note that most of the filter size definitions do not account for the aspect ratios deviating from unity which results in the inaccurate prediction of filtered stresses. Expansion ratio can be considered together with aspect ratio, and larger expansion ratios affect the accuracy of interpolation adversely.

The quality of the mesh also has an impact on the implemented boundary conditions. In order to predict near boundary flow features precisely, the mesh intensity in those regions should be increased accordingly. Beyond that, the quality and type of the mesh can be adjusted as well. While seeking for an optimum mesh to assure grid independence, the accuracy of the solution along the boundaries should be checked

as well as bulk.

3.2 Equation Discretization - Finite Volume Method

Discretization of the governing equations can be achieved in many ways, and it inherently depends on the type of problems to be solved. In the prediction of fluid flow problems and related transport phenomena, the finite volume method becomes prominent over other methods such as finite element and finite difference. This section details the theory of FVM and some of the discretization schemes.

3.2.1 Theory

Finite volume method subdivides the computational domain into small control volumes assuring that the continuum mechanics is still applied to the smallest control volume considered. One of the major advantages of this methods is the conservation property. As it integrates the conservation equations over each control volume, the global conservation of properties of interest is assured. The method is also so flexible that it directly discretize the physical space instead of computational space which requires no additional transformation between spaces. Such feature eases the applicability of this method to very complex geometries and flows in nature.

In general, the finite volume method involves the following steps:

- Integration of conservation equation
- Apply divergence theorem to convert volume integrals into surface integrals
- Approximation of integrals with numerical integration
- Evaluation of properties at the cell surface with a proper scheme

- Assembling and solution of discrete algebraic equations

Consider the differential form of a steady-state conservation equation for a general scalar variable ϕ as:

$$\nabla \cdot (\rho \mathbf{v} \phi) = \nabla \cdot (\Gamma^{\phi} \nabla \phi) + Q^{\phi} \tag{3.1}$$

Integrating the equation (3.1) over a control volume gives:

$$\int_{V_c} \nabla \cdot (\rho \mathbf{v} \phi) dV = \int_{V_c} \nabla \cdot (\Gamma^{\phi} \nabla \phi) dV + \int_{V_c} Q^{\phi} dV \tag{3.2}$$

By employing divergence theorem, volume integrals of the convection and diffusion terms can be replaced with surface integrals. The conservation equation becomes

$$\int_{\partial V_c} (\rho \mathbf{v} \phi) \cdot d\mathbf{S} = \int_{\partial V_c} (\Gamma^{\phi} \nabla \phi) \cdot d\mathbf{S} + \int_{V_c} Q^{\phi} dV \tag{3.3}$$

where $\mathbf{S}$ is the surface vector with the magnitude of control volume surface area, $\mathbf{v}$ is the velocity vector, ϕ is the conserved quantity. By means of finite volume approach equation (3.3) can be expressed as discrete summation of cell surfaces. If we define the total flux as $\mathbf{J}^{\phi} = \rho \mathbf{v} \phi + (-\Gamma^{\phi} \nabla \phi)$ and use a Gaussian quadrature for integral at the face f, discrete form of the conservation equation reduces to

$$\sum_{f} \sum_{p} (\mathbf{J}^{\phi} \cdot \tilde{\mathbf{n}})_{f,p} \omega_{fp} S_f = \sum_{m} (Q^{\phi}_{m} \omega_m V) \tag{3.4}$$

where f refers to faces of the cell, p refers to a number of integration point at each surface, m refers to a number of integration point at each control volume, and ω refers to weight function. As might be expected, increasing the number of integration points increases the accuracy while requiring more computational resource. Now using the equation (3.4) one can assemble and solve the set of discrete algebraic equations.

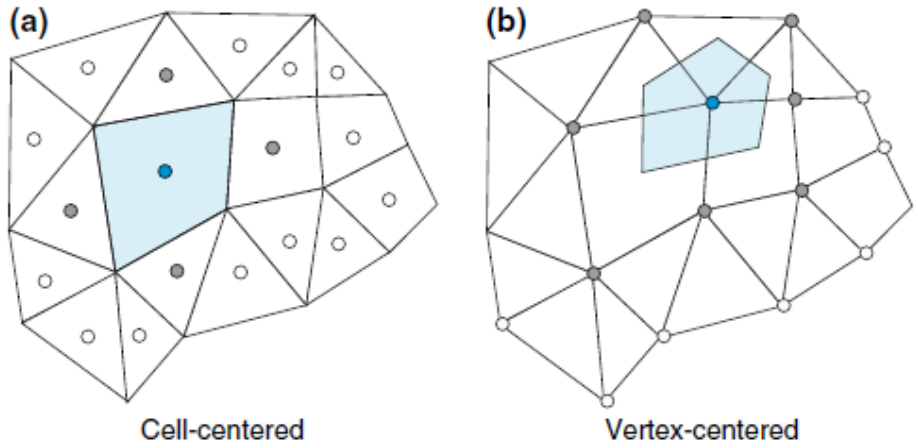

Figure 3.5: Finite volume method (a) cell-centered and (b) vertex-centered variable arrangement [2].

The variable arrangement in the finite volume method can be defined as either cell-centered or vertex-centered, as shown in Figure 3.5. The cell-centered method is more favorable in most of the FVM solver. At this juncture, OpenFOAM is also adopting the cell-centered variable arrangement. This approach requires the evaluation of diffusion and convection flux terms at the cell interfaces. As discussed in the section (3.1) the accuracy of this evaluation at interfaces strictly relies on the mesh quality and discretization schemes. In the next section, details of mostly used FVM discretization schemes are discussed.

3.2.2 Discretization Schemes

Discretization is an essential step to determine flow properties and gradients along the cell interfaces and boundaries. In finite volume method, the selection of a proper discretization scheme is strictly tied to the mesh structure. By knowing the skewness and orthogonality of the mesh, one can correctly determine required schemes for diffusion, convection, and other terms if necessary.

While selecting a numerical scheme for the discretization, each term in the conservation equations should be treated differently, and the general set of terms can be listed as:

- Time schemes: first and second time derivatives, "$\partial/\partial t, \partial^2/\partial t^2$"
- Divergence schemes: divergence, "$\nabla\cdot$" (Convective terms)
- Laplacian schemes: laplacian, "∇^2" (Diffusive terms)
- Gradient schemes: gradient, "∇"
- Interpolation schemes: cell to face interpolations of values.
- Surface normal gradient schemes: component of gradient normal to a cell face.

Commonly encountered terms and relevant schemes for each term is discussed in the following subsections.

Time Schemes

Numerical evaluation of transient fluid dynamics problems requires the discretization in both space and time. The temporal discretization relies on the time stepping procedure and does not require to store all the time history. Depending on the accuracy of discretization, storing the time history just for one or two previous step provides satisfactory results in most of the problems encountered. In fluid mechanics generally, the time-dependent problems involve transient and non-transient terms that general equation can be expressed as in the form

$$\frac{\partial(\rho\phi)}{\partial t} + \mathbb{H}(\phi) = 0 \tag{3.5}$$

and integration over control volume (cell) and a spatial discretization about the volume centroid yields

$$\frac{\partial(\rho_c\phi_c)}{\partial t}\mathrm{v_c} + H(\phi_c^t) = 0 \tag{3.6}$$

where $\mathrm{v_c}$ is the volume of the discretization element. The discretization can be achieved by either finite difference or finite volume approach. The following declarations adopt the latter.

- **First order implicit Euler scheme:**

$$\frac{(\rho_c\phi_c)^t - (\rho_c\phi_c)^{t-\Delta t}}{\Delta t}\mathrm{v_c} + H(\phi_c^t) = 0 \tag{3.7}$$

- **Second order implicit backward scheme:**

$$\frac{\frac{3}{2}(\rho_c\phi_c)^t) - 2(\rho_c\phi_c)^{t-\Delta t} + \frac{1}{2}(\rho_c\phi_c)^{t-2\Delta t}}{2\Delta t}\mathrm{v_c} + H(\phi_c^t) = 0 \tag{3.8}$$

- **Second order Crank-Nicholson scheme:**

$$\frac{(\rho_c\phi_c)^{t+\Delta t} - (\rho_c\phi_c)^{t-\Delta t}}{2\Delta t}\mathrm{v_c} + H(\phi_c^t) = 0 \tag{3.9}$$

While solving transient problems based on the problem definition, transport phenomena, necessity for boundedness, and desired accuracy, one of the time scheme listed can be selected.

Divergence schemes

Convective terms are essential for Navier-Stokes equation evaluations and require attention to get a proper discretization scheme. Their tendency of oscillation makes

the evaluation harder and requires higher order schemes in some problems. The most common convection schemes and their details are listed below.

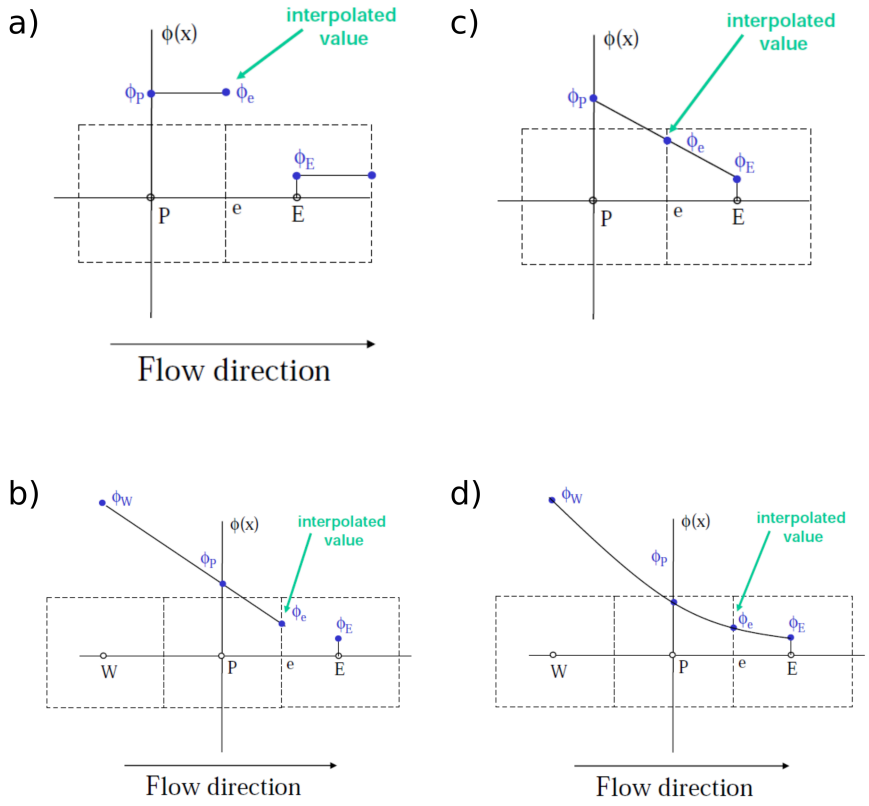

Figure 3.6: (a) upwind, (b) linear-upwind, (c) linear, and (d) QUICK schemes for divergence term discretization [3].

- **First order upwind scheme (Figure 3.6a):** Gathers the information from upstream and deals with the transportive property of the term. It is inherently a non-oscillatory and diffusive method and assumes that the cell value is isotropic.

- **Second order linear-upwind scheme (Figure 3.6b):** calculates the values of a property by using the information from two upstream cells. While it enjoys

the accuracy of second order, it deviates in the presence of higher gradients and needs limited for stable solutions.

- **Second order linear scheme (Figure 3.6c):** Relies on the linear interpolation of values between the cell centers. Performs better in isotropic mesh and produce better results in LES simulations. The method is more accurate, but unwantedly it can be oscillatory as well for the larger values of Peclet number, which is the ratio between convective and diffusive transport.

- **Third order Quadratic Upwind Interpolation for Convective Kinetics (QUICK) scheme (Figure 3.6d):** constructs a quadratic curve by using from two upstream and one downstream cell. For the application simplicity, the flow locally can be treated as one-dimensional results in one curve for each spatial direction.

Laplacian schemes

The discretization of diffusion terms usually investigated separately due to their disparate physical phenomena and Laplacian form of the term. When compared to other terms, laplacian terms require the evaluation of not only values but also gradients at the cell face center. Consider a typical laplacian term in the Navier-Stokes equation to be $\nabla \cdot (\nu \nabla U)$. To evaluate the values at the cell face centers, one needs to define an interpolation scheme for the diffusion coefficient, which is ν in this case, and a surface gradient scheme for ∇U. Selection of interpolation scheme does not substantially affect the accuracy of discretization since it is mostly a scalar property. However, a rigorous approach is required for the surface normal gradient because in most of the applications unstructured or nonorthogonal mesh is inevitable.

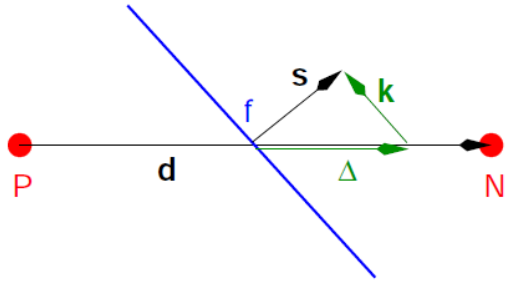

Figure 3.7: Evaluation of laplacian terms at non-orthogonal cell face center.

Figure 3.7 illustrates a typical scheme to evaluate properties at non-orthogonal cell face centers. The expression for this evaluation reads

$$\mathrm{s}_f \cdot (\nabla\phi)_f = |\mathrm{s}_f| \frac{\phi_N - \phi_P}{|\mathrm{d}_f|} + \mathrm{k}_f \cdot (\nabla\phi)_f \tag{3.10}$$

Here there is the second term on the right side of the equation (3.10) to account for non-orthogonal contributions to the gradient evaluation. The next issue would be how severe is the non-orthogonality in the mesh. By knowing one can implement proper correction schemes. Therefore before choosing discretization scheme, one better know statistics of the mesh such as orthogonality and skewness. OpenFOAM offers the options showed in Figure 3.8 for surface normal gradient discretization.

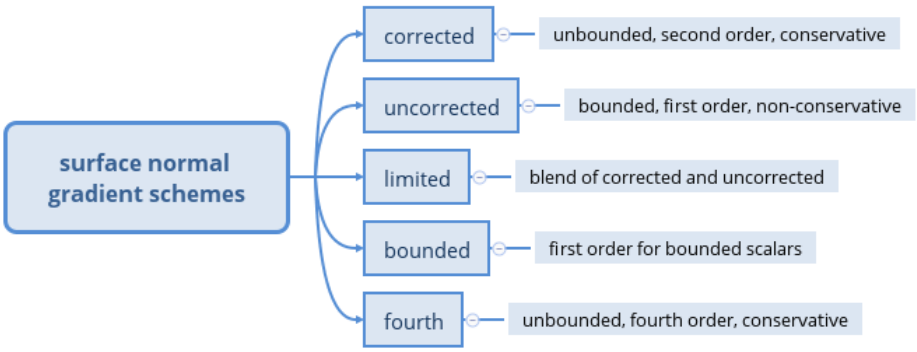

Figure 3.8: List of OpenFOAM Laplacian schemes and their behaviors.

3.3 Numerical Solver Algorithms

The previous section discusses the details of numerical discretization of conservation equations however it is not enough to obtain a complete solution for flow governing equations due to coupled nature of velocity and pressure [83]. Consider a three-dimensional incompressible flow governed by the conservation of mass and momentum equations which results in four equations and four unknowns - $\vec{v}(x, y, z),\ p$ - which is a closed problem and seems solvable. However, in these equations pressure is not defined explicitly so that the solution of the system requires an algorithm to properly update and solve discrete equations system. This task is not too complicated for the compressible flows since conservation of mass equation is used to evaluated density, and the pressure is linked to density by equations of state. To address the coupling issue in the incompressible flows, several different algorithms are developed and implemented in many problems successfully [83–87]. SIMPLE, PISO and PIMPLE algorithms are different approaches to the problem. SIMPLE and PISO is a standard name in the field whereas PIMPLE is named in the OpenFOAM libraries as the combination of SIMPLE and PISO algorithms.

3.3.1 Semi-Implicit Method for Pressure-Linked Equations Method - SIMPLE

The SIMPLE algorithm and its variations are the most commonly used method for the numerical evaluation of conservation equations comprised of partial differential equations. The algorithm is proposed by Patankar and Spalding [85] and relies on the idea of the guess-and-correct procedure. A typical SIMPLE algorithm sequence is shown in the Figure 3.9. As the algorithm seeks for a solution by looping until the convergence criterion is reached, the method is essentially designed and valid

for steady-state solutions where the solution is independent of time. The algorithm starts with an initial guess, assembles the set of equations, and solves in a segregated fashion. Then it evaluates the pressure correction equation and corrects the pressure and velocity field. If the convergence criterion is not met at this point, pressure and velocity are updated, and the loop returns to the assembling step. While updating the fields based on the correction, it is important to keep the solution stable. As for this reason, a relaxation approach is introduced to set a limit to updating step. Setting a relaxation coefficient close unity provides a rapid convergence rate while increasing the instability of the solution.

3.3.2 Pressure-Implicit with Splitting of Operators - PISO

As the name of the algorithm suggested, the method splits the prediction procedure based on the implicit and explicit steps [86], as illustrated in Figure 3.10. The flow of the algorithm starts very similarly to the SIMPLE method as the implicit solver and pressure corrector steps take places until the second correction. After that second correction step begins and this part of the correction procedure repeats by the defined number of corrector specific to PISO algorithm. As the repeating part solves the equations explicitly, the rate of convergence increases significantly so that not many iterations needed as in SIMPLE. This advantage of the algorithm makes it a very good candidate for transient simulations.

3.3.3 Combination of SIMPLE and PISO - PIMPLE

PIMPLE algorithm is developed in the OpenFOAM libraries and provides more stable solutions in time-dependent simulations. It basically removes one of the major limitations of PISO algorithm by merging the SIMPLE and PISO. The Courant

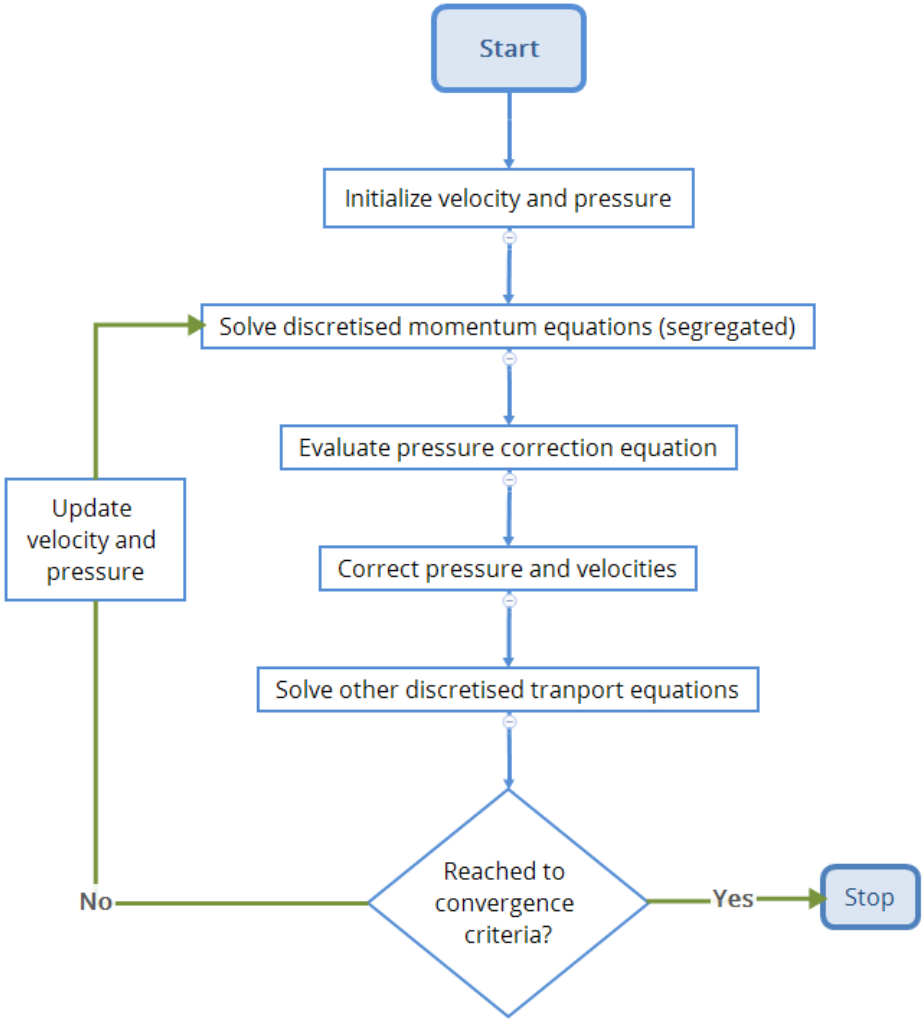

Figure 3.9: The sequence of operations for SIMPLE algorithm.

number larger than unity may cause instability when using PISO algorithm whereas the PIMPLE can go as high as 10 depending on the flow type, Reynolds number and discretization schemes. The key addition in this method is the outer corrector which is equivalent to SIMPLE iterations. If one sets the number of outer correctors to be 1, the algorithms essentially become PISO. Increasing the number of outer correctors will provide better-converged results at each time step enabling the stability at larger Courant numbers. Another critical addition of PIMPLE algorithm in OpenFOAM is

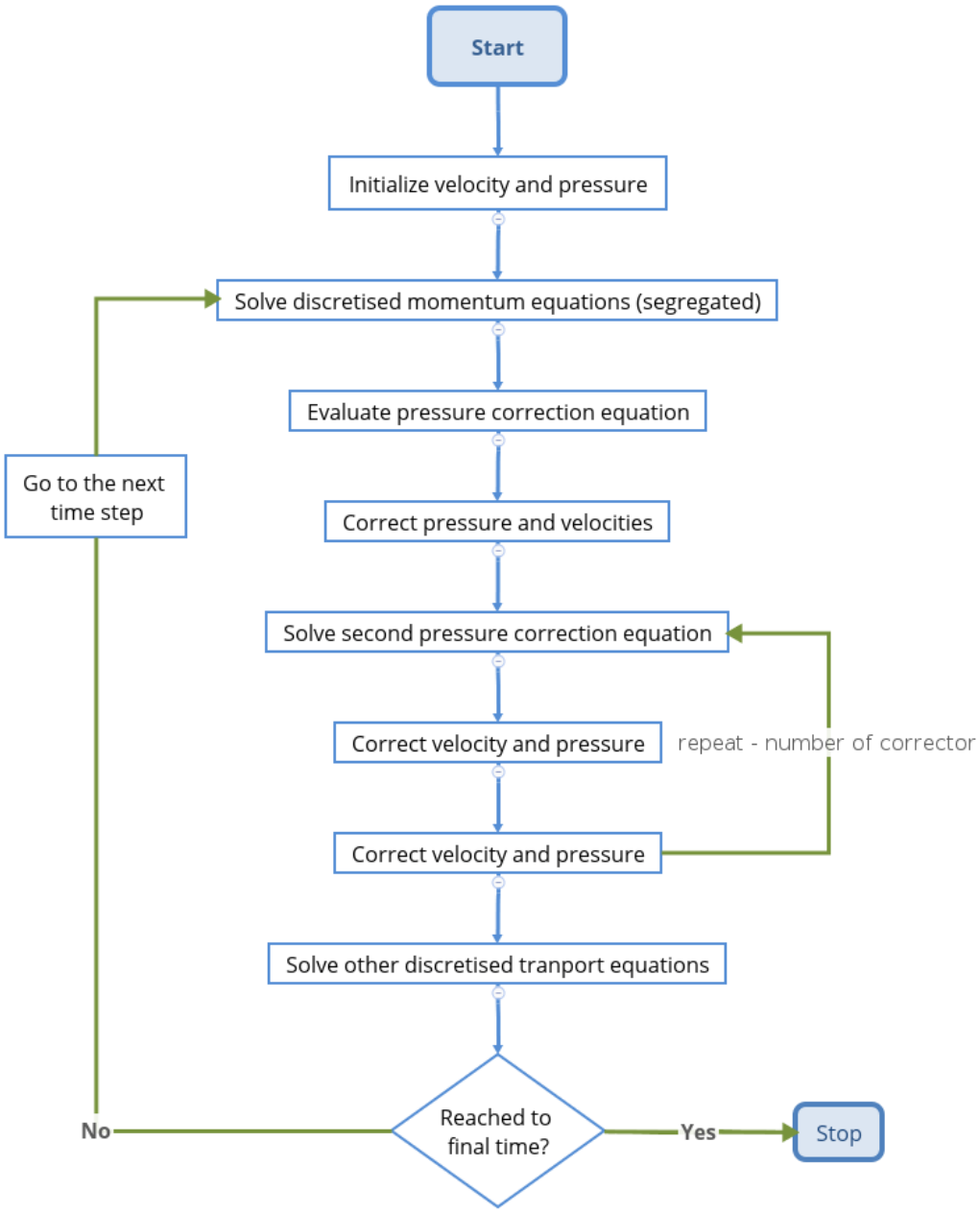

Figure 3.10: The sequence of operations for PISO algorithm.

being able to set two different convergence criteria; one for the initial steps and one for the last outer corrector step. Thanks to this adjustment, the desired convergence criterion does not need to be so aggressive all the time which provides computational time reduction in turn.

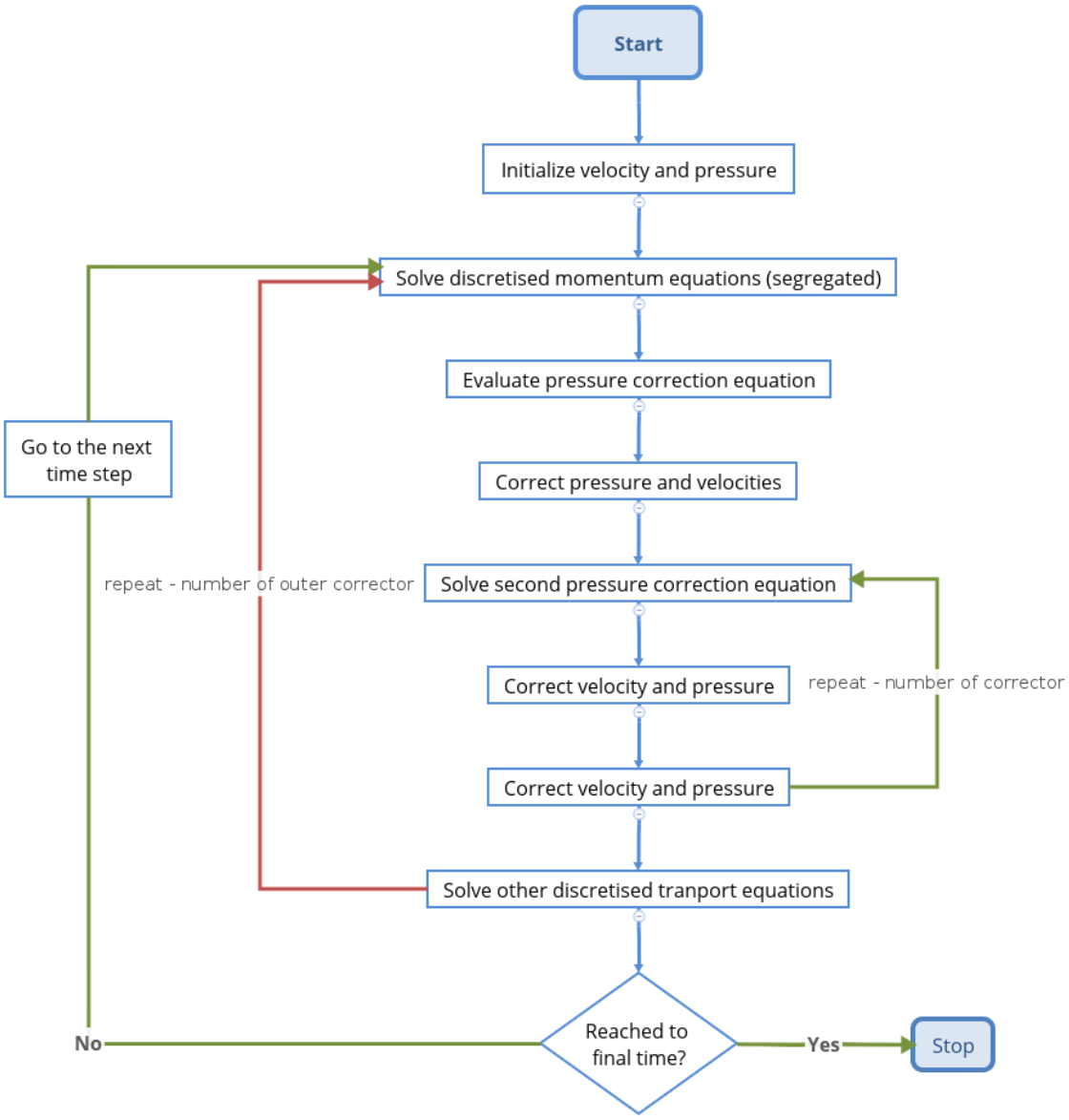

Figure 3.11: The sequence of operations for PIMPLE algorithm.

3.4 Finite Volume Method solver - OpenFOAM

OpenFOAM (Open Source Field Operation and Manipulation) is an open-source finite volume method solver developed using C++ libraries. The solver was originally initiated by Henry Weller in late 1980s at Imperial College, London and improved by other joined forces, Hrvoje Jasak to name one of them. The development community

fragmented in time giving rise to an increasing number of projects. In this study specifically, OpenFOAM v1706 version is employed. OpenFOAM uses the Object-Oriented Programming capabilities of C++ extensively so that it becomes very flexible for extension and custom development. It provides a wide range of pre-processing and post-processing tools such as blockMesh and ParaView along with the solvers which makes it a full environment for computational fluid dynamics.

OpenFOAM has a unique tensor operation syntax which closely resembles the partial differential equation considered, illustrated in Figure 3.12. The simplicity of the syntax provides easiness while developing custom solvers. Additionally, the fully parallelized structure of the applications decomposes the domain and enables utilization of the solvers in a distributed parallel mode using message passing interface (MPI) by default or other libraries.

$$\frac{\partial \rho \mathbf{U}}{\partial t} + \nabla \bullet \phi \mathbf{U} - \nabla \bullet \mu \nabla \mathbf{U} = -\nabla p$$

Represented by the code

```
solve
(
    fvm::ddt(rho, U)
  + fvm::div(phi, U)
  - fvm::laplacian(mu, U)
    ==
  - fvc::grad(p)
);
```

Figure 3.12: A sample OpenFOAM syntax for tensor operations.

OpenFOAM provides a wide range of solvers for different applications and flow phenomena. The main categories of this solvers and several solvers underneath each

category can be listed as:

- Incompressible
  - icoFoam
  - simpleFoam
  - pisoFoam
  - pimpleFoam
- Compressible
  - rhoCentralFoam
  - rhoPimpleFoam
- Multiphase
- Direct numerical simulations (DNS)
- Combustion
- Heat transfer and buoyancy-driven flows
- Particle-tracking flows
- Discrete methods
- Electromagnetics
- Stress analysis of solid
- Finance

3.5 Computational Resources

Computational fluid dynamics simulations of complex flows are very demanding task regarding computational capabilities. Explicit and implicit solutions of strongly coupled partial differential equations describing the change of phenomena in both time and space push the boundaries of memory and CPU utilization. In the current study, the problems ranged from steady to unsteady, laminar to turbulent, and 1

to 120 million mesh elements. Achieving the results presented in Chapter 4 and 5 required extensive computational resources. To achieve that several high-performance computing resources from local to large scale clusters are employed. The system configurations of these resources are listed below.

- Local HPC machines
  - Max allocated node: 1
  - CPUs : 3.5GHz 6-Core Intel Core i7-5930K Haswell-E
  - RAM : 64 - 128 GB DDR3-2133
  - Network interface : None
- SOL - Lehigh University HPC center
  - Max allocated node: 4
  - CPUs : 2 $\times$ 2.3GHz 12-core Intel Xeon E5-2670 v3
  - RAM : 128 GB DDR4-2133
  - Network interface : 100 Gb/s EDR Infiniband network interface
- Bridges - Pittsburgh Super Computer Center (accessed through XSEDE allocation)
  - Max allocated node: 16
  - CPUs : 2 $\times$ 2.3GHz 14-core Intel Xeon E5-2695 v3
  - RAM : 128 GB DDR4-2133
  - Network interface : Intel Omni-Path Architecture
- Comet - San Diego Super Computer Center (accessed through XSEDE allocation)
  - Max allocated node: 8
  - CPUs : 2 $\times$ 2.5GHz 12-core Intel Xeon E5-2680 v3
  - RAM : 128 GB
  - Network interface : 56 Gb/s (bidirectional) link bandwidth

Chapter 4

Results of Reverse Osmosis

4.1 Reverse Osmosis by Twisted Hollow Fiber Membrane Module

4.1.1 Problem Description

Conventional HFM desalination modules encase thousands of co-axially aligned HFMs in a mutually parallel flow of brackish water. HFMs are subject to a phenomenon called concentration polarization (CP), which leads to fouling and will eventually prevent clean water production. Momentum mixing in the HFM module is one of the key mechanism that increases the mass transport of accumulated retentate along membrane surfaces back into the bulk flow and disrupts local concentration fields along and near the HFM surfaces [5]. The approach to increase momentum mixing throughout the module involves the introduction of a novel twist to the traditional HFM module design. This study characterizes and compares the flow structures and performance of twisted and straight, co-axially aligned three-dimensional HFM modules. To the best of our knowledge, flow and concentration field characterization with proper membrane conditions throughout a twisted HFM module has not yet been reported on. To compare system performance, we consider the permeate fluxes of both geometries relative to their required pumping power. It will be shown that the twisted HFM geometry outperforms the straight, co-axially aligned geometry despite additional necessary pumping power due to increased system friction. System performance will be evaluated by Sherwood number, friction factor, the coefficient of performance, and transmembrane permeate mass flux.

The convoluted module geometry was obtained by twisting the straight module so that a 360^o rotation about the center HFM occurred at a pitch length of $360d$ as seen in Figure 4.1. Rotation occurs about the centermost HFM in the twisted

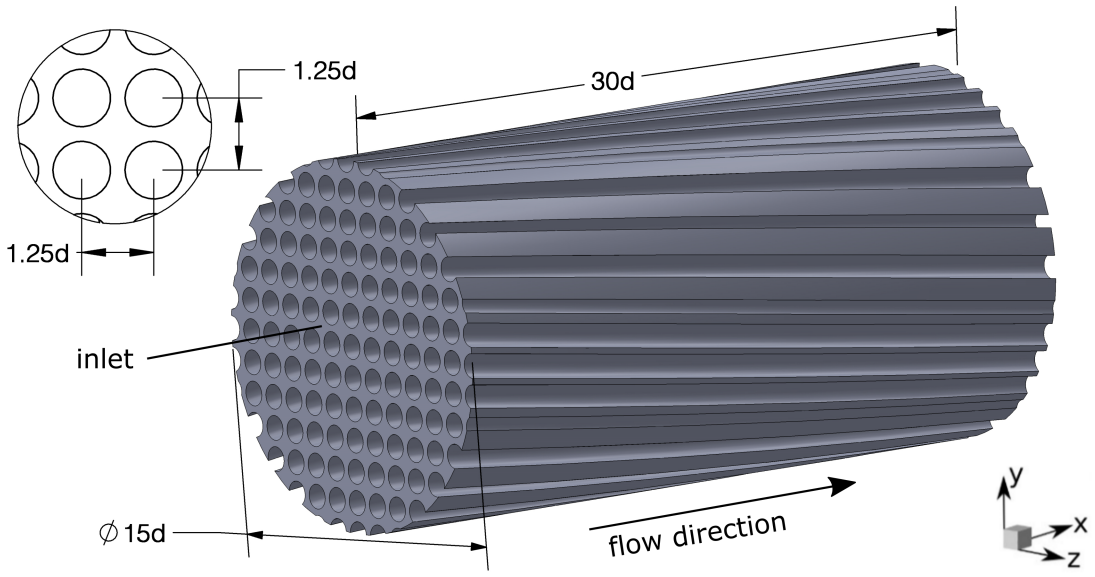

Figure 4.1: Schematic of the computational domain for proposed twisted geometry. The spacing between HFMs, the length and the diameter of the module and (x,y,z) coordinates are illustrated. Here d is the hydraulic diameter of the module which is the same as the diameter of the fiber for the spacing $1.25d$.

geometry, which is parallel to the modules axial direction. The full pitch length was not considered in this study, rather the module is convoluted about 30^o for the considered simulation domain. The outermost HFM, measured from the radial center, possesses the greatest angle of attack relative to the stream-wise direction of roughly 6^o. The three-dimensional computational domain considered in this study features an encased HFM bundle comprised of more than 100 fibers at a spacing of $1.25d$. As opposed to the circular outer shell of the twisted HFM module, a square cross-sectioned geometry is modeled for the straight HFM module with the application of the periodic boundary condition. The total simulation domain lengths are $x/d = 30$ and $x/d = 60$ for the twisted and straight geometries, respectively. The flow through straight HFM module promotes less mixing and it requires a longer length to reach an asymptotic value of Sh. Since the performance measurements and comparison of cases are achieved based on the asymptotic value of Sherwood number, the simulations of

straight geometry are conducted in a longer geometry. In accordance with this fact, the cross-sectional planes are purposely selected in different distances for straight and twisted geometry to evaluate the asymptotic values of Sherwood number and to eliminate the undesirable effects of the outlet boundary condition.

In this study, contours and profiles illustrating flow properties are rendered at various cross-sectional planes for the straight and twisted geometries. For clarity, the location of these planes within the module is shown below in Figure 4.2. Planes are located at $x/d = 25$ in Figure 4.2a, $z/d = 0$ in Figure 4.2b, $x/d = 55$ in Figure 4.2c, and $z/d = 0.625$ in Figure 4.2d. Figure 4.2a and Figure 4.2b depict the twisted geometry, and Figure 4.2c and Figure 4.2d depict the straight geometry. The $z/d = 0.625$ plane is situated in the bulk flow region between two adjacent HFM rows. The selected simulation parameters listed in Table 4.1 reflect real physical operating parameters observed in commercial systems.

Flow in the module is considered to be laminar, and the conservation equations are discretized using a finite volume approach. Our attempt of simulations with turbulence model failed to produce a converged solution for the range of flow speed considered in the current study since there is no flow separation occurring from the HFMs. The geometry was created using SolidWorks 2016, and the mesh was generated by Ansys 14.5 Meshing. The governing equations were numerically solved by the CFD solver in OpenFOAM v1706 using a pressure-based scheme with second-order upwind discretization.

Regarding the boundary conditions, at the module inlet, a uniform stream-wise velocity component in the x-direction, U_{ave}, is fixed. Reynolds number, $Re = (U_{ave}d)/\nu$, is defined based on the specified inlet velocity, where $d = 9.8 \times 10^{-4}$ [m] is the membrane hydraulic diameter. The hydraulic diameter is defined by $d = (4A_c)/P_w$ where A_c is the cross-section area and P_w is the wetted perimeter. A no-slip condition

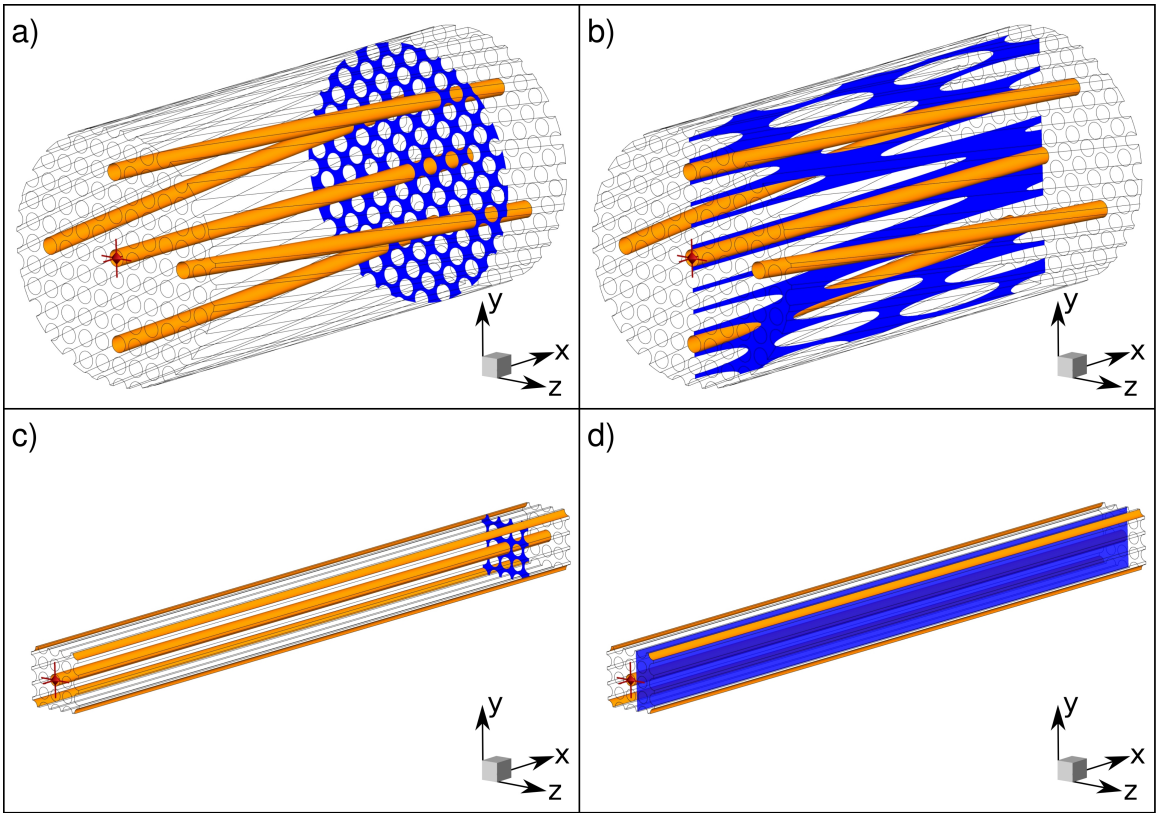

Figure 4.2: Locations of rendered contour plot planes for twisted (top row) and straight, co-axially aligned (bottom row) HFM module geometries. The subfigures are rendered at the (a) $x/d = 25$, (b) $z/d = 0$, (c) $x/d = 55$, and (d) $z/d = 0.625$ planes.

is employed throughout the HFM surfaces. The solution-diffusion [69] membrane transport model couples the local salt concentration, local transmembrane pressure difference, and local permeate flux, and is employed along all HFM surfaces. Based on this model, a suction condition is applied to the normal velocity component along HFM surfaces, which is set to zero along the impermeable module wall. A uniform concentration distribution of 4000ppm is specified at the module inlet, which is a typical brackish water concentration. A zero-pressure gradient is imposed at the module outlet.

The boundary conditions for the side wall or outer shell differs between both

Table 4.1: Physical simulation operating parameters.

Parameter	**Value**	**Ref**
Density: ρ	1000 [kg/m^3]	[9]
Dynamic viscosity: μ	10^{-3} [Pa s]	[9]
Transmembrane pressure: Δp	1.25 [MPa]	[9]
Concentration in the production side: c_p	0 [ppm]	[88]
Initial feed salt concentration: c_0	4000 [ppm]	-
Diffusivity: D	1.5×10^{-9} [m^2/s]	[88]
Osmotic pressure coefficient: κ	75 [kPa m^3/kg]	[88]
Permeability: A	2.3×10^{-11} [m/Pa s]	[88]
Schmidt number: $Sc = \nu/D$	667 [$-$]	[88]
Fiber bundle void fraction	0.5 [$-$]	[89]
Fiber radius:	5×10^{-3} [cm]	-
Fiber length	$3 - 6$ [cm]	-
Reynolds number	500, 1000, 1500 [$-$]	-

geometries. The straight geometry adopts a matching symmetric behavior on the side wall which enables the use of transitional periodicity. However, the use of periodic boundary conditions in the radial direction is not possible for the convoluted module geometry because the HFM angle of attack increases with radial distance. In the twisted geometry, the membrane boundary conditions are applied to any HFM inside or touching the shell and no-slip, and no-penetration boundary conditions are applied to the outer shell surface. Instead of eliminating the HFMs touching to the outer shell, it is modeled with regular spacing to avoid large voids with less friction in the flow direction.

Simulation results presented in this study are nondimensional. Velocity and concentration are normalized by the inlet velocity, U_{ave}, and inlet concentration, c_0,

respectively. Vorticity is normalized by ν/d^2, where d is the hydraulic diameter and ν is the kinematic viscosity. Suction rate along membrane surfaces is normalized by $A\Delta p$, where A is the membrane permeability and Δp is the transmembrane pressure difference. Shear stress is normalized by the maximum shear stress observed in the $Re = 1500$ case, τ_{max}.

4.1.2 Mesh Independence

Grid independence is important for accurate predictions for both flow field and concentration. Due to the high Schmidt number, concentration boundary layer tends to be thinner than the flow boundary layer. Such behavior needs special attention to resolve concentration boundary layer and predict surface properties for precise coupled boundary condition. Therefore, a very careful attention is given to mesh encryption, which includes an inflation type mesh, along with the membrane surfaces while generating the mesh. Two key parameters for inflation layer is the first mesh element layer thickness and the growth rate of the inflation. For the twisted geometry, a mesh refinement study was performed for the largest Reynolds number of 1500 to ensure that characterization of the flow and concentration fields was independent of the selected mesh resolution. Five different mesh densities were considered for the fixed simulation domain size; they utilized 40, 64, 90, 103, and 122 million (M) mesh elements. In each mesh set the first mesh element layer thickness and the inflation growth rate varies as well. Two properties are compared using the five mesh densities in Figure 4.3, which are the average normalized salt concentration as a function of the stream-wise direction for a single HFM as well as the normalized stream-wise velocity component along a line in the z-direction. The results using 103M and 122M mesh elements deviated by less than 0.1%. Therefore, we employed 103 million mesh elements for the simulations in this study, where the element size is 1.2×10^{-3} d along

the membrane surface.

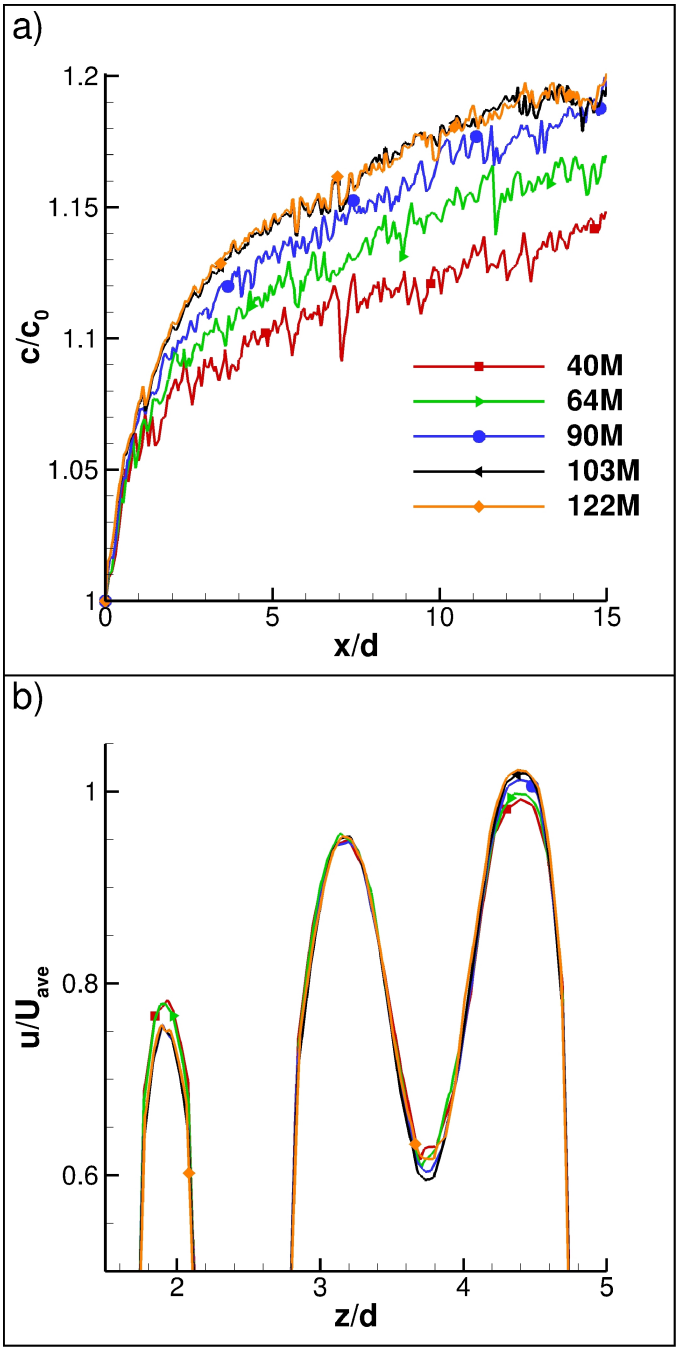

Figure 4.3: Mesh independence results for five mesh densities utilizing 40, 64, 90, 103, and 122 million (M) mesh elements in the twisted geometry. (a) Average normalized concentration along a single membrane surface in the flow direction and (b) normalized velocity along a line in the z-direction.

4.1.3 Model Validation

To validate the mathematical model and the numerical method, we conducted a simulation in a geometry employed by Hawler et al. [89] using the same membrane properties and operating parameters. Hawler et al. investigated the performance of an RO HFM desalination module and reported the product recovery rate for various volumetric flow rates, feed concentrations, temperatures, and feed pressure. Since the validation test is performed by comparing the predicted and measured product recovery rate, we run simulations in the module with a full length. Due to the limitations of the computational resources we considered a square cross-sectional domain with transitional periodic boundary conditions as described in straight geometry design. Since the flow inside the module is nearly parallel to the hollow fibers the effect of such simplification on the performance of the module is negligible. Matching Reynolds number between the computational and experimental study for the validation test is calculated to be 62 based on the physical, geometric, and operating flow properties reported in Ref [89]. The parameters used for the validation study are listed in Table 4.2.

Hawler and his colleagues reported the product recovery rate to be 23.3% for the operating parameters listed in Table 4.2. Our prediction for the product recovery rate is 21.4%, which only differs by 8.9% from the measured value. Figure 4.4 depicts profiles of the averaged concentration and suction rate in the stream-wise direction obtained by simulations. Detailed profiles regarding the suction rate and concentration along the surface of HFMs, as depicted in Figure 4.4, were not provided in Ref [89]. The averaged values of surface concentration and suction rate are determined at each cross-section. Near the inlet, the suction rate and membrane surface concentration change rapidly by adjusting the inlet conditions. In the region slightly away from the inlet, the suction rate decreases linearly while the concentration increases linearly.

Table 4.2: Model validation operating parameters.

Parameter	**Value**	**Ref**
Transmembrane pressure: Δp	6.31 [MPa]	[89]
Concentration in the production side: c_p	0 [ppm]	-
Initial feed salt concentration: c_0	35000 [ppm]	[89]
Diffusivity: D	1.5×10^{-9} [m^2/s]	[88]
Temperature: T	28^o [C]	[89]
Permeability: A	1.61×10^{-13} [m/Pa s]	[89]
Fiber bundle void fraction	0.5 [$-$]	[89]
Fiber length	75 [cm]	[89]

The severity of the concentration polarization is apparent. The suction rate profiles also explain why the product recovery rate is very low in this module at this operating condition. These profiles also indicate that the Sherwood number will asymptote to a constant value for a given flow rate. Additionally, Usta et al. [11] employed the same membrane transport model used in the present study and validated it against the experimental study conducted by Ho et al. [90].

4.1.4 Results

In this section, results for the characterization of both straight and twisted HFM reverse osmosis modules, comparison of their characteristics, the effect of radial distance to the performance, and coefficient of performance is presented.

Characterizing Flow Structures of the Straight Geometry

Normalized stream-wise velocity component, vorticity magnitude, and concentration contours are illustrated in Figure 4.5 for the straight geometry at the $x/d = 55$

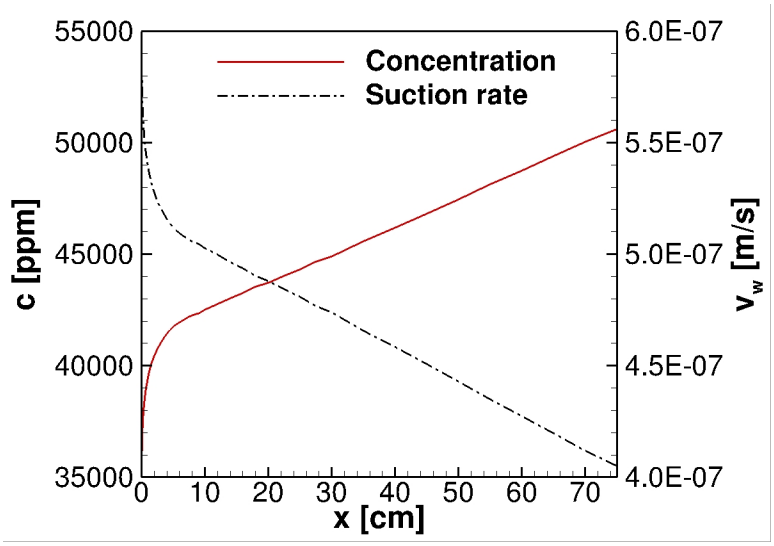

Figure 4.4: Salt concentration and water suction rate profiles in the stream-wise direction for model validation. Corresponding concentration and suction rate values for each x location are obtained by averaging in the azimuthal direction for all HFMs at a given cross-section.

plane, depicted in Figure 4.2c, for $Re = 1500$. The velocity contour, illustrated in Figure 4.5a, is characterized by two discrete bulk flow regions. The first of these regions is characterized by a majority of the bulk flow, wherein the flow velocity has retarded slightly due to the friction of nearby HFMs. The second region is centrally located between any four neighboring HFMs, where there are isolated jet flows that have considerably higher velocity than at the inlet. These two velocity regions interact very minimally, and this poor mixing and is unfavorable for increasing system performance. The vorticity magnitude contour, illustrated in Fig 4.5b, reveals three distinct regions of vortical activity. Vorticity is highest along and near to membrane surfaces, and is lowest in the high-speed jet flow regions. The third region buffers the other two, and characterizes most of the bulk flow vortical activity. Vorticity dramatically dissipates in narrow gap regions between any two adjacent HFMs and persists slightly farther into the wide gap regions, where adjacent HFMs are farther away. The concentration field, illustrated in Figure 4.5c, is overwhelmingly dominated by

uniformly low concentration because the Schmidt number is large.

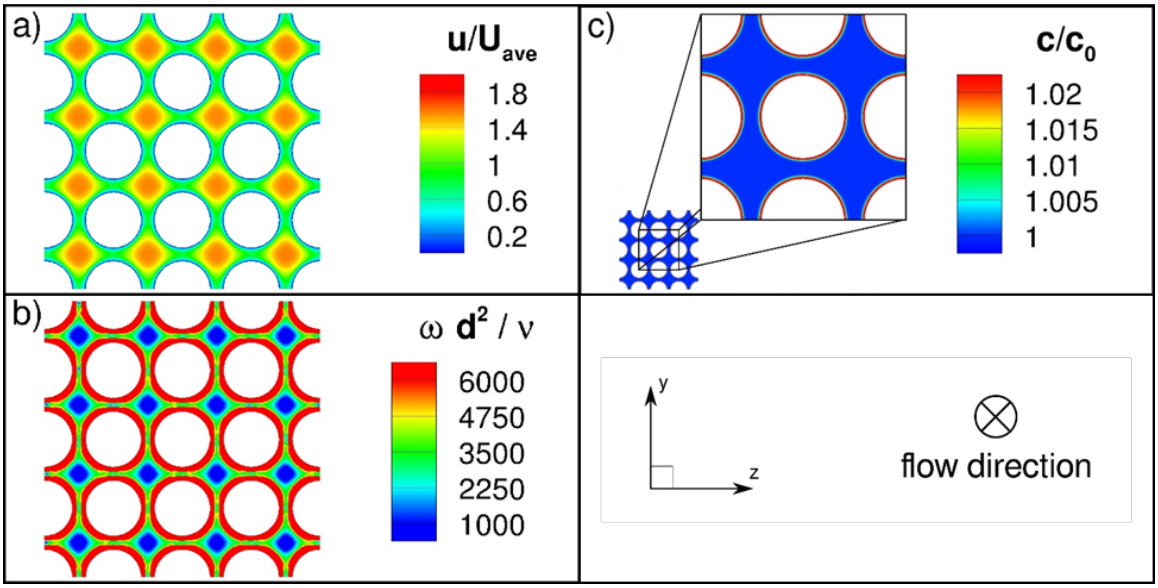

Figure 4.5: Normalized (a) stream-wise velocity component, (b) vorticity magnitude, and (c) concentration contours for $Re = 1500$ at the $x/d = 55$ plane for the straight, co-axially aligned geometry. Quantities are normalized by the average inlet velocity, ν/d^2, and the inlet concentration, respectively. Location of the rendered plane is illustrated in Figure 4.2c.

Figure 4.6 illustrates normalized stream-wise velocity component and vorticity magnitude contours for $Re = 1500$ at the $z/d = 0.625$ plane, depicted in Figure 4.2d, for the straight geometry. Vorticity magnitude contours appear slightly distorted, especially near the boundaries, in Figure 4.6b due to post-processing of the unstructured mesh used in the current study. The flow has high speed in jet flow regions because it traverses the module uninterruptedly there, and with little resistance from nearby HFMs, shown in Figure 4.6a. The jet flows exhibit low vortical activity, shown in Figure 4.6b. Contours in Figure 4.6 are located in the bulk space between HFM rows, and high vortical activity appears to be totally absent here. High fluid speeds and low vortical activity in the bulk flow suggest that the straight, co-axially aligned geometry abets minimal momentum mixing, which is not conducive to increasing wa-

ter desalination module performance. The corresponding concentration field is not shown, but it should be noted that the bulk flow has uniformly low concentration, which also indicates minimal mixing throughout the module.

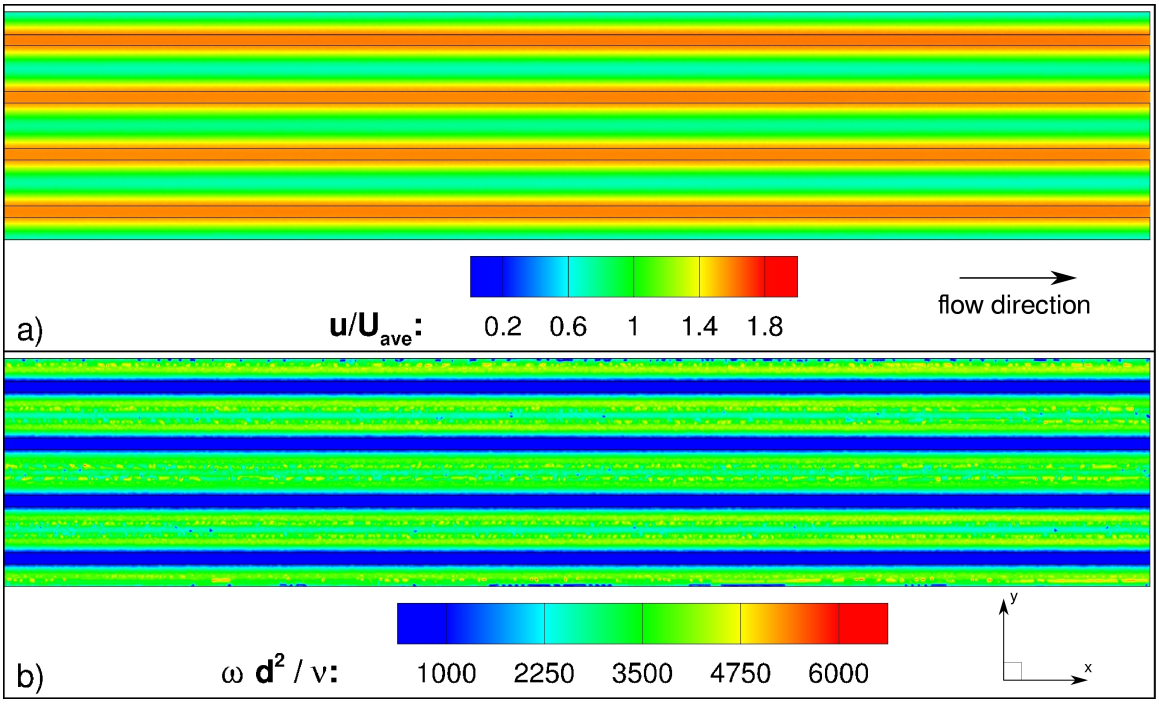

Figure 4.6: Normalized (a) stream-wise velocity component, and (b) vorticity magnitude contours for $Re = 1500$ at the $z/d = 0.625$ plane for the straight, co-axially aligned geometry. Quantities are normalized by the average inlet velocity and ν/d^2, respectively. Location of the rendered plane is illustrated in Figure 4.2d.

Characterizing Flow Structures of the Twisted Geometry

Normalized stream-wise velocity component contours are illustrated for the twisted geometry in Figure 4.7 for $Re = 500$, 1000, and 1500 at the $x/d = 25$ plane. In the cross-section view of the twisted HFM module, the fibers appear to have circular cylinder whereas it is elliptical. This is because the radius of the ellipsis changes with the cosine of the angle of attack which is not perceptible for the considered geometry in this study. The red regions indicate high-speed jet flows, which are large and

mostly symmetric near the module center. Twisted HFMs increase in angle of attack with distance from the radial center and become increasingly effective at breaking-up jet flow regions indicated in Figure 4.7 by the smaller and increasingly asymmetric jet flow regions nearer to the module edge. Impeding and breaking-up the jet flows with twisted membranes increases momentum mixing throughout the module, which is favorable for increasing module performance.

Two phenomena contribute to the decreased normalized speed of jet flows as Reynolds number increases, depicted in Figure 4.7. The first is related to an increased velocity gradient along HFM surfaces as Re increases. This can be realized as the increase in wall shear stress as flow rate increases, as presented later. The velocity gradient, with respect to the normal direction along any HFM surface, increases with Reynolds number, which accelerates fluid closer to membrane surfaces and lowers the normalized peak velocity in the gap regions. The second is related to water removal from the bulk flow by HFMs. Normalized jet flow velocity near the module center decreases with increasing Reynolds number because higher fluid speeds near the membrane surface improve membrane efficacy and enable relatively more water removal from the bulk flow into the membrane cavities. Thus, the velocity of the bulk flow decreases because there is relatively less mass passing through the given feed-side flow area. The increase of permeate passing through HFMs at higher Reynolds numbers is discussed further and quantified later.

Normalized vorticity magnitude contours are illustrated in Figure 4.8 for the twisted geometry at $Re = 500$, 1000, and 1500 at the $x/d = 25$ plane, depicted in Figure 4.2a. Two trends in vortical activity are common in all cases. First, there is low vorticity in the gap regions centered between any four HFMs. Second, there is high vortical activity along and very near to membrane surfaces. Normalized bulk flow vortical activity is mostly uniform everywhere in the module for the smallest

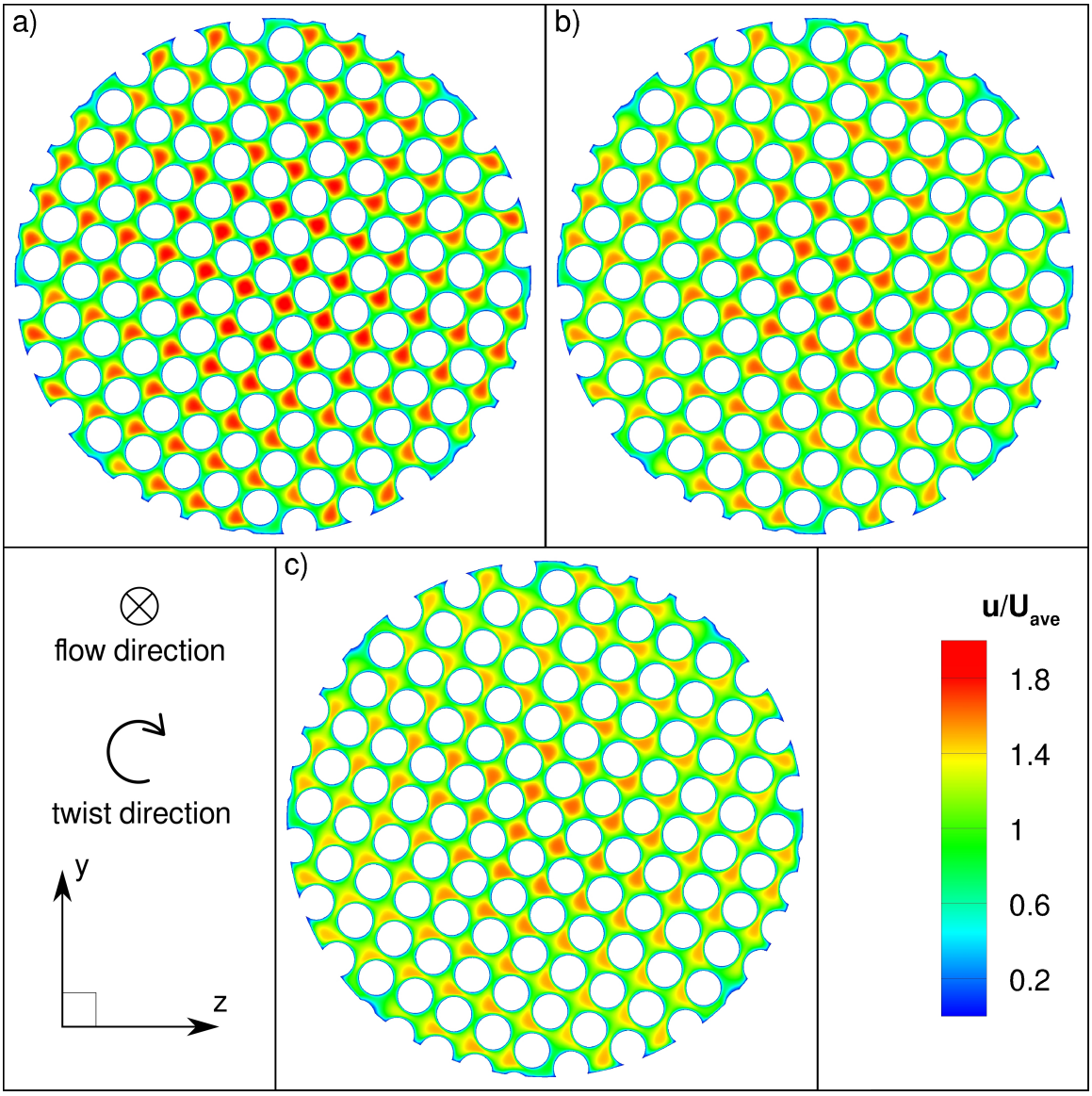

Figure 4.7: Normalized stream-wise velocity component contours for (a) $Re = 500$, (b) $Re = 1000$, and (c) $Re = 1500$. Velocity is normalized by the averaged inlet velocity. Contours are rendered for the twisted geometry at the $x/d = 25$ plane. Location of the rendered plane is illustrated in Figure 4.2a.

Reynolds number, $Re = 500$. However, slightly higher vortical activity is observed that surrounds the module center for $Re = 1000$ and 1500. The shape of the vortical structures changes substantially with distance from the radial center for $Re = 1000$ and 1500. Clearly, increased flow rate induces more intense and desirable vortical

activity distributions in the twisted geometry.

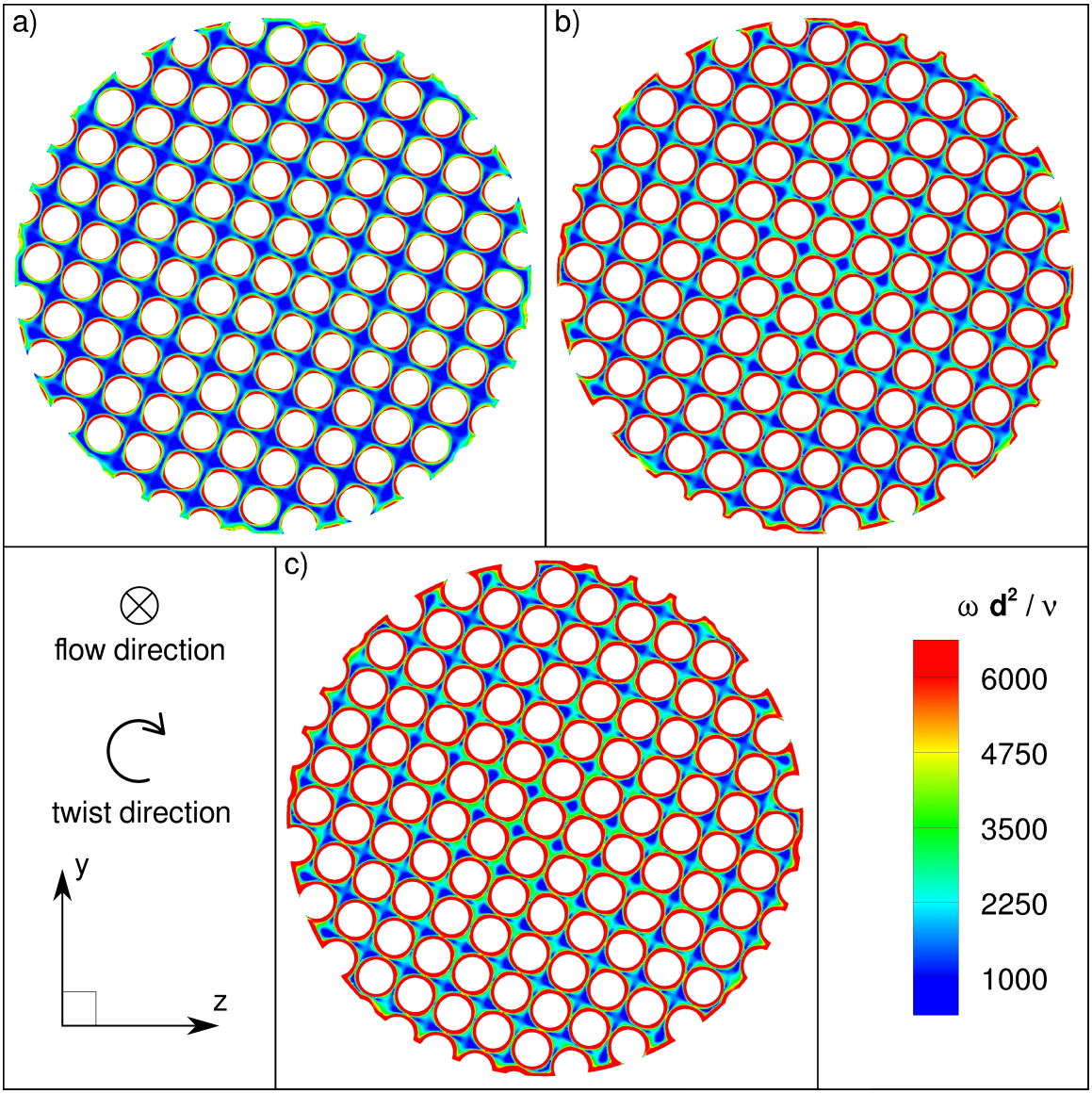

Figure 4.8: Normalized vorticity magnitude contours for (a) $Re = 500$, (b) $Re = 1000$, and (c) $Re = 1500$. Vorticity is normalized by ν/d^2. Contours are rendered for the twisted geometry at the $x/d = 25$ plane. Location of the rendered plane is illustrated in Figure 4.2a.

Figure 4.9 illustrates normalized concentration contours for the twisted geometry for $Re = 500$, 1000, and 1500 at the $z/d = 0$ plane, depicted in Figure 4.2b. Figure 4.9 exhibits a concentration boundary layer at the trailing edge of the HFMs, which

decreases in size as flow rate increases. Higher salt concentrations along membrane surfaces abruptly decay to the inlet concentration level in the narrow gap regions between any two HFMs because the Schmidt number is large. Figure 4.9 clearly illustrates increasing HFM angle of attack with distance from the radial center.

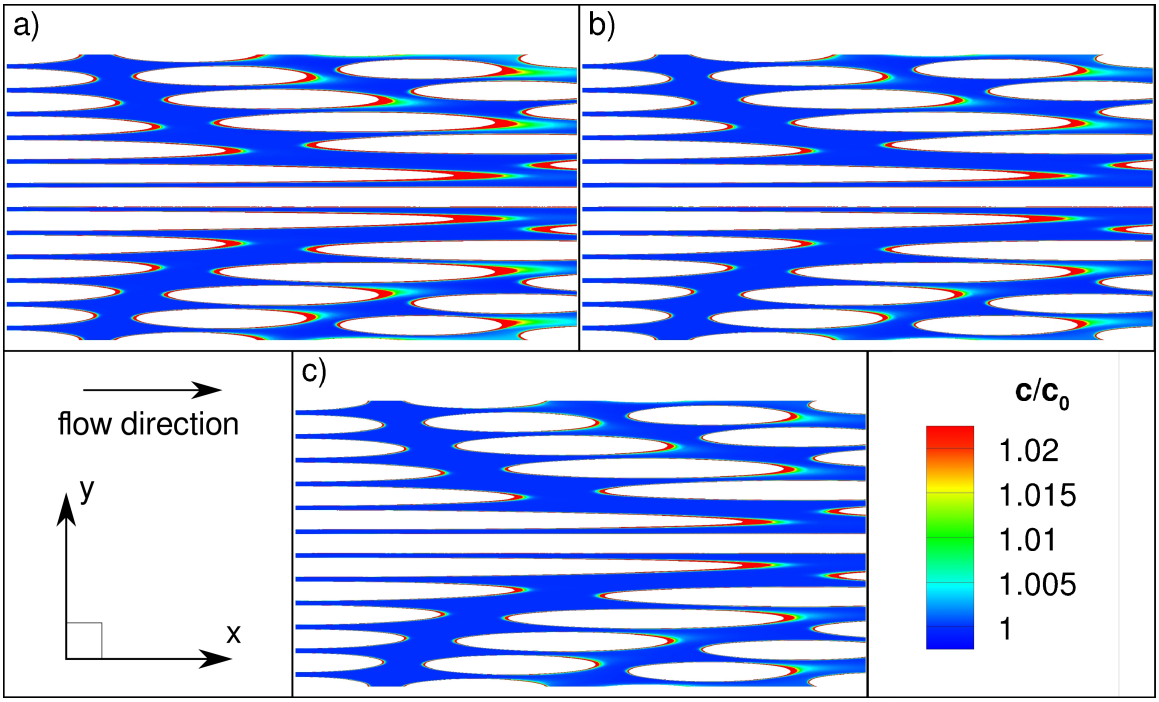

Figure 4.9: Normalized concentration contours for (a) $Re = 500$, (b) $Re = 1000$, and (c) $Re = 1500$. Concentration is normalized by the inlet concentration. Contours rendered at the $z/d = 0$ plane, depicted in Figure 4.2b.

Comparison of Membrane Surface Properties between Geometries

Figure 4.10 and Figure 4.11 illustrate normalized concentration, suction rate, Sherwood number, vorticity magnitude, and shear stress magnitude profiles along selected HFM surfaces in the straight, co-axially aligned and twisted geometries, respectively. Sherwood number, Sh, is evaluated using the relation

$$Sh = \frac{d\ h_m}{D},\ h_m = \frac{D\nabla c \cdot \vec{n}}{c_b - c_m} \tag{4.1}$$

where h_m is the local mass transfer coefficient, $\vec{n}$ is the surface normal direction, d is the characteristic length, D is the diffusivity, c_b is the bulk concentration, and c_m is the concentration at membrane surface.

The centermost HFM was selected to illustrate the surface properties in the straight geometry, depicted in Figure 4.10f. The selected HFM in the twisted geometry is depicted in Figure 4.11f, and is in the fourth concentric row outward from the center. The profiles are rendered for $Re = 500$, 1000, and 1500 at the $x/d = 25$ and 55 planes for twisted and straight geometries, respectively.

As water permeates through HFM surfaces, the salt concentration increases along the exterior HFM surface. Figure 4.10 indicates that the normalized salt concentration distribution along the membrane surface is inversely related to the Reynolds number, but the normalized suction rate and Sherwood number distributions directly scale with the Reynolds number. We see that concentration, suction rate, and Sherwood number are nearly uniformly distributed along the HFM surface, except for minor inhomogeneities due to the presence of adjacent HFMs. These are most readily seen in the suction rate and Sherwood number profiles for $Re = 500$, which appear to have a slightly more square distribution. The vorticity and shear stress magnitude profiles for the straight geometry, in Figure 4.10d and Figure 4.10e, differ from the other surface properties, because the presence of adjacent HFMs greatly impacts their distributions, whereas the other surface properties are largely uniform. Vorticity and shear stress along the membrane surface both scale with local fluid speed, are smallest where HFMs are most near, and are largest where HFMs are farthest away.

Figure 4.11 indicates that the trends observed for varying Reynolds number in the straight geometry are preserved in the twisted geometry - concentration is inversely proportional to the Reynolds number, and all other membrane properties scale with the Reynolds number. However, differing flow structures in the twisted geometry

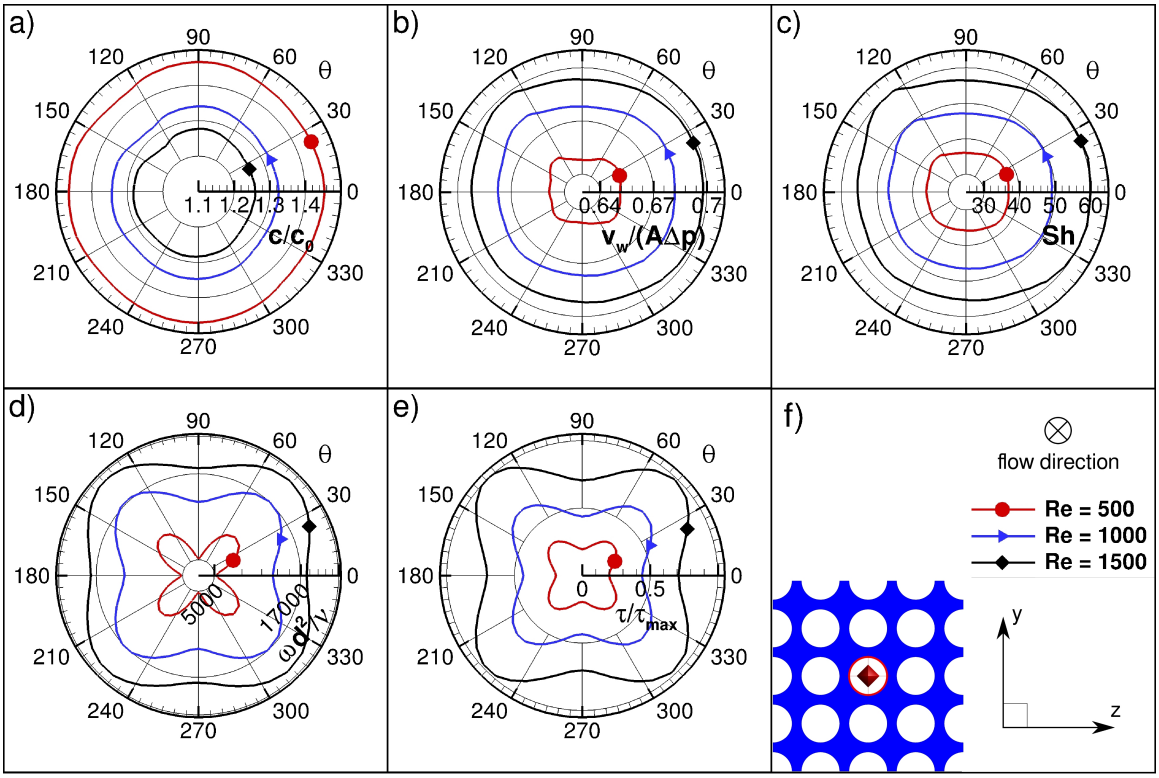

Figure 4.10: Normalized (a) concentration, (b) suction rate, (c) Sherwood number, (d) vorticity magnitude, and (e) shear stress magnitude profiles along the membrane surface for the centermost HFM in the straight geometry at the $x/d = 55$ plane for $Re = 500$, 1000, and 1500. All quantities are normalized, and the location of the selected HFM is shown in (f)

greatly change the distribution of flow properties along the membrane surface, as well as alter their magnitudes. Convoluting the HFM bundle about its radial center introduces leading and trailing edges along the HFM surface since twisted HFMs away from the module center have angles of attack askew to the flow direction. The twisted module design introduces a swirl, which adds cross-flow velocity components to the existing axial flow. The added cross-flow components increase momentum mixing throughout the module, thereby increasing membrane performance and mitigating concentration polarization.

The swirling flow in the twisted module alters the distribution of flow properties

along the membrane surface, illustrated in Figure 4.11. The normalized suction rate, Sherwood number, vorticity magnitude, and wall shear stress distribution profiles in the twisted geometry are smallest at the leading and trailing edges. However, the normalized concentration profile for the twisted geometry, shown in Figure 4.11a, is greatest at the leading and trailing edges. The distribution of flow properties along HFM surfaces in the twisted geometry is considerably more asymmetric, indicating increased momentum mixing has been achieved. The flow property magnitudes along HFM surfaces differ for the twisted geometry. Normalized concentration along the membrane surface, depicted in Figure 4.11a, decreases in the twisted geometry, indicating a reduction in concentration polarization along the membrane surface. Normalized suction rate, shown in Figure 4.11b, is largest in the twisted geometry for all Reynolds numbers. Sherwood number and normalized vorticity magnitude profiles, depicted in Figure 4.11c and Figure 4.11d respectively, increase dramatically in the twisted geometry - on the order of one magnitude for some Reynolds numbers. On the other hand, shear stress magnitude along the HFM surface did not dramatically change for the twisted geometry, although the shape of the distribution did.

Figure 4.12 illustrates running averaged Sherwood number profiles as a function of the stream-wise direction for both geometries. Figure 4.12 was obtained by averaging Sherwood number in the azimuthal direction at each cross-section along the domain length for all HFMs. While averaging Sherwood number, the HFMs closer to the outer shell are omitted to minimize end effects. Figure 4.12 indicates that Sherwood number reaches an asymptotic value in a considerably longer distance for the straight geometry. In both geometries, the asymptotic value of Sherwood number increases with Reynolds number. Sherwood number is nearly twice as large in the twisted case.

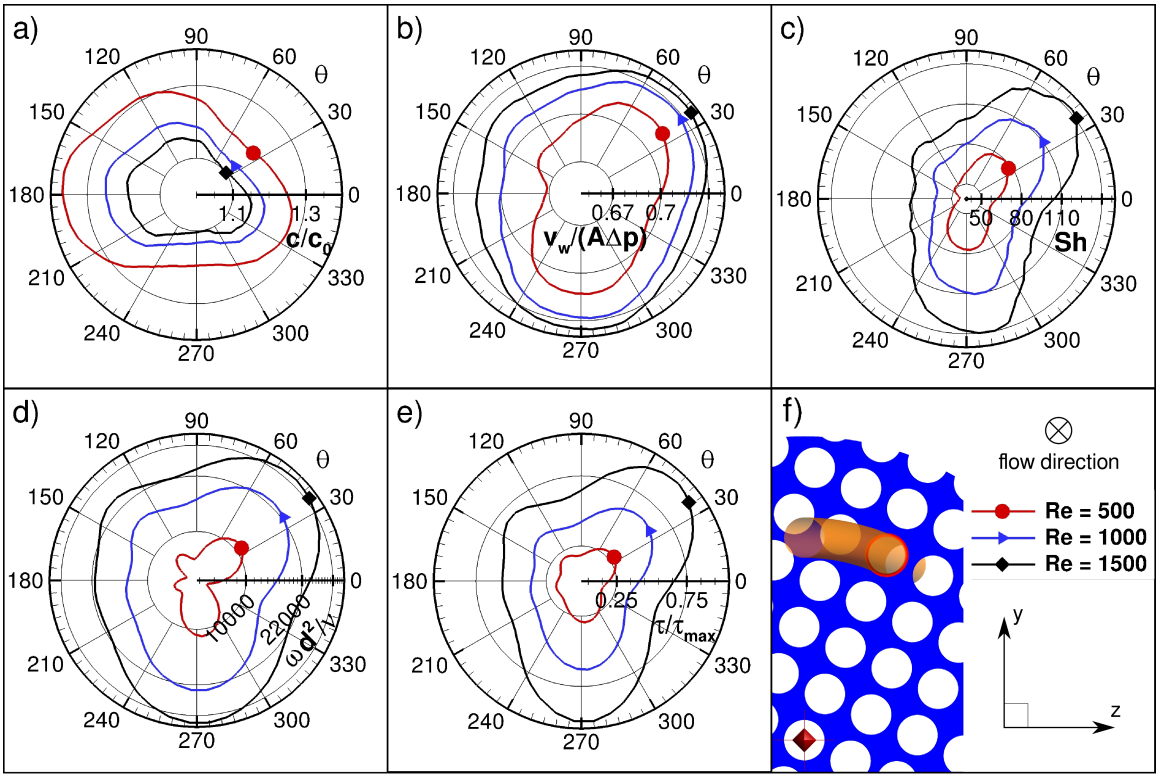

Figure 4.11: Normalized (a) concentration, (b) suction rate, (c) Sherwood number, (d) vorticity magnitude, and (e) shear stress magnitude profiles along the surface of the selected HFM for the twisted geometry at $Re = 500$, 1000, and 1500. The selected HFM is shown in (f), and the profiles are rendered at the $x/d = 25$ plane.

Effect of Radial Distance on Membrane Surface Properties for Twisted Geometry

The angle of attack for an HFM is the angle formed between the flow and the fibers axial direction at any point along the membrane, which increases for HFMs further from the module center. Cross-flow velocity components are generated when flow interacts with HFMs of non-trivial angles of attack. At a threshold distance from the module center, the HFMs have sufficiently large angles of attack that flow separation would occur from the trailing edge. In this study, such angles of attack do not exist because the module radius considered herein is not large enough. Figure 4.13 and Figure 4.14 illustrate flow characteristics along HFM surfaces in the twisted

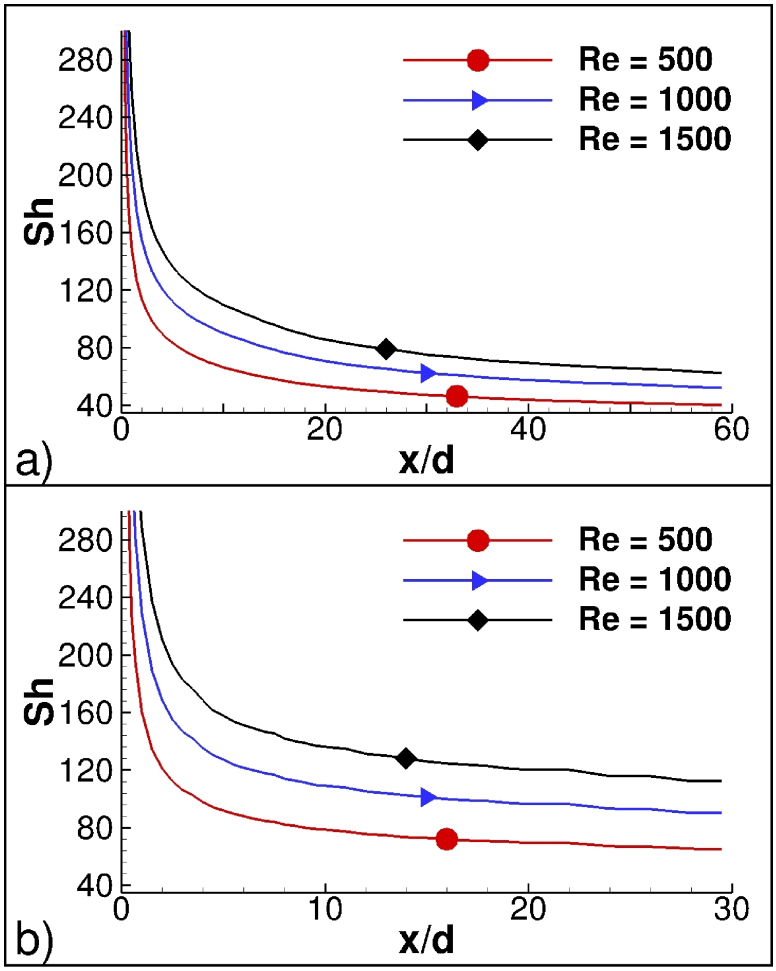

Figure 4.12: Sherwood number profiles along the stream-wise direction for the (a) straight and (b) twisted geometries. Corresponding Sherwood number for each x/d location is obtained by averaging in the azimuthal direction for all HFMs at a given cross-section.

geometry of ascending radial distances in order to characterize the effects of increasing angle of attack. The radial distance from the module center to the periphery is $r/d = 7.5$. The centermost HFM, at $r/d = 0$, and two others at $r/d = 2.5$ and $r/d = 5.0$ were examined. The defined radial distances indicate the distance between the selected HFMs center and the module center, which is normalized by the hydraulic diameter, d. The rows in Figure 4.13 and Figure 4.14, ordered from top to bottom, illustrate $Re = 500$, 1000, and 1500, respectively; the columns illustrate normalized

concentration and shear stress in Figure 4.13, and Sherwood number and vorticity magnitude in Figure 4.14.

The centermost HFM has zero angles of attack because it is concentric with the module. This is evident in Figure 4.13 by the nearly symmetric profiles the centermost HFM exhibits for all presented flow characteristics and Reynolds numbers. Nonetheless, these profiles exhibit small non-uniform fluctuations in the flow property distributions along the membrane surface. These fluctuations exist because the surrounding HFMs are slightly skewed from the flow direction, and create cross-flow velocity components that perturb flow characteristics along the centermost HFM surface. Figure 4.13 suggests that high shear and low concentration regions are highly correlated. Shear stress along the HFM surface is largest at two locations near the leading edge, where cross-flow is forced to diverge around the membrane. Both locations also exhibit decreased concentration polarization, which is critically important in industrial application and leads to fouling. At best, fouling decreases membrane performance, and at worst it stops desalinated water production altogether until the solute is removed by mechanical or chemical means. Cross-flow structures created by the twisted geometry reduce CP along the majority of the HFM surface. However, in a small region near the trailing edge, normalized concentration along the membrane surface is relatively insensitive to increasing angle of attack and radial distance for $Re = 500$ and 1000, and slightly increases for $Re = 1500$.

Sherwood number is a measure of water removal from the flow and is largest at two locations along the membrane surface near the leading edge where shearing is high, and concentration polarization is low in Figure 4.14. Sherwood number profiles from Figure 4.12 and Figure 4.14 indicate that the convoluted module geometry dramatically increases HFM performance for all membranes, and especially for those far from the module center where the angle of attack and momentum mixing is large.

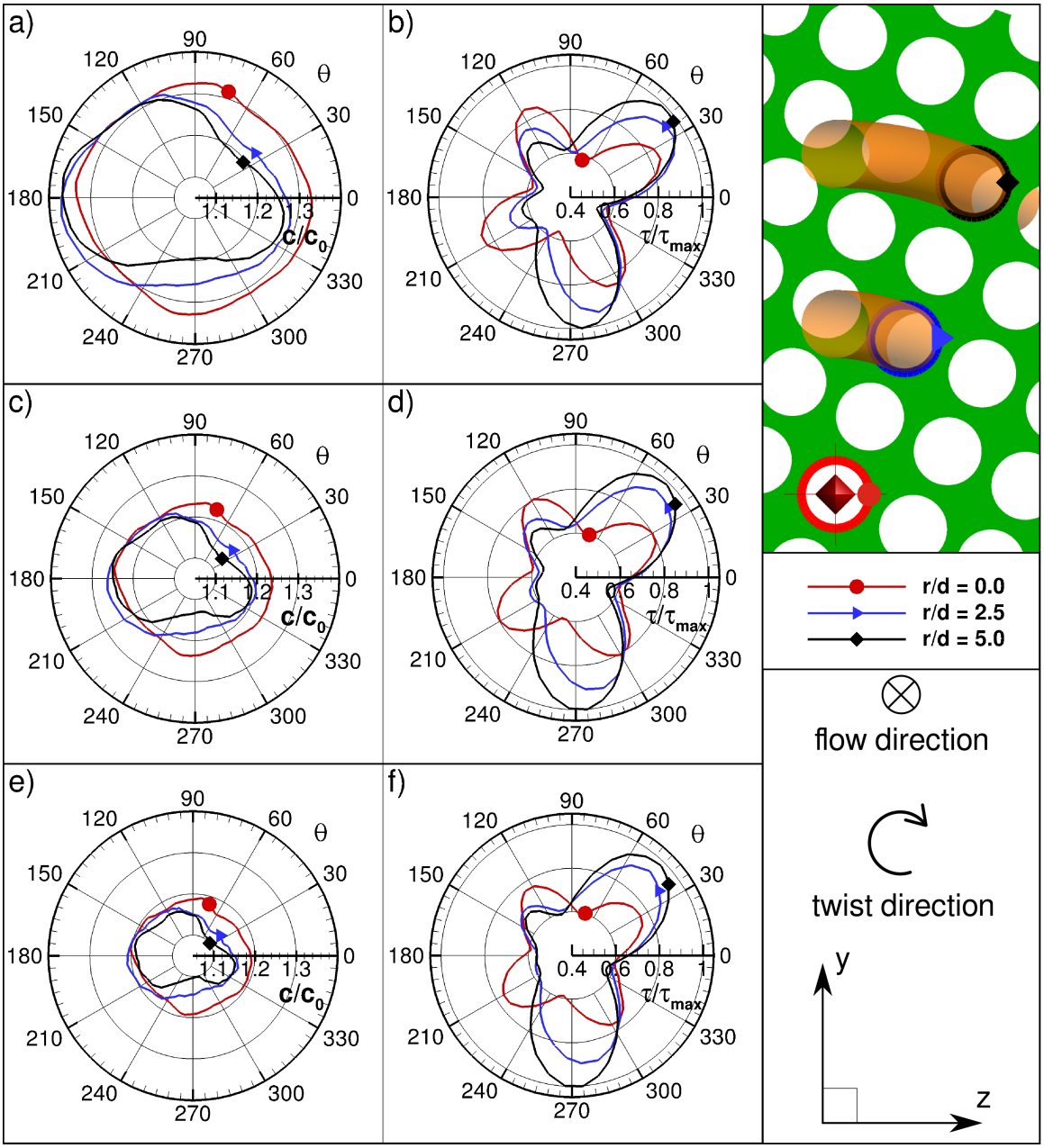

Figure 4.13: (a, c, e) Normalized concentration and (b, d, f) normalized shear stress magnitude profiles along HFM surfaces at radial distances of $r/d = 0$, 2.5, and 5.0 from the module center in the twisted geometry. Ordering from top to bottom, the rows correspond to $Re = 500$, 1000, and 1500. The selected HFM is shown in the top right corner of the figure, and the profiles are rendered at the $x/d = 25$ plane.

An HFM in the twisted geometry at a radial distance of $r/d = 5.0$ from the module center consistently outperforms a comparable HFM in the straight geometry by

more than a factor of two. Increased momentum mixing and decreased concentration polarization both contribute to a dramatic increase in permeate mass flux, indicated by the concentration and Sherwood number profiles in Figure 4.13 and Figure 4.14, respectively.

In the twisted HFM module, fibers adopt various angles of attack, which enables us to assess the performance of the module as a function of the angle of attack. The ratio of the averaged Sherwood number for HFMs away from the center to the centermost HFM is calculated to show improvement in the mass transfer coefficient. Another metric is the ratio of skin frictions that shows the increase in shear stress along HFM surfaces, which is favorable because it helps to mitigate concentration polarization and decrease the tendency of fouling. The skin friction coefficient is calculated as:

$$c_f = \frac{\tau_w}{0.5\rho U_{ave}^2} \tag{4.2}$$

where $_w$ is the average shear stress along the HFM surface, c_f is the average skin friction coefficient of all HFMs at a given radial distance from the module center in the twisted geometry. Figure 4.15 presents $\overline{Sh}/\overline{Sh_s}$ and c_f/c_{fs} as a function of the angle of attack α in degrees, which indicates HFMs of increasing radial distance. $\overline{Sh_s}$ and c_{fs} are average values for the centermost HFM in the twisted geometry. The twisted module geometry herein considered is small compared to commercially available systems, but facilitates considerable performance gains nonetheless. HFMs located only a few rows outward from the center exhibit increased mass transfer performance by $22-31\%$, which could have huge implications for commercial systems that encase thousands of HFMs. Figure 4.15b depicts the relative increase in the skin friction coefficient, c_f, as a function of the angle of attack. It is well-documented that an increased skin friction coefficient is desirable in these membrane desalination

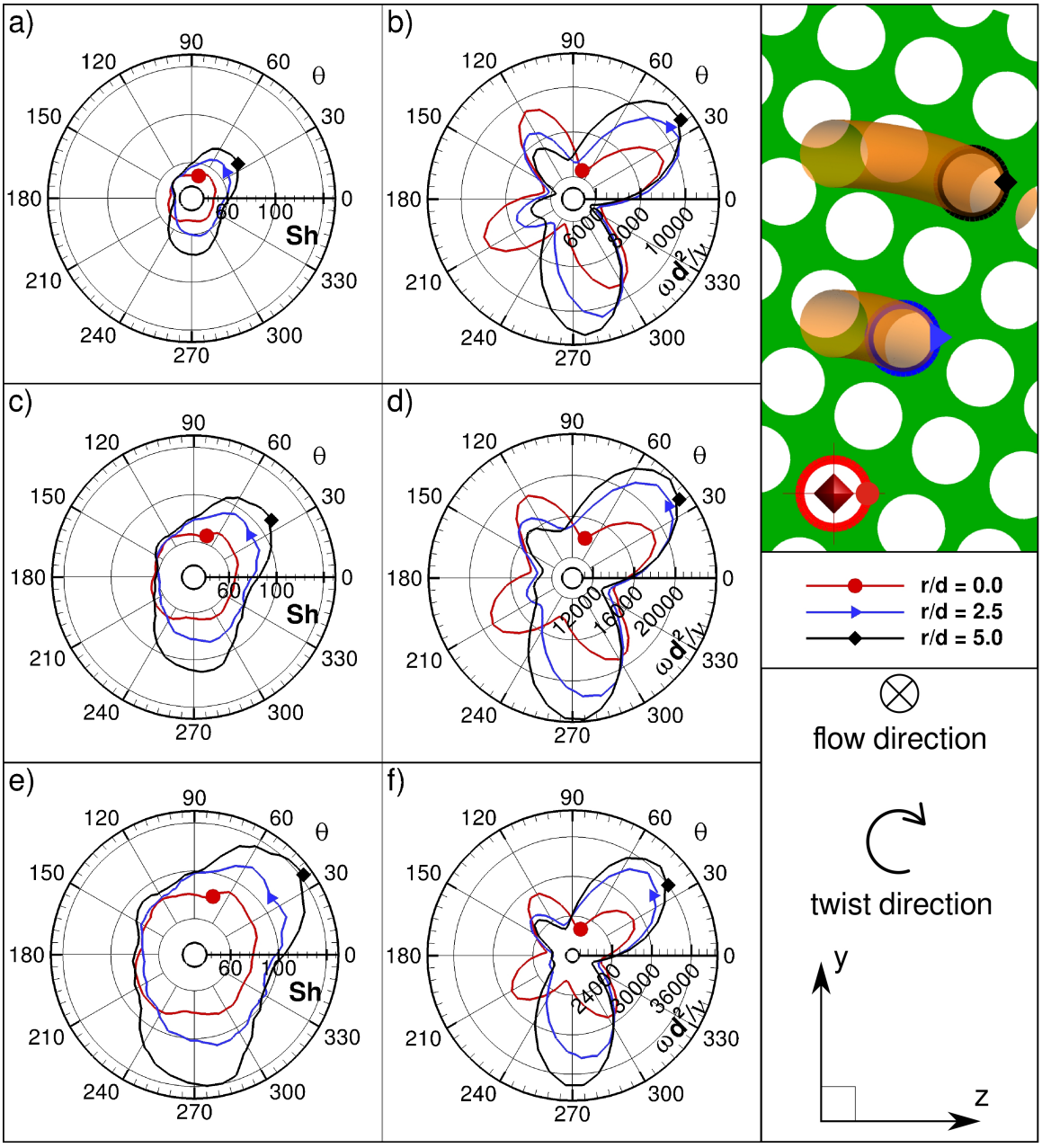

Figure 4.14: (a, c, e) Sherwood number, (b, d, f) normalized vorticity magnitude profiles along HFM surfaces at radial distances of $r/d = 0$, 2.5, and 5.0 from the module center in the twisted geometry. Ordering from top to bottom, the rows indicate the Reynolds numbers $Re = 500$, 1000, and 1500. The selected HFM is shown top right corner of the figure, and the profiles are rendered at the $x/d = 25$ plane.

systems for both mitigation of concentration polarization and fouling.

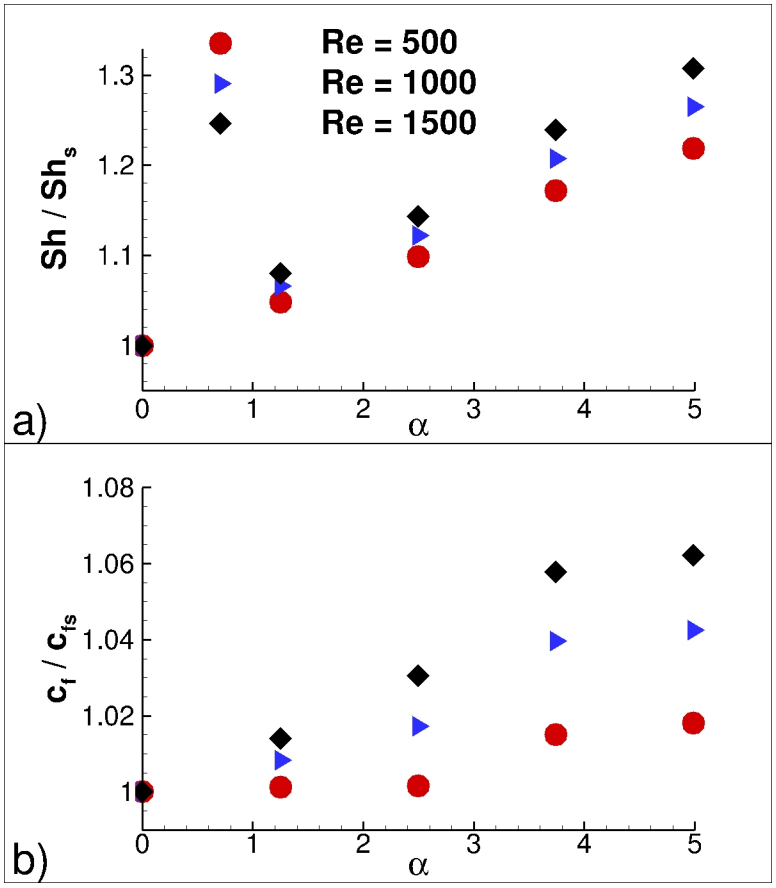

Figure 4.15: $\overline{Sh}/\overline{Sh_s}$ and c_f/c_{fs} of individual HFMs as a function of the angle of attack for $Re = 500$, 1000, and 1500. Results are depicted at the $x/d = 25$ plane.

Coefficient of Performance

Twisted HFMs are skew to the flow direction, induce swirling flow, and are effective at breaking-up isolated jet flow regions observed in the straight, co-axially aligned geometry. Separation module performance increases due to heightened momentum mixing in the twisted geometry but decreases because of elevated skin friction. Collectively, the increased skin friction accounts for a greater pressure drop along the module length in the twisted geometry. The coefficient of performance compares the

performance of both geometries relative to their required pumping power and will be presented for the entire system.

COP compares mass flux performance relative to the pressure drop along the module length for both geometries. COP is defined as:

$$COP = \left(\frac{\overline{Sh}}{\overline{Sh_s}}\right)\left(\frac{f_s}{f}\right)^{(1/3)}, \; f = \frac{d\left|\frac{\partial p}{\partial x}\right|}{0.5\rho U_{ave}^2} \tag{4.3}$$

$\overline{Sh}$ and $\overline{Sh_s}$ are the average Sherwood numbers for the twisted and straight geometries, respectively, and f and f_s are the corresponding average friction factors. In order to neglect end effects, Sherwood number and friction factor averages do not consider portions of HFMs most near to the inlet and outlet. Table 4.3 presents friction factor, Sherwood number, and COP values for the straight and twisted geometries and various flow speeds. In both geometries, friction factor decreases, and Sherwood number increases with increasing flow rate. COP calculations reveal that overall module performance increases roughly 69% for $Re = 500$ and 77% for $Re = 1500$. Although the friction factor increases in the twisted module that negatively impacts system power requirement, the elevated skin friction is still highly desirable because it offers a remedy for fouling that may extend the operational time between membrane cleaning. Therefore, our findings suggest these systems perform most optimally at high flow speeds, and that the twisted geometry far outperforms the straight, coaxially aligned geometry.

In addition to the performance evaluation based on these non-dimensional parameters, assessment can be done based on dimensional parameters such as product recovery rate, ϕ, which is defined as,

$$\phi = \frac{\dot{m}_m}{\dot{m}_i} = \frac{\int^L v_w \rho P_w dL}{\dot{m}_i} \tag{4.4}$$

Table 4.3: Tabulated results for the friction factor, averaged Sherwood number, and coefficient of performance for both the straight and twisted geometries at $Re = 500$, 1000, and 1500.

Re	Straight		Twisted		
	f_s	$\overline{Sh_s}$	f	$\overline{Sh}$	COP_s
500	0.0344	37.47	0.0413	67.21	1.69
1000	0.0181	49.71	0.0228	93.31	1.74
1500	0.0125	60.16	0.0161	116.04	1.77

where v_w is the averaged suction rate at each cross-section, ρ is the density of the product, P_w is the wetted perimeter at each cross-section, L is the module length, $\dot{m}_m$ is the product mass flow rate at the membrane surface, and $\dot{m}_i$ is the inlet mass flow rate. We calculated the ratio of the recovery rate of the twisted to the straight geometry, ϕ_t/ϕ_s , using the suction rate between $x/d = 10$ and 30, and tabulated the result in Table 4.4 for three flow rates. The recovery rate is higher in the twisted module at all flow rates with as much as 5% increase at $Re = 500$. However, the recovery rate in the short module considered in this study cannot be accurately determined.

In the region that is a few diameters away from the inlet, the suction rate linearly decreases in the stream-wise direction (see Figure 4.4). The slope of the decrease of permeation rate is directly correlated to the recovery rate of the module. Higher values of the negative slope imply lower values for the recovery rate. Hence, the recovery rate performance of the twisted and the straight modules can be better assessed by comparing the slope of the suction rate in the stream-wise direction for these short modules. Figure 4.16 presents normalized salt concentration and suction rate profiles in the stream-wise direction for the straight and twisted geometries at various Re numbers. Similar to the longer module used for the validation test, the profiles have

a steep slope near the inlet but becomes nearly constant in regions further away from the inlet. The slope is calculated to be -5.9×10^{-4} and -2.7×10^{-4} at $Re = 500$ for the straight and twisted geometries, respectively. Evidently, the twisted module has greater product recovery than the straight module.

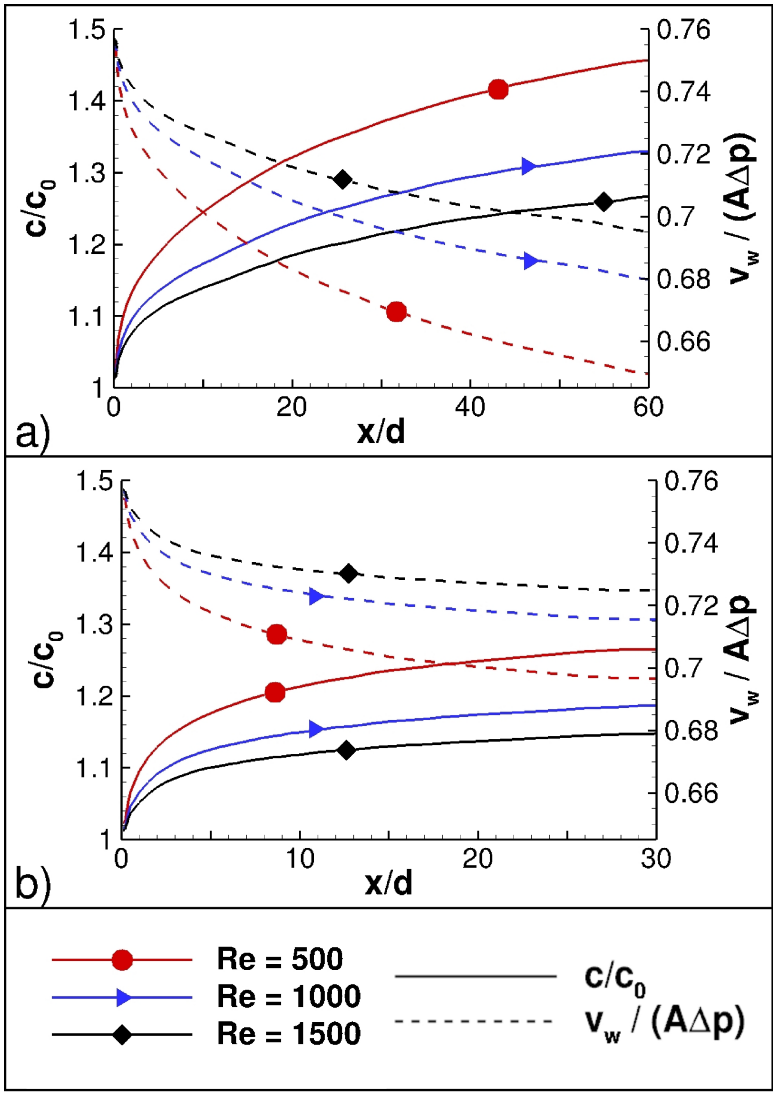

Figure 4.16: Normalized salt concentration and water suction rate profiles along the stream-wise direction for the (a) straight and (b) twisted geometries. Corresponding values for each x/d location is obtained by averaging in the azimuthal direction for all HFMs at a given cross-section.

Water permeation rate per unit area of membrane surfaces for both the straight

and twisted geometries are calculated and compared at Re = 500, 1000 and 1500 as seen in the Table 4.4. The area-averaged water permeation rate for the twisted geometry is about $5-9\%$ greater compared to that for the straight geometry. This is a clear evidence that the flux performance of the module with twisted HFMs is much greater. We expect that the performance of twisted modules employed commercially will be greater than what we report here, because those modules are much larger in the radial direction and the angle of attack for the HFMs further away from the center will be much larger.

Table 4.4: Area averaged water permeate rate (L/m^2h) for both the straight and twisted geometries, and ratios of the product recovery rate at Re = 500, 1000, and 1500.

Re	v_w (Straight)	v_w (Twisted)	ϕ_t/ϕ_s
500	67.68	73.24	1.048
1000	70.71	74.87	1.034
1500	72.73	75.66	1.028

4.1.5 Conclusion

Simulations are performed for three values of Reynolds numbers, 500, 1000, and 1500 in three-dimensional modules consisting of the twisted and straight RO HFMs. We have shown how the twisted HFM water desalination module geometry induces swirling flow structures that increase the momentum mixing throughout the module. The swirling structures add cross-flow velocity components to the existing axial-flow and disrupt jet flow regions that previously traversed the module uninterruptedly. Increased momentum mixing is evident by heightened wall shear stress and Sherwood number for the twisted geometry. Increased wall shear stress contributed to decreased concentration polarization by transporting regions of high concentration away from

membrane surfaces, which may enable prolonged operational time in commercial systems that use a twisted module design. Elevated Sherwood number and area averaged water permeation rate demonstrate increased permeate mass flux is achievable with the twisted geometry because Sherwood number is largest where swirling flow structures increased the local vorticity and suction rate along the HFM surface. Finally, we observe that individual HFM performance increases with distance from the radial center, and is greatest for higher flow rates. We predict total system performance increases roughly 70% with the twisted module geometry herein considered.

4.2 Reverse Osmosis by Hollow Fiber Membrane - Cross Flow

4.2.1 Problem Description

The three-dimensional computational flow domain representing the hollow fiber membrane bank is shown in Figure 4.17. In the present study, inline and staggered arrangements of hollow fiber membrane banks are considered with the center-to-center spacing of $2d$, where d represents the diameter of the hollow fiber membranes. The feed channel contains a bank of 3 rows and 9 columns of hollow fibers, and the height of domain is $6d$. In order to investigate the existence and the effect of secondary flows throughout the domain, the width is chosen to be two times of the height, which is $12d$. The regions of the flow domain without hollow fiber membranes upstream and the downstream of the bank have length $6d$ and $24d$, respectively, in order to minimize transient effects due to boundary conditions on hollow fiber bank region.

In this study, steady-state simulations are performed by employing the k-ω SST turbulence model and the Solution-Diffusion membrane transport model for inline and staggered arrangements and Re between 400 and 1000 resulting in four different cases. The binary solution of salt and water is assumed to be incompressible. The physical and operating parameters are selected from several studies in the field and are listed in Table 4.5.

At the inlet, a uniform stream-wise component of velocity, U_{ave}, is defined along with the inlet brackish water concentration of 4000ppm. At the outlet, a constant pressure and a constant concentration gradient is applied. Transitional periodicity is considered for the sidewalls, while a symmetric boundary is defined for the top and the bottom surfaces.

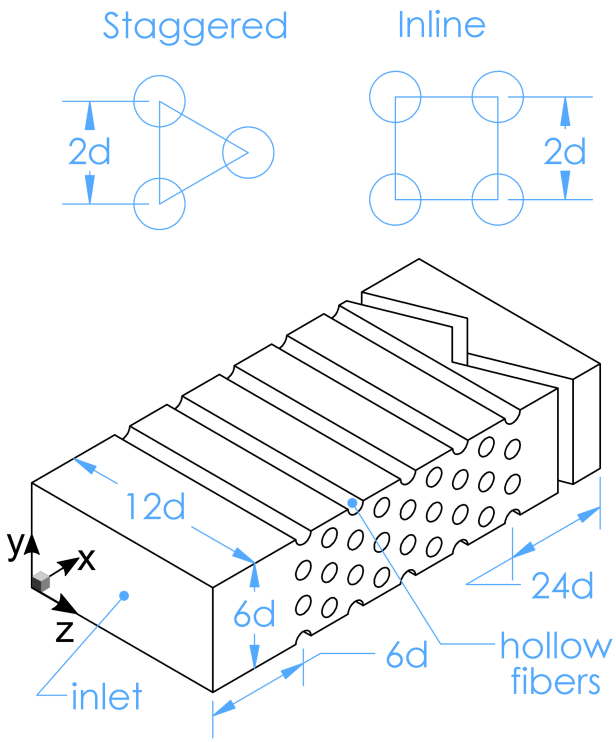

Figure 4.17: Schematic of the flow domain

Table 4.5: Physical and operating parameters used in simulations.

Parameter	**Value**	**Ref**
Density: ρ	1000 [kg/m^3]	[9]
Dynamic viscosity: μ	10^{-3} [Pa s]	[9]
Transmembrane pressure: Δp	1.25 [MPa]	[9]
Concentration in the production side: c_p	0 [ppm]	[88]
Diffusivity: D	1.5×10^{-9} [m^2/s]	[88]
Osmotic pressure coefficient: κ	75 [kPa m^3/kg]	[88]
Permeability: A	2.3×10^{-11} [m/Pa s]	[88]
Schmidt number: Sc	667 [−]	[88]

Computational fluid dynamics simulations heavily rely on selected numerical parameters such as mesh size and mesh structure, and the simulation results must be

independent of these numerical parameters. As such, the results of a well-documented mesh optimization study by the authors [9, 16] are inherited. Further, the accuracy of the selected turbulence and membrane transport models have been validated in several studies [8, 9, 16, 91].

4.2.2 Results

Figure 4.18 illustrates the normalized stream-wise velocity component iso-surfaces for $Re = 400$ and 1000 for the inline and staggered arrangements. For the inline arrangement, the flow structures are characterized by two distinct features the first being a prominent jet flow region in the stream-wise direction occupying the uninterrupted space between hollow fiber membrane rows, and the second is a distinct wake flow region between any two-consecutive hollow fiber membrane columns. For the inline configuration, both flow rates exhibit three-dimensional flow structures illustrated in Figure 4.18 that exist behind the hollow fiber membrane and vary in the z-direction. The presence of these secondary flow structures indicates that two-dimensional analysis of these systems is insufficient because crucial information about flow dynamics is neglected by ignoring variation in the z-direction. The flow in the staggered configuration is unable to traverse the hollow fiber membrane bank uninterruptedly because it is repeatedly impeded by the presence of consecutive downstream hollow fiber membranes. Therefore, the flow is subjected to repeated and rapid flow divergence, as it navigates around the impeding hollow fiber membrane, as well as subsequent flow convergence, as it is again impeded downstream. These flow phenomena induce high shear regions near the forward and backward stagnation points for the staggered arrangement.

Figure 4.19 illustrates normalized y-component vorticity iso-surfaces for both flow speeds and configurations, where the vorticity is normalized by the hydraulic diameter

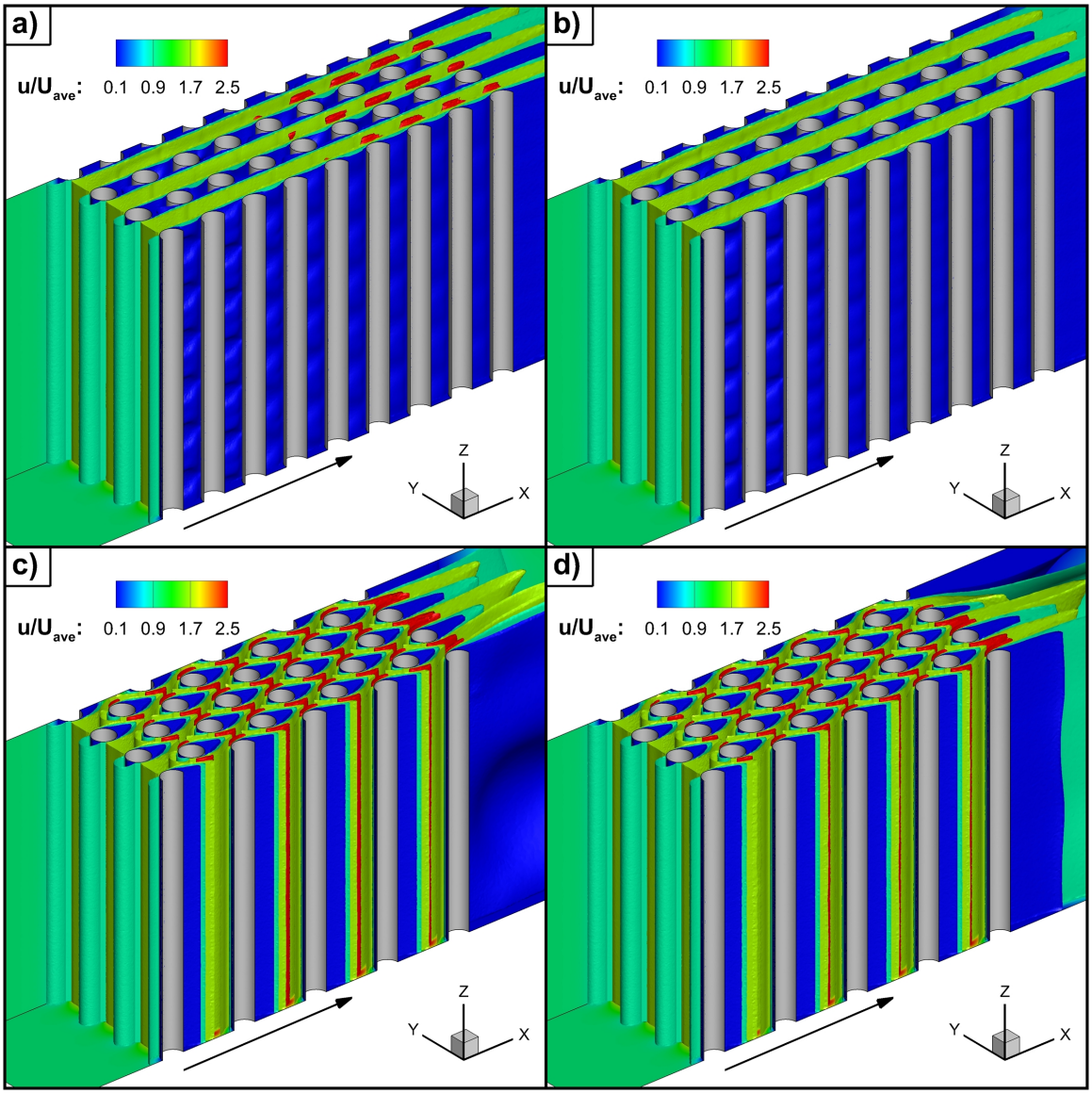

Figure 4.18: Iso-surfaces of the stream-wise velocity component for (a, b) inline and (c, d) staggered configurations. The figures to the left illustrate results for $Re = 400$, and the figures to the right depict results for $Re = 1000$.

divided by the averaged inlet velocity, d/U_{ave}. The vorticity component values illustrated in Figure 4.19 best depict the vortical effects of secondary flow structures in the hollow fiber membrane bank. For both flow speeds, the vortical structures in the inline arrangement are larger and exhibit a more deterministic periodicity as compared to the staggered arrangement. The observable vortical structures in the staggered

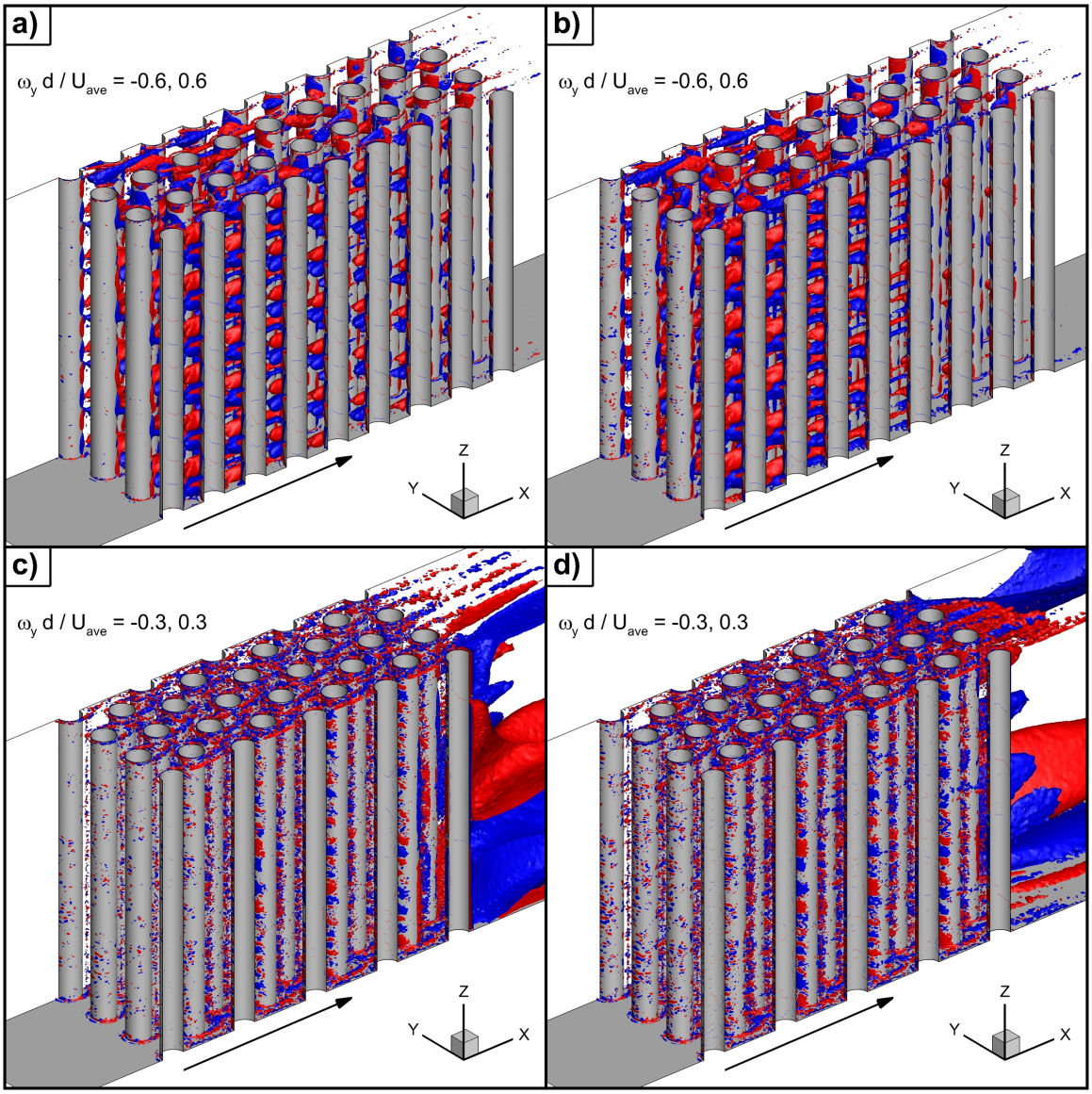

Figure 4.19: Iso-surfaces of the span-wise component of the vorticity for (a, b) inline and (c, d) staggered configurations. The figures to the left show values for $Re = 400$ and the figures to the right stand for the values of $Re = 1000$.

arrangement are significantly smaller and greater in number, which is expected since the flow through the bank is repeatedly interrupted in the staggered geometry. As the flow propagates down the flow domain, the vortical structures become more scattered and attached to the hollow fiber membrane surfaces. The presence of secondary flows is thought to increase the efficiency of these systems. Based on the vortical structures

illustrated in Figure 4.19, it is difficult to deduce if the staggered arrangement induces secondary flows, nonetheless the presence of small vortical structures indicates considerably elevated momentum mixing is achieved in the staggered arrangement, which results in scouring on the membranes surfaces. Figure 4.19a and Figure 4.19b indicate that the inline configuration exhibits a weak secondary flow in the first half of the bank region, which appears to diminish as the flow enters and propagates down the bank. Figure 4.19d and Figure 4.19c suggest that vortical activity is slightly stronger for $Re = 1000$ than for $Re = 400$, which was expected.

Figure 4.20 illustrates steady state normalized salt concentration contours along the region indicated by the red frame for inline and staggered geometries at $Re = 400$ and 1000. The salt concentration is normalized by the inlet salt concentration, and the figures are rendered at the middle of the bank at the $z = 6d$ plane. The inline geometry, shown in the left column of Figure 4.20, exhibits three distinct peaks of high concentration along the hollow fiber membrane surfaces, whereas the staggered geometry, shown in the right column of Figure 4.20, only exhibits two peaks of high concentration along the membrane surfaces for both flow speeds. Therefore, the inline geometry abets more concentration polarization along the membrane surfaces than does the staggered geometry. Examining the concentration polarization along the membrane surfaces induced by the flow structures and bank geometry provides insight into the determination of potential fouling/scaling regions, which is a great challenge in reverse osmosis technologies. Note that as the Schmidt number becomes considerably large, the concentration boundary layer thickness becomes quite thin for elevated flow speeds. For both geometries, the peak salt concentration locations along the membrane surface are similar and exist near to where boundary layer separation occurs with the exception that the inline arrangement has an additional salt concentration peak at the forward stagnation point. Lastly, as the flow speed increases

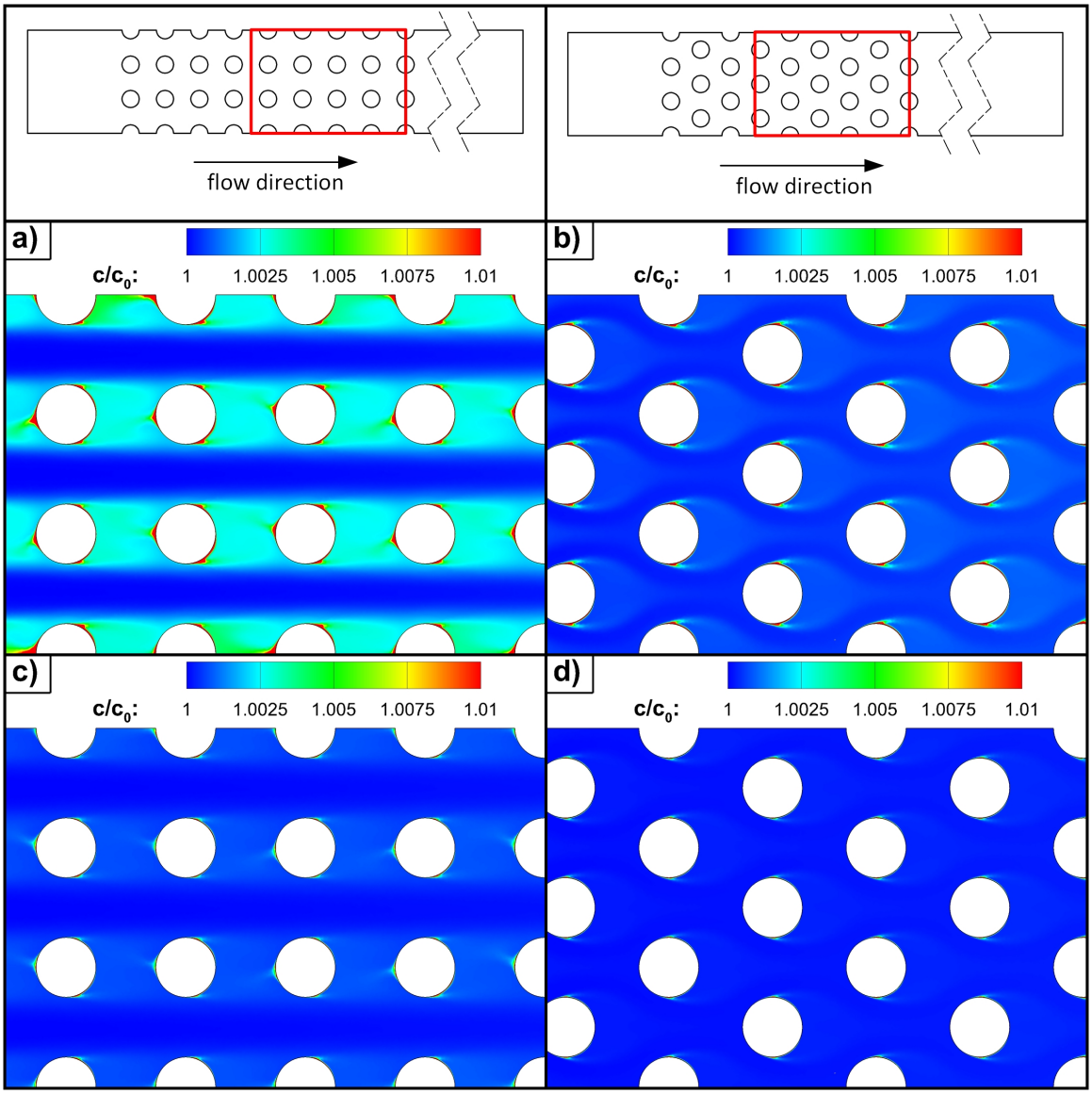

Figure 4.20: Concentration contours for (a, c) inline and (b, d) staggered configurations. (a, b) are for $Re = 400$ and (c, d) are for $Re = 1000$. The red frames in the top images indicate the bank regions illustrated in (a, b, c, d). All figures are rendered at the z=6d plane.

from $Re = 400$ to $Re = 1000$, the peak salt concentration locations do not change for both geometries, however, the prominence of the concentration polarization is lessened because the peaks diminish in size.

Figure 4.21 illustrates normalized salt concentration, local water flux, and Sher-

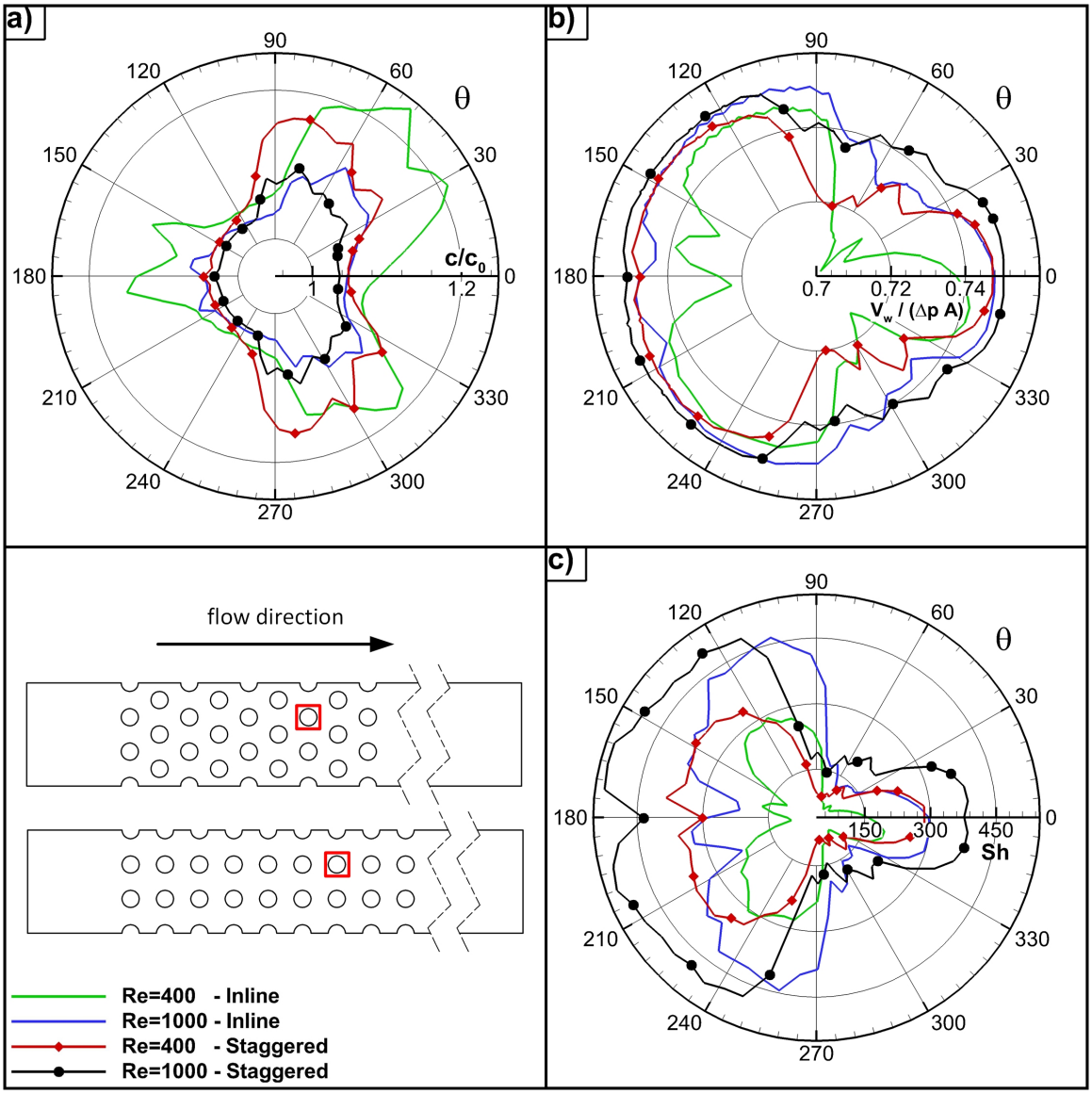

Figure 4.21: Profiles of (a) normalized concentration, (b) normalized suction rate, (c) and Sherwood number. The profiles are depicted from the indicated fibers in the bottom left at the $z = 6d$ plane in span-direction. $= 0^o$ denotes the downstream of hollow fiber.

wood number profiles, where concentration is normalized by the inlet concentration, c_0, and local water flux is normalized by $(\Delta p\ A)$. The results are depicted at the $z = 6d$ plane for the hollow fiber membrane indicated by red box in the bottom-left image of Figure 4.21. Sherwood number is calculated along the surface of hollow fiber

membranes for all cases. Sherwood number, Sh, is defined as appeared in equation (4.1).

Previously stated in the discussion of Figure 4.20, the characteristics of salt concentration polarization along the surface of the hollow fiber membranes differ depending on the arrangement of the hollow fiber membranes. Regions along the membrane surfaces that exhibit high vorticity correspond to regions of low salt concentration, shown in Figure 4.21. Further, Figure 4.21 suggests that regions of low salt concentration also correspond to regions of relatively high suction rate. Sherwood number varies between 50 and 500, and assumes the local maximum value in the vicinity of the upstream stagnation point for staggered configurations at $Re = 1000$, shown in Figure 4.21.

The Sherwood number profiles, illustrated in Figure 4.21, are a measure of the membrane flux performance, which is correlated to the local salt concentration and suction rate along the membrane surface both of which are ultimately dependent upon the hollow fiber membrane bank arrangement and flow speed. In order to obtain a more complete comparison of the performance of the various membrane arrangement and flow speed combinations, the corresponding required pumping power must be considered. The coefficient of performance (COP) resolves the membrane module performance relative to a base case. For this study, the inline arrangement is chosen to be the base case. The coefficient of performance is defined as:

$$COP = \left(\frac{\overline{Sh}}{\overline{Sh_s}}\right)\left(\frac{f_s}{f}\right)^{(1/3)} \tag{4.5}$$

where the subscript, s, indicates the averaged values of the baseline case. The overbar indicates the area averaged values, and the considered values are averaged over the area between the 5^{th} column and 8^{th} column where the flow field and concentration

distribution is developed. The friction coefficient is evaluated from:

$$f = \frac{d\left|\frac{\partial p}{\partial x}\right|}{0.5\rho U_{ave}^2} \tag{4.6}$$

where $\left|\frac{\partial p}{\partial x}\right|$ is the pressure gradient along the stream-wise direction.

Table 4.6: The average friction factor, Sherwood number, coefficient of performance, and water permeation rate [L/m^{2}h].

	Re	f	Sh	COP	v_w
Inline	400	0.35	166.1	1	75.86
	1000	0.37	280.1	1	77.08
Staggered	400	1.99	212.3	0.72	76.38
	1000	1.79	330.1	0.7	77.29

Table 4.6 shows calculated values of the averaged Sherwood number, friction factor, coefficient of performance, and averaged water permeate for various flow speeds and configurations. Sherwood number is relatively high for the staggered configuration and increases as the flow speed increases. However, the staggering arrangement continuously interrupts the flow, which increases the system friction resulting in higher required pumping power. The coefficient of performance, also referred to as the merit number, indicates that the inline configuration performs better at flow rates considered. It is also shown that the coefficient of performance is nearly the same at low and high flow rates. In accordance with this deduction, note that the COP is limited to assessing the performance based solely on mass transport parameters. It is well studied by researchers [11, 92–96] that the performance of membranes is also significantly reduced due to concentration polarization and fouling/scaling characteristics, which requires further assessment. Lastly, the water permeation rate is also slightly

improved by the increasing flow speed, but remains relatively insensitive to variations in Reynolds number.

4.2.3 Conclusion

Steady-state three-dimensional simulations of reverse osmosis driven desalination separation systems are conducted to investigate the influence of inline and staggered hollow fiber membrane bank arrangements with two different flow speeds on system performance. Mass transfer, concentration polarization, and membrane flux performance are considered. This study employed the k-ω SST momentum transport and Solution-Diffusion membrane transport models to accurately estimate the flow field, concentration distribution, and water permeation rate. This study affirms the importance of three-dimensional analysis for the velocity and concentration fields in hollow fiber membrane bank simulations.

Figure 4.20 shows the influence of membrane configurations on concentration polarization structures and locations of potential fouling/scaling regions. Figure 4.21 illustrates concentration, suction rate, and Sherwood number profiles along the surface of a specified hollow fiber membrane at a given cross-section, which reveal the interdependence of flow characteristics. Findings from Figure 4.20 and Figure 4.21 suggest that the staggered configuration exhibits less concentration polarization at higher flow speeds, as well as the low salt concentration at the membrane surface results in higher Sherwood numbers. Table 4.6 shows the relative performance of selected parameters, such as the coefficient of performance and water permeation rate the inline arrangement was considered the base case. The calculations suggest that the inline configuration at $Re = 1000$ abets the optimal coefficient of performance, while the staggered arrangement at higher flow speed indicates the optimal water permeation rate.

Chapter 5

Results of Vacuum Membrane Distillation

5.1 The Effect of Membrane Parameters on Vacuum Membrane Distillation Module Performance

5.1.1 Problem Description

This study focuses on the influence of membrane properties on the performance of VMD systems. The performance of the VMD system is directly related to PTFE membrane properties; porosity, membrane thickness, and pore radius. Membrane porosity and thickness constitute the considerable part of the Knudsen and viscous diffusion model that need to be characterized. The impact of pore radius on the diffusion is even more significant as it has a nonlinear behavior and it primarily determines the contribution of each diffusion mechanism. To elucidate the importance

of selected parameters, the simulations are carried out for fixed flow properties such as Reynolds number, feed concentration, feed temperature and vacuum pressure whereas membrane properties are varied. To compare the corresponding module performance for each set of parameters, total concentration polarization, temperature polarization and total mass flux is discussed. Further, mass flux ratios of each mechanism are determined to understand the effect of different membrane pore sizes better.

Three-dimensional CFD simulations employed for a channel featuring active flat-sheet membrane surface to investigate the sensitivity of the membrane properties to the mass transport. The area of active membrane is 10cm^2 (rectangle sizes 10×1 cm in stream-wise and span-wise directions respectively) and the feed flow channel height, h, is 1mm. Both top and bottom surface of the channel are considered as a membrane which ends up 20cm^2 active surface area in total. OpenFOAM v1706 is employed as a meshing tool and an FVM solver. For the Reynolds number of 1500, considered in this study, the flow is assumed to be laminar. The validity of this assumption can be verified from the findings reported by Tsukahara et al. [97]. Reynolds number, $Re = U_{ave}\ h/\nu$, is defined based on the channel height, h, and averaged inlet velocity, U_{ave}.

For the inlet and outlet, fixed averaged velocity, U_{ave} and fixed pressure are applied respectively. In the span-wise direction, transitional periodicity is applied to represent larger modules. At the membrane surfaces, local water flux, temperature, and concentration are coupled and following conditions, listed in equations (5.1, 5.2, 5.3) are imposed for velocity, temperature and concentration, respectively.

$$V_m = \frac{N_t}{\rho} \tag{5.1}$$

$$k_f \nabla T \cdot \vec{n} = V_m \Delta h_{fg} \tag{5.2}$$

$$D\nabla c \cdot \vec{n} = V_m c \tag{5.3}$$

Herein, V_m is the suction rate, N_t is the total mass flux, ρ is the density of water, k_f is the thermal conductivity of the feed solution, Δh_{fg} is the enthalpy of evaporation, D is the diffusivity of solute into the solvent, and $\vec{n}$ is the membrane surface normal direction.

Within this study, membrane properties pore size, porosity, and thickness are varied in a specific range while keeping rest of the flow parameters fixed to seek for an optimum set of membrane properties. Three different values of each parameter are selected results in 27 different cases. The selection of the desired values for each parameter primarily determined from the typical commercial membrane applications [98]. It is worth noting that as the pore size increases, the LEP decreases in general which requires a rigorous design consideration to prevent membrane wetting. Values of these parameters and further details about flow properties are listed in Table 5.1.

Table 5.1: Operating parameters and membrane properties.

Parameter	**Value**
Pore radius: r_p	$0.2, 0.45, 1.0$ [μm]
Thickness: δ	$120, 150, 180$ [μm]
Porosity: ε	$0.6, 0.7, 0.8$ [$-$]
Mean free path: λ	0.745 [μm]
Feed temperature: T_f	60 [^{o}C]
Saturation temperature: T_{sat}	32.87 [^{o}C]
Feed concentration: c_f	35 [kg/m^3]
Vacuum pressure: p_v	5000 [Pa]
Reynolds number: $Re = U_{ave}h/\nu$	1500 [$-$]

To discretize the computational domain structured mesh is generated. Local mesh

encryption is applied to the membrane surfaces which enables the accurate prediction of local temperature and concentration. Meshing parameters are obtained from a previous study done by present authors [11]. The validation of the implemented membrane transport model is achieved by comparing the numerical predictions with the experimental measurements for matching parameters reported by Mericq et al. [59].

5.1.2 Results

Figure 5.1 illustrates concentration polarization coefficient (CPC), φ, and temperature polarization coefficient (TPC), θ, contours at mid z-plane for one set $r_p = 1.0$, $\delta = 120$, and $\varepsilon = 0.8$ of membrane property. TPC and CPC are calculated based on equation (2.45) and (2.46), respectively.

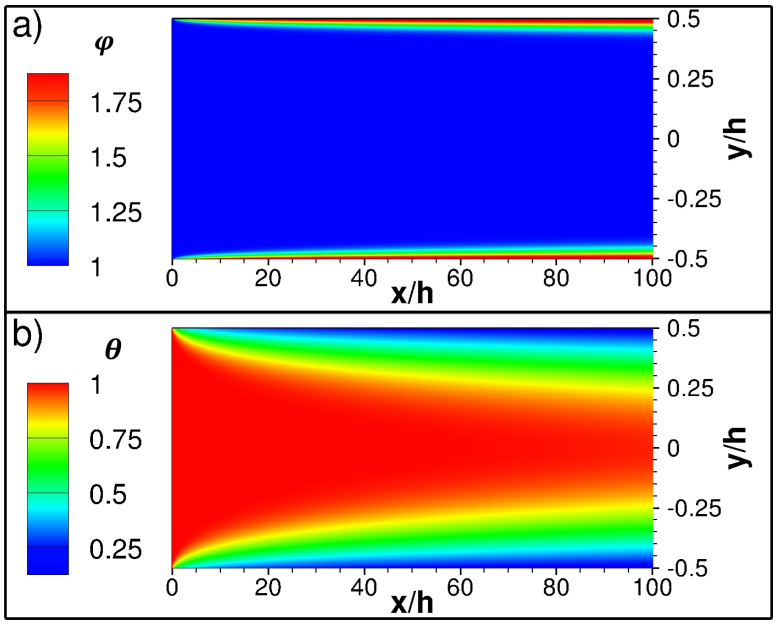

Figure 5.1: Contours of concentration polarization coefficient (a) and temperature polarization coefficient (b) for the membrane properties of $r_p = 1.0$, $\delta = 120$, and $\varepsilon = 0.8$. The contours are rendered at mid z-plane and normalized channel height, y/h, is vertically exaggerated by a factor of 50.

For better thermal and mass transfer efficiency, it is desired to obtain θ and φ values approaching unity. The CPC contour, illustrated in Figure 5.1a, shows the development of a very thin concentration boundary layer due to a high value of Schmidt number, $Sc = \nu/D$. For this relatively short channel, the bulk concentration does not elevate, and φ remains nearly unity through the module. Elevated concentration polarization near membranes decreases the partial pressure of water vapor resulting in a reduction of mass flux. The temperature polarization coefficient, presented in Figure 5.1b, is significantly lower in the region proximity to the membrane. As it approaches zero, the thermal efficiency of module decreases, and membrane becomes dysfunctional. It should not be confused that the boundary layer observed is not the actual thermal boundary layer because of difference in the definition of θ. Any level of mixing can significantly mitigate the concentration and temperature polarization and improve the mass flux performance.

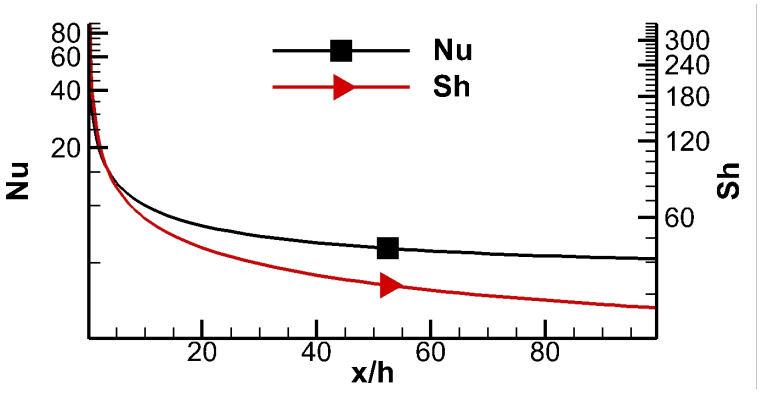

Figure 5.2: Log profiles of Sherwood number and Nusselt number along the stream-wise direction for $r_p = 1.0$, $\delta = 120$, and $\varepsilon = 0.8$.

Figure 5.2 illustrates averaged Sherwood number and Nusselt number log profiles along the stream-wise direction for the same membrane properties listed in Figure 5.1. The values are obtained by averaging both properties at each cross-section along the domain length. Sherwood number, Sh, and Nusselt number, Nu, are calculated

using the relation in equation (5.4) and (5.5), respectively.

$$Sh = \frac{h_m h}{D},\ h_m = \frac{D\nabla c \cdot \vec{n}}{c_f - c_m} \tag{5.4}$$

$$Nu = \frac{h_t h}{k_f},\ h_t = \frac{k_f \nabla T \cdot \vec{n}}{T_b - T_m} \tag{5.5}$$

Here, h_m is the local mass transfer coefficient, c_f and c_m are feed and local membrane concentration, respectively, h_t is the local heat transfer coefficient, T_f and T_m are feed and local membrane temperatures, respectively. Figure 5.2 indicates that Sherwood number and Nusselt number nearly reach asymptotic values.

To compare and discuss the differences between all 27 cases, TPC, CPC, and mass flux values are averaged along the membrane surface between $xh = 80$ and 90 omitting the development and outlet effects. The findings are discussed in Figures 5.4, 5.5, 5.6, and 5.7.

TPC, θ, and CPC, φ, profiles along the stream-wise direction are presented in Figure 5.3 for different membrane pore sizes. Figure 5.3 indicates that both TPC and CPC reaches to asymptotic value in a longer distance for the smaller pore sizes. The severity of both polarization issues is positively correlated with membrane pore size. As the pore size increases the TPC and CPC issues get even worse resulting from increased mass flux. Especially for the values of θ observed in the largest pore size, further measures in terms of design point should be considered to keep membrane module functional. Since the LEP is negatively correlated with the pore size, any improvement increasing pressure drop needs further justification. In the present study, pressure loss through the module is predicted to be between 95 and 98 [Pa] for all cases. It is inferred that increased pressure due to the losses is not significant to include in membrane wetting determination in the present study.

The averaged CPC for different sets of membrane properties is illustrated in Figure

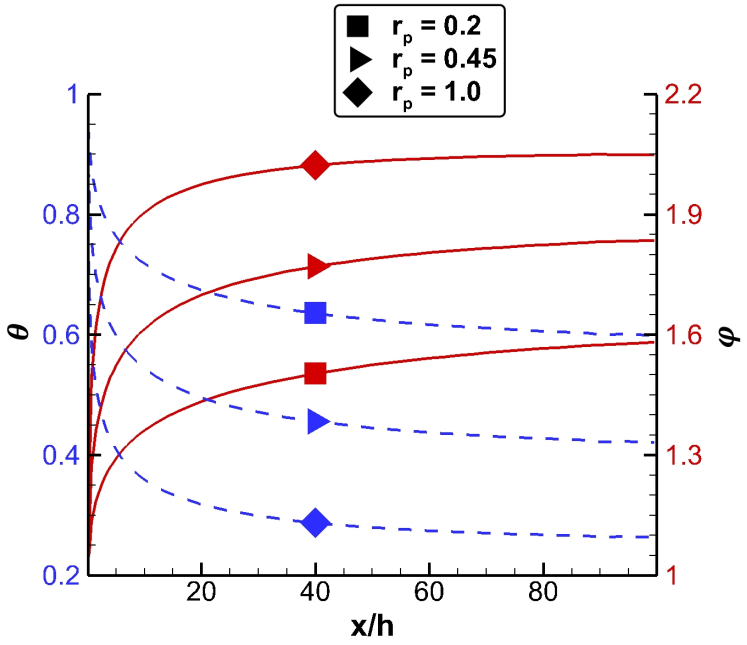

Figure 5.3: Profiles of temperature polarization coefficient, θ, (dashed line) and concentration polarization coefficient, φ, (solid line) along the stream-wise direction for different membrane pore sizes, r_p, at fixed $\delta = 120$, and $\varepsilon = 0.8$.

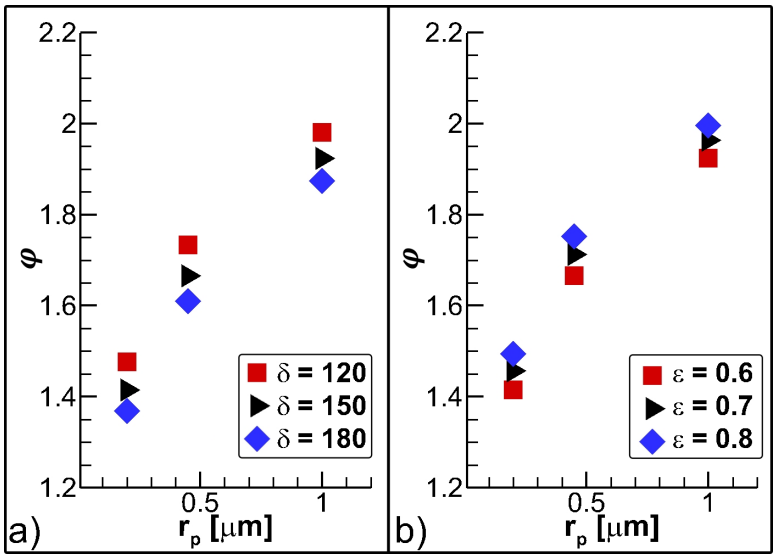

Figure 5.4: Averaged concentration polarization coefficient as a function of pore size for (a) $\varepsilon = 0.6$ and $\delta = 120$, 150, and 180 and (b) $\delta = 150$ and $\varepsilon = 0.6$, 0.7, and 0.8.

5.4. The mean value for each case is obtained by averaging φ between $x/h = 80$ and 90 along the membrane surface. Figure 5.4a presents the CPC for a fixed porosity

and varying membrane thickness. It indicates that CPC increases with decreasing membrane thickness. In Figure 5.4b the membrane thickness is kept fixed, and ϵ is varied. The values suggest that increasing porosity increases the CPC as well. However, the effect of porosity is not that significant when compared to pore size and membrane thickness.

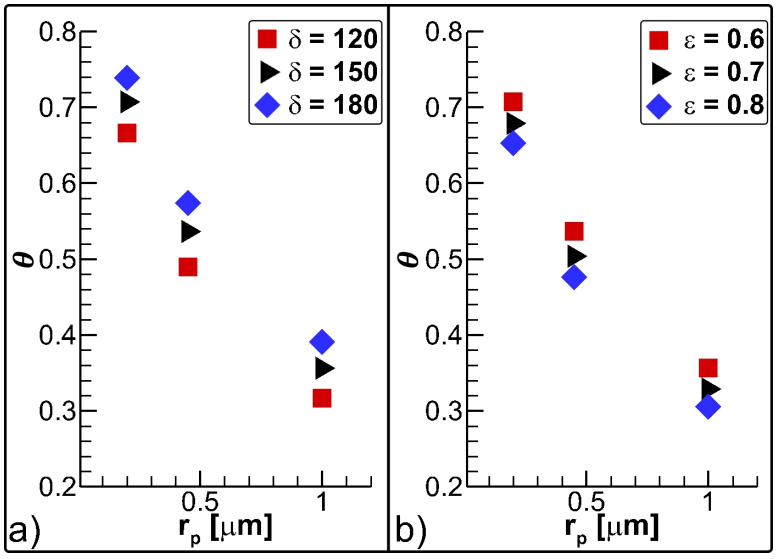

Figure 5.5: Averaged temperature polarization coefficient as a function of pore size for (a) $\varepsilon = 0.6$ and $\delta = 120$, 150, and 180 and (b) $\delta = 150$ and $\varepsilon = 0.6$, 0.7, and 0.8.

Figure 5.5 illustrates the dependence of membrane thickness and porosity to the averaged TPC for different membrane pore sizes. Evidently, the TPC is less sensitive to membrane porosity when compared to thickness. Previously stated in the discussion of Figure 5.3, the values of θ approaching to zero should be avoided. As such, the TPC will be mitigated which allows to run feed through longer modules. It is also worth adding that momentum mixing in the channel can greatly influence the performance module for larger pore size as against smaller sizes.

The averaged mass flux by means of Knudsen and the viscous mechanism is illustrated in Figure 5.6 as a function of r_p for $\varepsilon = 0.6$ and $\delta = 120$ and 150. For the selected range of membrane pore size, the ratio of pore size to mean free path, r_p/λ,

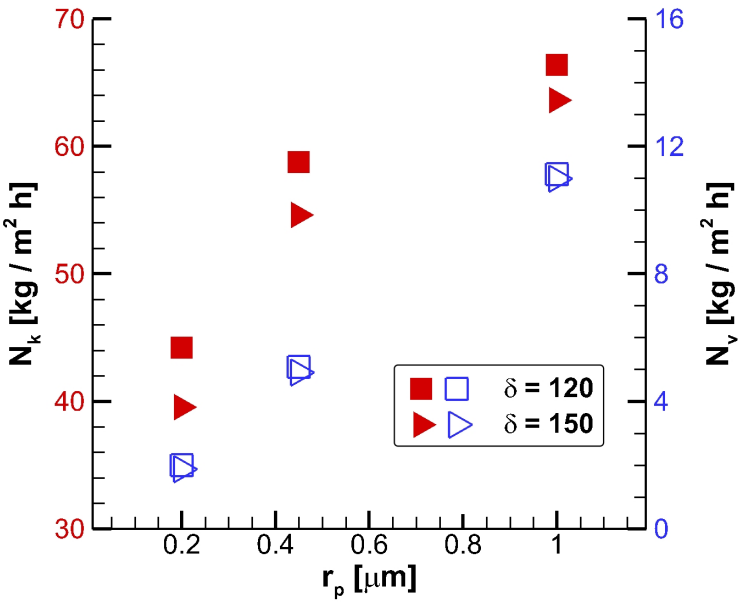

Figure 5.6: Averaged water flux through Knudsen mechanism (filled markers), N_k, and viscous mechanism (unfilled markers), N_v, as a function of r_p, $\delta = 120,\ 150$, and $\varepsilon = 0.6$.

is determined to be between 0.27 and 1.34 which is in the transitional regime means two mechanisms are occurring simultaneously. First, regarding the membrane pore size, it is observed that increasing pore size increases the flux in both mechanisms. To better understand, the ratio of viscous flux to Knudsen flux should be determined which are 4.5% and 16.8% for smallest and largest pore sizes considered in this study, respectively. Because the membrane properties are selected from typical membrane applications, such ratios show the necessity of taking both mechanisms into account while characterizing MD process. Regarding the membrane thickness, it is obvious that viscous flux is less dependent on the thickness when compared to Knudsen flux because in the viscous mechanism the mass flux is nonlinearly proportional to the pore size. As such, the impact of changing thickness is reduced when compared to the impact of pore size in the viscous mechanism.

Total averaged mass flux through the membrane is illustrated in Figure 5.7 for

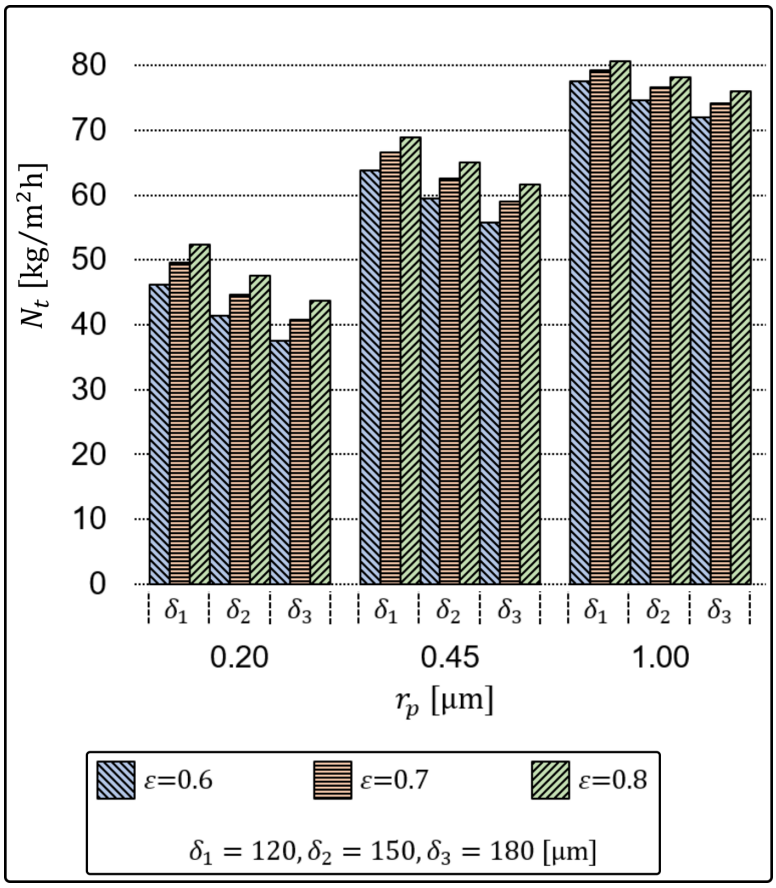

Figure 5.7: Averaged total water flux through the membrane for $\varepsilon = 0.6,\ 0.7, 0, 8,$ $\delta = 120,\ 150,\ 180,$ and $r_p = 0.2,\ 0.45,\ 1.00.$

each membrane design parameter. As expected, larger membrane pore size provides the most water flux in any scenarios varying the membrane thickness and porosity. However, it is realized that the sensitivity of the flux over the thickness and porosity is decreases as the pore size increases. This can simply be explained by the concentration and temperature polarization which are limiting the mass flux and suppressing the dependence of each parameter. From this point forth, it can be inferred that larger membrane pore size is not favorable for longer modules even if they provide better mass flux in short length unless there is a momentum mixing in the channel. Overall, Figure 5.7 suggests that the effect of membrane design parameters is not negligible. Quite the contrary, it varies the total water flux as much as by a factor of 2.

5.1.3 Conclusion

Three-dimensional laminar flow simulations are carried out in a channel containing flat-sheet membrane to investigate the impact of varying membrane design parameters on the performance of VMD modules. The simulation accurately models mass transport through the membrane by means of Knudsen and viscous diffusion. The parametric study contains a total of 27 scenarios varying membrane pore size, membrane thickness, and porosity.

The concentration polarization coefficient (CPC) and temperature polarization coefficient (TPC), are evaluated. It is found that the severity of both polarization issues increases with increasing pore size. It is shown that CPC increases with decreasing membrane thickness and, to a lesser extent, increasing porosity. Similarly, TPC is found to be less sensitive to porosity than membrane thickness or pore size.

The mass flux is also characterized for the selected membrane properties. It is found that increasing pore size increases the flux in both Knudsen and viscous diffusion mechanisms. It is also shown that the viscous flux is less dependent on the membrane thickness than Knudsen flux because of the nonlinear dependency of the viscous mechanism to the pore size. For the largest pore size, the ratio of viscous flux to Knudsen flux increases to 16.8%. Additionally, the average mass flux through the membrane is observed. It is determined that the chosen design parameters can affect the mass flux by as much as a factor of 2. It is expected that the results of this paper will provide insight into the membrane parameters that drive VMD performance and can be used as a basis for membrane design trade studies.

5.2 The Effect of Flow Parameters and Momentum Mixing on Vacuum Membrane Distillation Module Performance

5.2.1 Problem Description

The present study furthers the previous parametric study by utilizing CFD simulations to examine the influence of inlet operating conditions and feed channel geometry on VMD module performance. Specifically, feed inlet velocity and inlet temperature are evaluated for a feed channel with and without cylindrical spacers. The spacers are added to the feed channel in order to enhance momentum mixing and reduce polarization effects. To highlight the importance of selected parameters, the simulations are carried out for fixed membrane properties while the flow properties are varied. To compare the corresponding module performance for each set of parameters, total concentration polarization, temperature polarization, total mass flux, and differential pressure are evaluated. The present studies aims to provide insight into driving mechanisms behind VMD performance and provide simulation based data for system design.

The geometry used for this study is provided in Figure 5.8. Three-dimensional CFD simulations are employed on a channel featuring an active flat-sheet membrane surface to investigate the sensitivity of the VMD performance to the feed channel operating conditions. The area of active membrane is 5.2 cm^2 (rectangle sizes 6.5 $\times$ 0.8 cm in stream-wise and span-wise directions respectively) and the feed flow channel height, h, is 2 mm. Both top and bottom surface of the channel are considered as membrane which ends up 10.4 cm^2 active surface area in total. Simulations for an empty channel are compared to those for a feed channel containing cylindrical

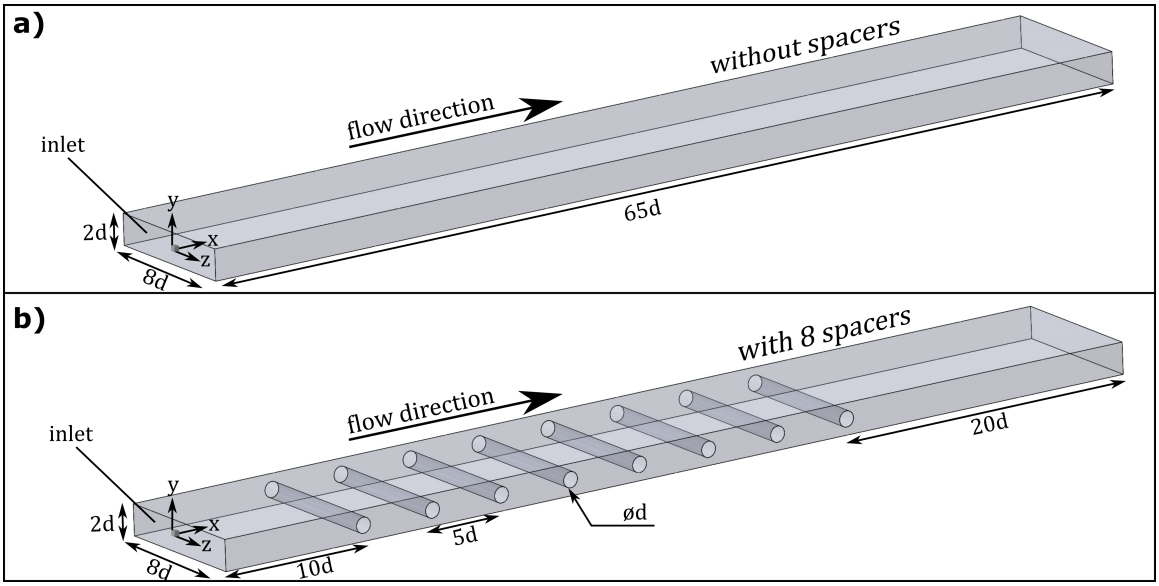

Figure 5.8: Schematic of flow geometry (a) without and (b) with spacers.

spacers. A total of 8 spacers are added to the channel to induce mixing. The spacers are placed perpendicular to the stream-wise flow direction and spaced $5d$ apart. The spacers are placed far enough from the inlet and outlet to minimize boundary effects. A structured mesh is developed in OpenFoam v1706 which is employed as a meshing tool and an finite volume method solver.

In order to accurately characterize the complex transient, three-dimensional flow in the feed channel, Large Eddy Simulations (LES) are employed. The LES model uses a filter to model the scales of motion smaller than the filter size and solves the larger eddies. The LES is used to provide time-dependent predictions to capture unsteady flow. There are different models for the sub-grid scales of motion which vary based on the application. In this study, the Wall-Adapting Local Eddy-Viscosity (WALE) subgrid-scale model is used. The WALE model allows for resolution of the near wall flow-field which is important to the present simulation.

The boundary conditions at the inlet and outlet are fixed averaged velocity, U_{ave} and fixed pressure respectively. Transitional periodicity is applied in the span-wise

direction to represent larger modules. At the membrane surfaces, local water flux, temperature, and concentration are coupled based on the Dusty Gas membrane transport model and the conditions given in equation (5.1, 5.2, 5.3) are imposed for velocity, temperature, and concentration, respectively.

For this study, the membrane properties are kept constant while the inlet temperature and velocity are varied. Values of these parameters and further details about flow properties are listed in Table 5.2.

Table 5.2: Operating parameters and membrane properties.

Parameter	**Value**
Pore radius: r_p	0.2 [μm]
Thickness: δ	179 [μm]
Porosity: ε	0.75 [$-$]
Feed temperature: T_f	$50, 80$ [$^{\circ}$C]
Saturation temperature: T_{sat}	32.87 [$^{\circ}$C] (at 5000Pa)
Feed concentration: c_f	90 [kg/m^3]
Vacuum pressure: p_v	5000 [Pa]
Reynolds number: $Re = U_{ave}h/\nu$	$200, 1000$ [$-$]

5.2.2 Spatial and Temporal Convergence

To discretize the computational domain structured mesh is generated. Local mesh encryption is applied to the membrane surfaces which enables the accurate prediction of local temperature and concentration. Additionally, similar level of mesh encryption is applied to spacers to capture the flow separation and induced momentum mixing caused by vortex generated by the spacers. In order to ensure that proper mesh discretization, a mesh convergence study is conducted. Simulations are carried out

at the $Re = 1000, T = 80$°C case since it provides the most complex flow structures. The details of the mesh parameters for this study are shown in Table 3.

Table 5.3: Mesh convergence study details.

Grid	# of Cells	1st layer thickness [mm]	y^+_{min}	y^+_{max}	y^+_{ave}
M1	284040	0.00160	0.01179	0.22629	0.11089
M2	880992	0.00123	0.00671	0.1857	0.08768
M3	1959120	0.00097	0.00606	0.14535	0.07158
M4	3726888	0.00082	0.00380	0.13618	0.06488
M5	5011776	0.00075	0.00597	0.11919	0.05940

In order to assess the adequacy of each mesh, the drag coefficient calculated on the spacer and the total mass flux through the membrane are examined. Figure 5.9a illustrates the drag coefficient on the spacer for each mesh density as a function of non-dimensional time, $\tau_i = tU_{ave}/d$. The results for each case are offset on the y-axis for visualization purposes. The drag coefficient is also time-averaged and listed on the y-axis next to the corresponding curve. Notice that for the M1 and M2 mesh, the drag coefficient is nearly periodic with time. As the mesh density is increased, the fluctuation of the drag coefficient becomes irregular as expected. The M4 and M5 mesh configurations show convergence on a drag coefficient. Figure 5.9b contains the same information as Figure 5.9a only now for the total mass flux. As with the drag coefficient, there is little change in the mass flux from the M4 mesh to the M5 mesh. Based on the mesh convergence, the M4 mesh is deemed sufficient and is utilized for the remainder of this study.

Regarding the temporal convergence, we adopted the dynamic time step adjustment by limiting the Courant number at 0.7 maximum. As this is the maximum Courant number specified, the average revolves around 0.2 depending the mesh and

flow structures. Such value is considered be sufficient enough to justify the temporal convergence.

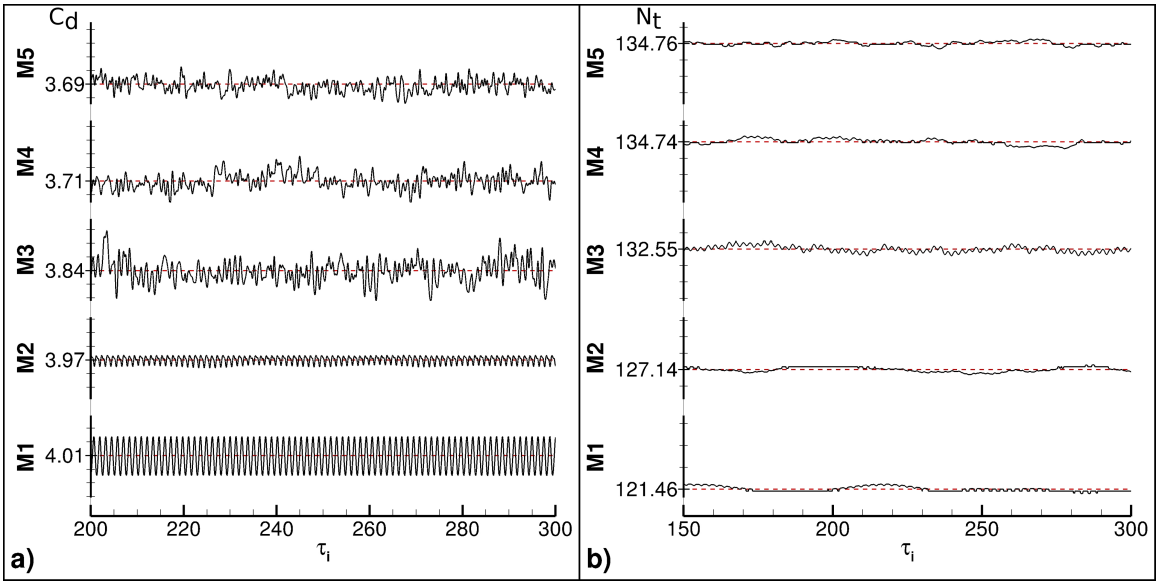

Figure 5.9: Mesh convergence results for the M1 through M5 mesh configurations, (a) drag coefficient, C_d, history and (b) total mass flux, N_t, history. The history is shown for non-dimensional time, τ_i. The average properties are indicated on y axis. The mesh density M1 = 284040, M2 = 880992, M3 = 1959120, M4 = 3726888, and M5 = 5011776.

5.2.3 Results

The focus of this study is on the performance of VMD systems with cylindrical spacers in the feed channel under four different feed channel inlet conditions. The membrane properties and operating conditions are shown in Table 5.2. Contours, profiles, and averaged values for several performance parameters are examined for each condition. The contour plots are shown to provide visual interpretation and understanding of the flow field and physics with the addition of spacers to the feed channel. This understanding is carried forward into detailed comparisons to the empty channel configuration. These latter can be used as the basis for performance

evaluations and design trade studies.

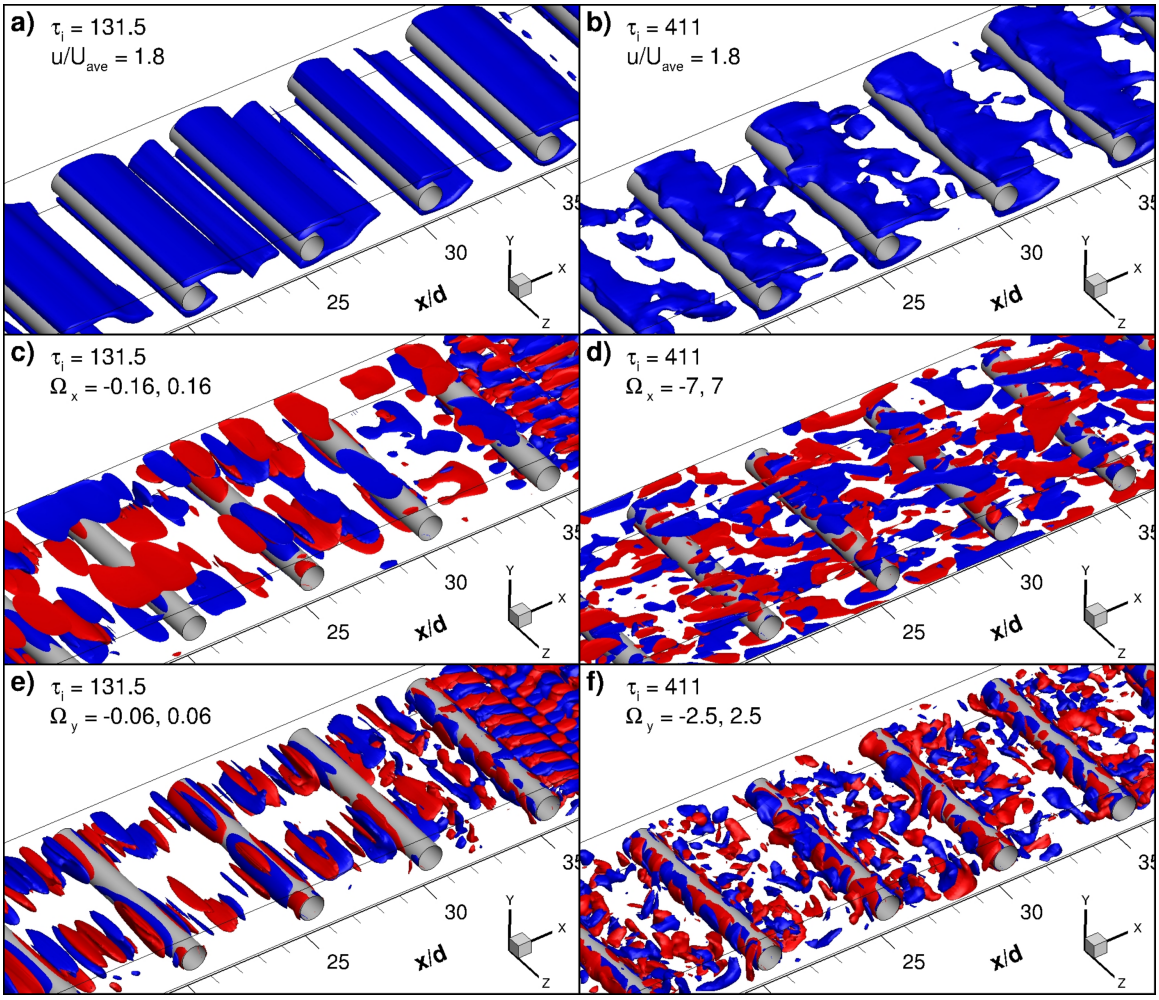

Figure 5.10: Instantaneous iso-surfaces at non-dimensional time τ_i of the stream-wise velocity (first row), x-vorticity (second row), and y-vorticity for $Re = 200$ (left column) and $Re = 1000$ (right column) at $T = 80$°C. The normalized vorticity, Ω, is obtained by $\omega/(U_{ave}/d)$.

Figure 5.10 shows instantaneous iso-surfaces of the stream-wise velocity as well as the x and y components of vorticity for the case with the inlet temperature of 80°C. x and y component of vorticity is purposely presented to illustrate the existence and strength of secondary flows. The left-hand side of the figure contains the results for Reynolds number of 200 and the right-hand side for Reynolds number of 1000. Each case shows different levels of influence of the spacers. Figure 5.10a indicates

that at lower Reynolds number the flow remains mostly two-dimensional whereas it is significantly three-dimensional at higher Reynolds number, as illustrated in Figure 5.10b. Once we take a closer look at the vorticity iso-surfaces, it is noticed that the vortical activity at lower flow speed is not so much dependent of span-wise direction agreeing the assertion made about secondary flows. As we compare the level and structure of the vorticity between Reynolds number of 200 and 1000 it is obvious that higher flow speed induce secondary flow and more of a scattered vortical structures and smaller eddies. Smaller and larger scale turbulent structures extend and reach the successive spacer; providing a good level of mixing in the entire feed channel.

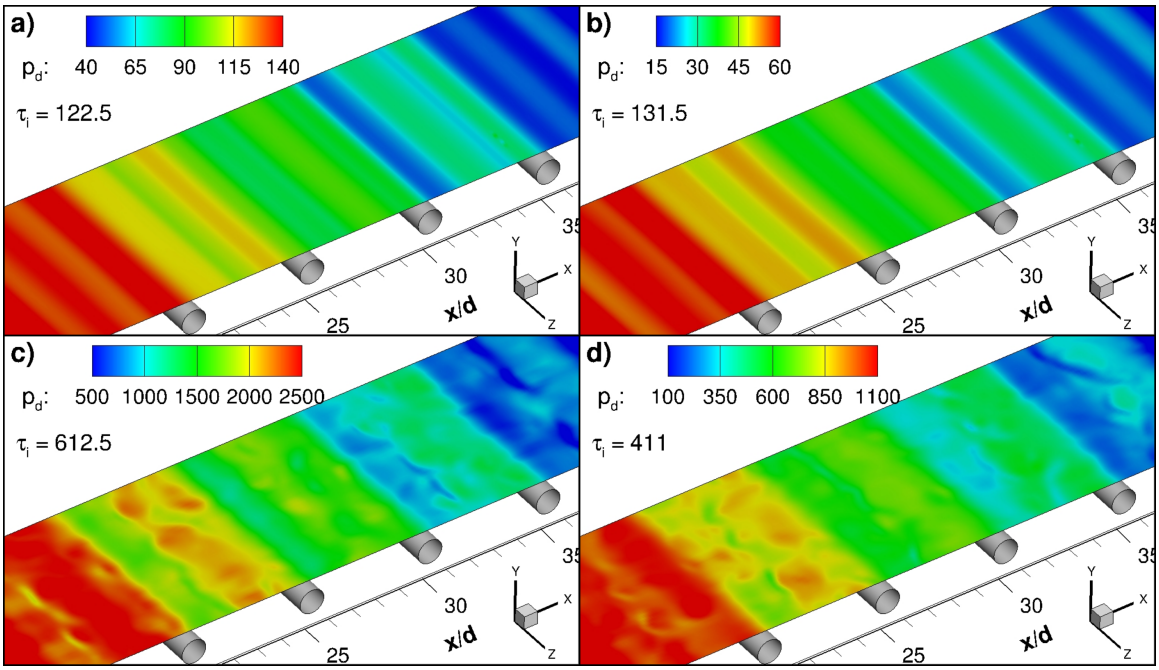

Figure 5.11: Instantaneous contours of the differential pressure on the top membrane surface at non-dimensional time τ_i with the addition of spacers for (a) $Re = 200$, $T = 50$°C (b) $Re = 200$, $T = 80$°C (c) $Re = 1000$, $T = 50$°C (d) $Re = 1000$, $T = 80$°C.

The pressure exerted on the membrane surface is an important parameter in VMD system design as it must be kept below the liquid entry pressure as defined in equation 2.32 for the system to prevent membrane wetting. The instantaneous pressure is

provided in Figure 5.11 as a differential pressure defined as

$$p_d = p_m - p_o \tag{5.6}$$

where, p_m is the pressure on the membrane surface and p_o is the outlet pressure. The pressure results are interesting as they show a significant decrease in differential pressure with increasing temperature. This decrease in differential pressure is a result of the viscosity decrease due the elevated temperature. Furthermore, higher flow rates yields to more pressure drop which increase the pressure on the membrane surface. Inclusion of spacers at higher inlet flow rates should be investigated rigorously to prevent membrane wetting.

The first performance parameters examined are the polarization coefficients. The present study uses the temperature polarization coefficient (TPC), θ, as shown in equation (2.45), to provide a quantitative evaluation of temperature polarization. TPC varies from 0 to 1 with best performance as TPC approaches unity. Lower TPC indicate a degradation in system performance. If the membrane temperature drops below the saturation temperature, the membrane becomes dysfunctional. Similarly, concentration polarization is evaluated using the concentration polarization coefficient (CPC) which is defined in equation (2.46). As with TPC, the ideal case is a CPC of unity. CPC values above unity indicate concentration elevation near the membrane surface. Such phenomenon results in a decrease in the partial pressures and corresponding decrease in mass flux through the membrane.

Figure 5.12 and Figure 5.13 show instantaneous contours of TPC and CPC respectively. Each is provided as a contour plot comparing performance for the four different operating conditions. The left-hand side of each figure shows the coefficient for the lower temperature cases ($T = 50^{\circ}$C) while the right-hand side shows the higher

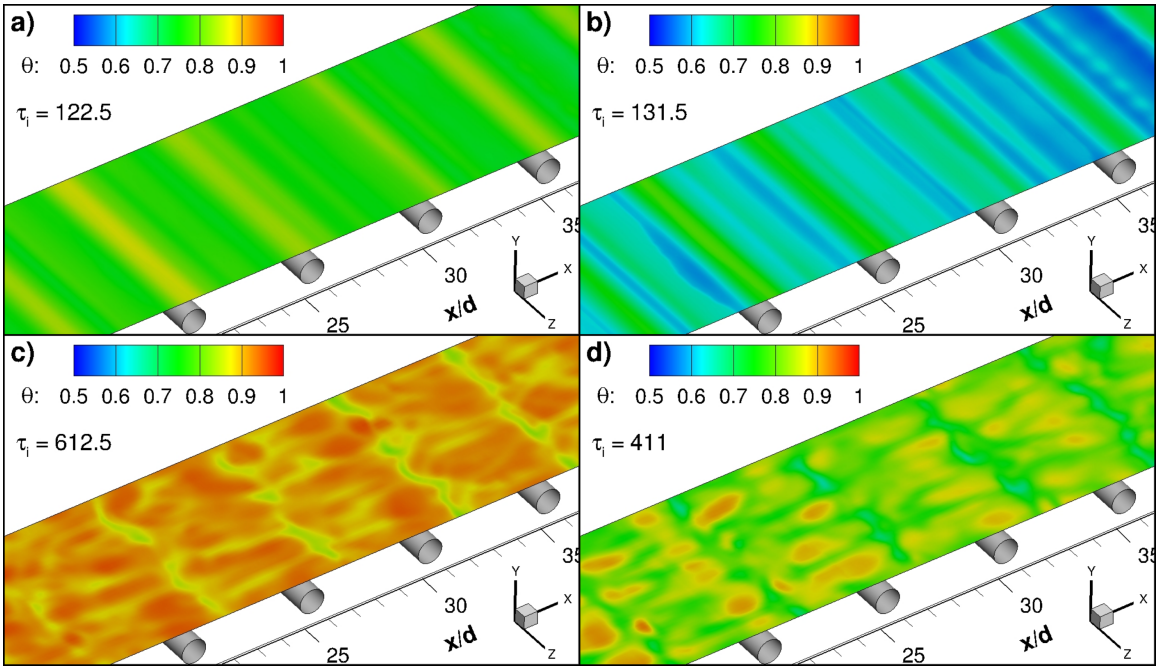

Figure 5.12: Instantaneous contours of the temperature polarization coefficient on the top membrane surface at non-dimensional time τ_i with the addition of spacers for (a) $Re = 200$, $T = 50^{o}$C (b) $Re = 200$, $T = 80^{o}$C (c) $Re = 1000$, $T = 50^{o}$C (d) $Re = 1000$, $T = 80^{o}$C.

temperature cases ($T = 80^{o}$C). The upper half of the figure provides the results for the lower Reynolds number ($Re = 200$) and the lower half contains the results for the higher Reynolds number cases ($Re = 1000$). In the low Reynolds number cases TPC decreases in the flow direction between the cylindrical spacers as well as overall along the length (Figure 5.12a and Figure 5.12b) while CPC increases (Figure 5.13a and Figure 5.13b). Each of these indicate a decrease in the performance. These decrease in coefficients are less pronounced in higher flow rate due to turbulent mixing. The presence of the cylindrical spacers does improve performance in the area directly near the spacer as the flow is disturbed and velocity increased around the cylinder. The increase in momentum mixing and the three-dimensional flow field is more readily observed in the higher Reynolds number cases. Figure 5.12c and Figure 5.12d as well as Figure 5.13c and 5.13d provide insight as to how the flow field shapes and reduces the

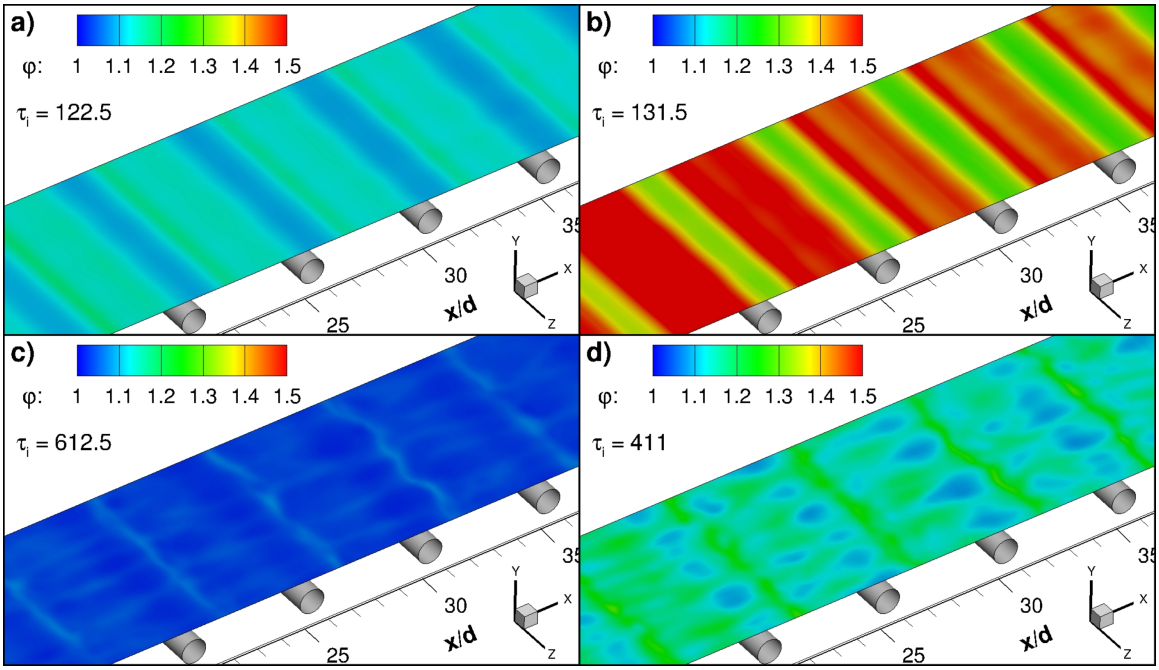

Figure 5.13: Instantaneous contours of the concentration polarization coefficient on the top membrane surface at non-dimensional time τ_i with the addition of spacers for (a) $Re = 200$, $T = 50$°C (b) $Re = 200$, $T = 80$°C (c) $Re = 1000$, $T = 50$°C (d) $Re = 1000$, $T = 80$°C.

polarization effects (increasing TPC and decreasing CPC). Additionally, it is shown that higher operating temperatures results more polarization due to increased flux. Thus higher temperature cases benefits more from the presence of spacers. Furthermore, at higher flow rates the flow becomes three-dimensional and such secondary flows contribute the mixing results in more mitigation of the both polarization.

Figure 5.14 illustrates instantaneous contours of TPC (top row) and CPC (bottom row) at three different span-wise locations and $Re = 200$ (left column), $Re = 1000$ (right column) for $T = 80$°C. When low and high Reynolds numbers are compared it is noticed that the effect of secondary flows on the temperature and concentration distribution are visible thereof they do not vary much in z-direction at lower flow speed whereas they do at higher flow speed. Concentration boundary layer thickness is lower when compared to temperature boundary layer due to significant difference

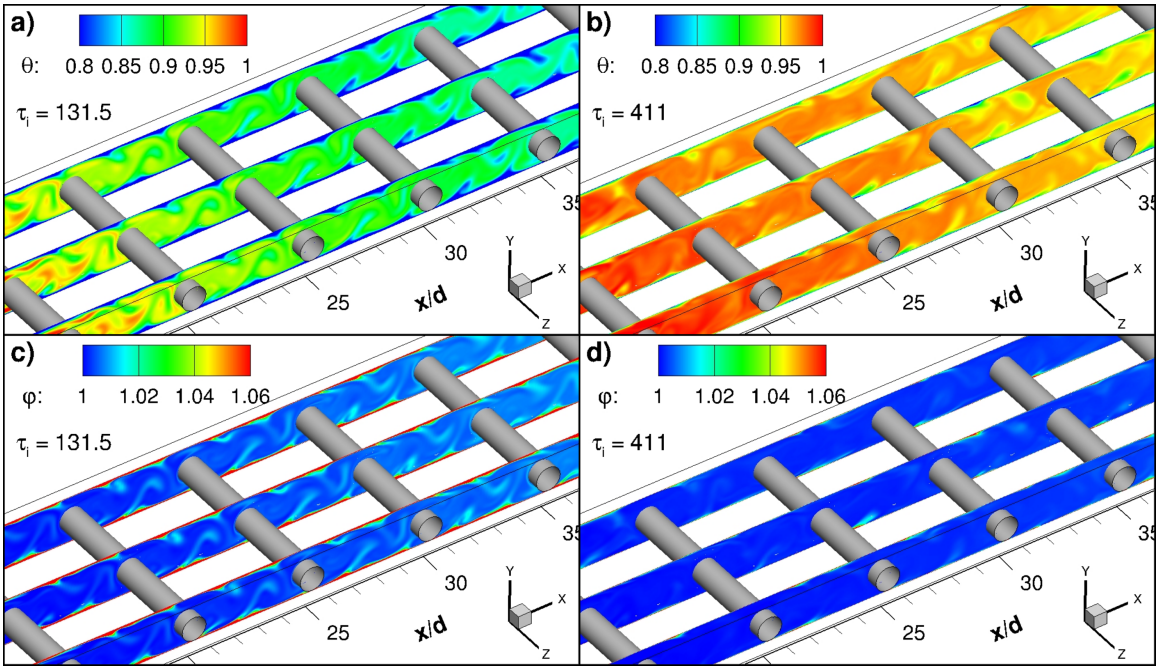

Figure 5.14: Instantaneous slices on the xy plane at non-dimensional time τ_i with the addition of spacers of the (a) temperature polarization coefficient for $Re = 200$ (b) temperature polarization coefficient for $Re = 1000$, (c) concentration polarization coefficient for $Re = 200$, (d) concentration polarization coefficient for $Re = 200$ at $T = 80$°C.

between Prandtl and Schmidt number of the feed solution ($Sc = \nu/D,\ Pr = \nu/\alpha$). Higher flow speed mitigates the concentration and temperature polarization better due to induced momentum mixing and secondary flows.

Instantaneous contours of the total mass flux, N_t, along the top membrane surface are shown in Figure 5.15 for each of the conditions studied. The total mass flux is proportional to the suction rate and as expected increases in the area adjacent to the cylindrical spacers. The total water vapor flux increases with increasing Reynolds number and increasing temperature. Note that there is a difference in scale between the right-hand and left-hand side of the graph. At higher flow speed scattered distribution of higher and lower flux indicates that higher vortical activity attached to the membrane surface decreases the polarization locally and increases the flux in turn.

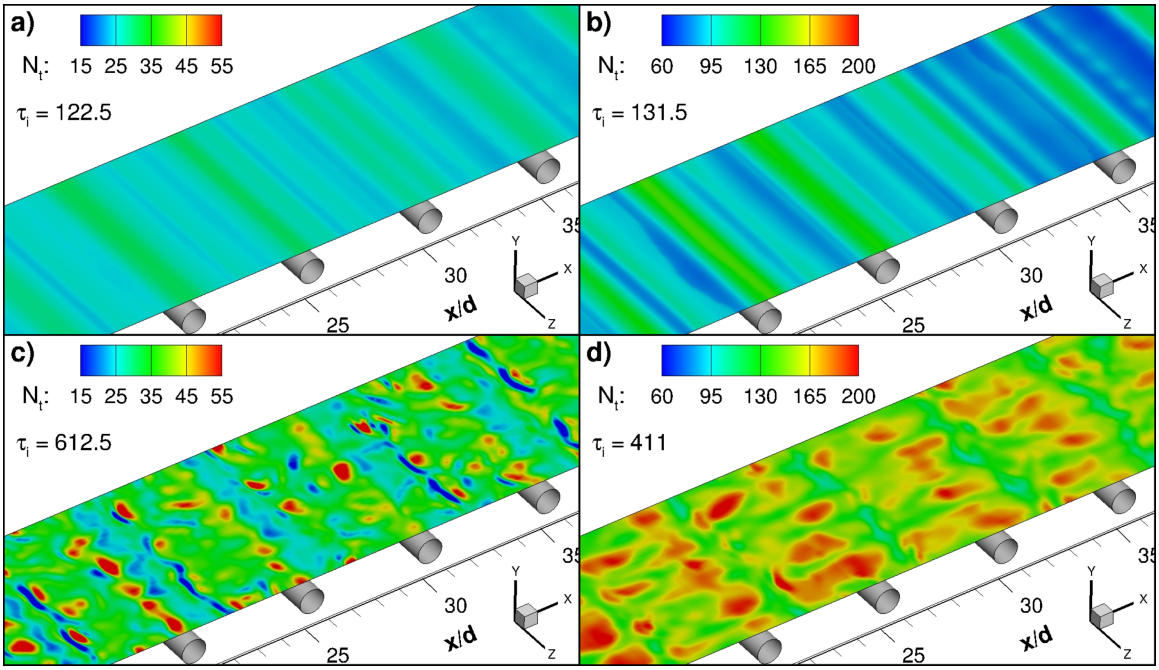

Figure 5.15: Instantaneous contours of the permeate flux through the top membrane surface at non-dimensional time τ_i with the addition of spacers for (a) $Re = 200$, $T = 50$°C (b) $Re = 200$, $T = 80$°C (c) $Re = 1000$, $T = 50$°C (d) $Re = 1000$, $T = 80$°C.

The key contribution of transient simulations can be stated that it nicely articulates how the vortical activity transported until consecutive spacer keep the permeate flux level high between spacers as well. The averaged mass flux values for all cases are illustrated in Figure 5.17.

Figure 5.16 shows the profiles of time-averaged temperature polarization, concentration polarization, total mass flux, and differential pressure along the membrane surface for all cases. It is noticed that in all properties except the differential pressure, the properties have the similar values until the flow reaches to first spacers. Right after that spacers induce desirable momentum mixing and deviates the surface properties from the ones in the channel without spacers. The TPC is more pronounced at lower Reynolds number and higher temperature, as shown in Figure 5.16a. So the effect of spacers on the mitigation of polarization observed in these cases are more

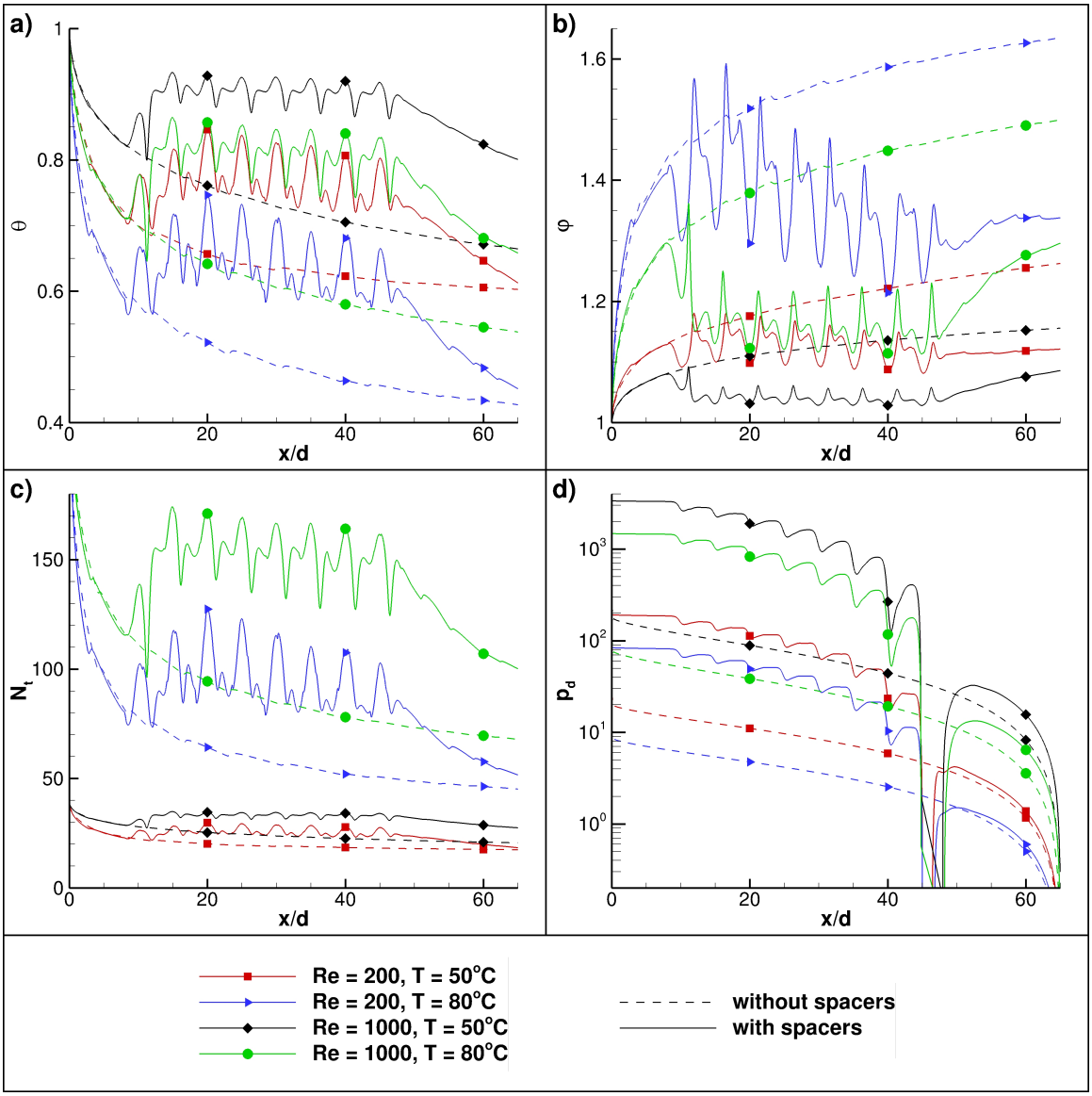

Figure 5.16: Profiles of (a) time-averaged temperature polarization coefficient, (b) concentration polarization coefficient, (c) total mass flux, and (d) differential pressure versus stream-wise direction along a line located on top membrane surface at mid-z location. The results are rendered with and without spacers for cases studied.

significant. As with the temperature polarization, concentration polarization is more pronounced at lower flow speed and higher feed temperature because of higher permeate flux. Presence of spacers substantially mitigates the concentration polarization and $Re = 1000, T = 80°\text{C}$ benefits the most from the spacers. As discussed before,

temperature substantially changes the partial pressure of water vapor so that resulting vapor fluxes are differs by 2-3 folds between high and low feed temperature, as illustrated in Figure 5.16c. Whatever we consider either relative or absolute improvement caused by the spacers, higher temperature takes the advantage of these mixer more than lower temperatures. Due to membrane wetting risk, the examination of pressure exerted on the membrane surface is also important. As shown in Figure 5.16d, the differential pressure significantly increases with the inclusion of spacers. Note that y-axis on the graph is logarithmic scaled. In the spacer cases a significant pressure drop is observed in the wake region of last spacer due to sudden expansion. Additionally, as discussed in Figure 5.11 above, the pressure drop is more significant at lower temperatures because of the temperature dependency of viscosity.

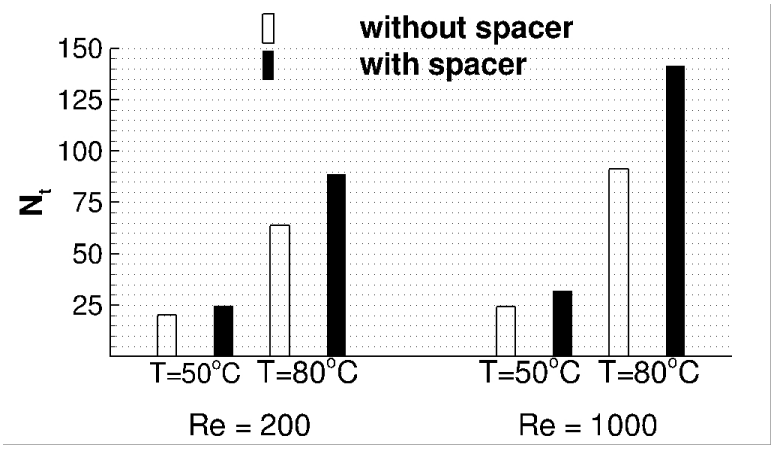

Figure 5.17: Averaged total water flux through the membrane for all 8 cases.

As it is aimed to increase the total mass flux ultimately, the examination of time-averaged total mass flux is achieved and the results for all cases are illustrated in Figure 5.17. Based on the cases considered in this study, increasing the Reynolds number from 200 to 1000 increases the flux in general and more significantly at higher temperatures. Introducing the spacers increase the flux 45% on average and 54.6% at maximum in $Re = 1000, T = 80$°C case. Such finding reveals that the spacers

tremendously affects the total mass flux as they induce momentum mixing.

5.2.4 Conclusion

Three-dimensional transient laminar and turbulent flow simulations are carried out to investigate the effectiveness of spacers on the issue of concentration and temperature polarization and on the total mass flux through the membrane. To elucidate the the effect of spacers more, different flow parameters such as feed temperature and flow rate are included in the study and time-averaged mass fluxes are compared between channel with and without spacers for all four cases.

TPC and CPC are evaluated and it is found that severity of both polarization increases with the higher temperature due to higher mass fluxes. Submerging spacers into the channel disrupts the flow and induce momentum and turbulent mixing resulting in the mitigation of polarization. The vortical structures are mostly two-dimensional and regular at $Re = 200$ whereas it is three-dimensional and scattered at $Re = 1000$. As with TPC and CPC, the total mass flux increases with the spacers and higher feed temperatures. As for the membrane wetting, the pressure applied on the membrane surface is examined and it is noticed that increasing the temperature decreases the pressure drop because of the change in the viscosity. Thus it is important to monitor pressure drop while designing these systems.

Chapter 6

Conclusion and Future Work

6.1 Conclusion

In this study, a comprehensive computational methodology is developed to investigate the transport phenomena in reverse osmosis and vacuum membrane distillation modules. Computational fluid dynamics simulations were carried in three-dimensional geometries for various module design scenarios. The simulations are designed to solve laminar/turbulent flows of incompressible, aqueous solutions in a steady or unsteady mode in accordance with the physical phenomena of the design of interest. Membrane boundaries are treated as a functional surface where Solution-Diffusion and Dusty Gas membrane transport models are employed to predict the permeate flux through the membrane in RO and VMD modules respectively. While evaluating the permeate flux, the local properties - temperature, concentration, suction rate, and pressure - are fully coupled along the membrane surface to accurately capture the transport phenomena.

Various design parameters are investigated, and possible design improvements are suggested to increase the performance of desalination modules. Particular attention

is given to the degree of momentum and turbulent mixing to address the concentration and temperature polarization issue. The features pursued in this study include concentration, temperature, the mass flow rate through the membrane, wall shear stress, Sherwood number, Nusselt number, pressure, the coefficient of performance, vorticity, velocity, temperature polarization and concentration polarization. Explicit summary of the findings is given below whereas the major findings of each study are included at the end of each preceding section.

6.1.1 Twisted RO hollow fiber membranes

A novel design adaptation by twisting the hollow fiber membrane bundle is achieved to induce momentum mixing. Depending upon the degree of convolution, a desired angle of attack between flow direction and hollow fiber membrane surface, reaching to 7.5^o for the considered geometry, is obtained whereas it was simply parallel in the existing designs. Such angle of attack gave rise to significant swirling flow motion without causing any flow separation. Thus, a desirable momentum mixing is attained while the flow is still in the laminar regime. Note that for the larger modules flow separation could occur due higher angle of attack and elevated turbulent mixing mitigates the polarization even better. Furthermore, augmented wall shear stress on the membrane surfaces also mitigates the potential fouling which increases the lifespan of the module.

As the module is convoluted by the center axis of the hollow fiber membrane bundle, each fiber experienced a unique angle of attack depending upon its distance from the center so that the performance of each individual hollow fiber membrane is characterized by the angle of attack. The elevated angle of attack increases the wall shear stress which works in aid of both concentration and fouling mitigation. With our findings, we identify how the twisted module design induces desirable flow

structures that increase membrane separation performance and HFM efficacy whereas it requires no additional component for this adaptation.

6.1.2 RO hollow fiber membranes with cross-flow

Arranging the hollow fiber membranes in a cross-flow mode causes flow separation and flow instabilities which give rise to turbulent flow structures in wake region of the HFMs at even lower Reynolds numbers. Elevated turbulent mixing mitigates the concentration polarization and increases the permeation rate. Staggered configuration of HFMs separates and merges the flow repeatedly through the bank which causes more mixing than inline configuration. Such improvement comes with an expense of additional pressure drop. The coefficient of performance which is a function of Sherwood number and friction coefficient revealed that increased Sherwood number in the staggered case was not justified by the increase in the pumping power. However this is not the only criteria for performance evaluation and staggered geometry potentially increases the membrane life span due to decreasing concentration polarization and possible fouling.

6.1.3 The effect of PTFE membrane properties

Fundamentally, membrane properties - pore size, porosity, and thickness - affect the permeate flux most. Based on the present transport model, the flux is proportional to the pore size and porosity and is inversely proportional to the thickness of the membrane. The increase in the pore size increases the flux whereas it undesirably decreases the LEP. The viscous flux is proportional to the square of pore size and the resulting flux between Knudsen, and the viscous mechanism is comparable hence both mechanism needs to be included in the modeling. Additionally, larger pore size

yield higher flux which makes the membrane prone to temperature and concentration polarization. Furthermore, membrane porosity and membrane thickness have lesser degree of impact on the mass flux when compare to pore size.

6.1.4 VMD modules containing spacers

The vacuum membrane distillation process operates in a narrow framework regarding the design parameters. This means that the feed temperature, pressure, and membrane properties have to be maintained in a certain range to keep the system operational. Throughout the feed channel, the temperature must be high enough for desired vapor pressure and it still has to be lower than the boiling temperature. The hydrophobic membrane is prone to wetting so that pressure exerted on the membrane has to be limited by liquid entry pressure which is the maximum allowable value. Regarding the membrane properties, larger pore sizes are desired for higher permeate flux whereas it also decreases the liquid entry pressure threshold which limit operational conditions. Therefore, scale up of VMD modules for industrial applications is a challenging task and requires careful optimization and design efforts.

Spacers were included in the feed channel to induce turbulent mixing to limit the severity of the temperature and concentration polarization. LES simulations revealed that the vortex structures generated by the spacers extend down to a consecutive spacer. This is an important result since it means that a similar level of the desired mixing can be obtained while increasing the distance between spacer. Increasing the distance between spacers will eventually result in lesser pressure drop. Higher feed temperatures lead to higher permeate fluxes and temperature polarization. So, the effect of spacers is more pronounced for higher temperatures. Furthermore, it was observed increasing feed temperature decreases the pressure drop due to decrease in the viscosity.

6.2 Future Work

This investigation has provided an accurate computational model to understand the complex nature of desalination by membrane separation and several design adaptations to increase the module performance. Based on the findings and interpretations, the research focus can be extended to following directions.

(i) *Fouling investigation in RO desalination.* In the present study, initial permeate flux is studied whereas the fouling of organic and inorganic molecules on the membrane surface also decreases the permeate flux after running the system for a while. The addition of an accurate fouling model will enable the examination of the system performance and the exploration of possible remedies to mitigate the fouling to increase the membrane lifespan. To understand the permeation rate reduction, molecular dynamics simulations can be carried out to determine the permeability of cake layer formed over the membrane due to the fouling.

(ii) *Concentration polarization in carbon nanotube membranes.* Concentration polarization (CP) is a central issue in the reverse osmosis desalination, and higher fluxes yield more severe CP. Recently carbon nanotube membranes have been developing and reported permeate flux based on the molecular dynamics simulations and experiments is two orders of magnitude larger than existing membranes. By implementing the developed model, severity of CP and possible remedies can be investigated.

(iii) *Optimum VMD module design to scale-up.* It was found that VMD process operates when temperature, concentration, and liquid entry pressure are in certain range and keeping those values in that range can be a significant issue for the scaled-up systems. If one of the limitations is put forward, the temperature drops considerable in the larger systems, but it should be higher than the

saturation temperature so that module operates. To address these limitations, an improved module design should be considered, and current computational model can be used to justify new designs.

(iv) *Slip boundary condition for hydrophobic membranes.* As the water does not penetrate into the hydrophobic membranes at all, a no-slip boundary condition is applied for tangential component of the velocity field. Such assumption can be relaxed by implementing a slip velocity model to predict the flow phenomenon over the hydrophobic surfaces. It is expected that the flow structures at the vicinity of the membrane will affect temperature and concentration distribution resulting in a change in the permeate flux.

(v) *Non-uniform distribution of pore radius in hydrophobic membranes.* It is observed that pore radius was the key parameter defining the transport mechanism. Any variation in the pore radius along the membrane surface may affect the total permeate flux where the membrane characteristic differs based on the manufacturing. An extended study including the non-uniform distribution of pore sizes leads to get more insight into the effect of membrane characteristics on permeate flux.

(vi) *Effect of non-circular pore radius on membrane transport mechanism.* Pore shape of the hydrophobic membranes does not necessarily to be circular whereas the current transport models adopt this simplification. Utilizing molecular dynamics simulations to investigate the effect of non-circular pore shape on the Knudsen and viscous flux will provide a solid understanding of transport mechanisms.

Bibliography

[1] Abdullah Alkhudhiri, Naif Darwish, and Nidal Hilal. Membrane distillation: a comprehensive review. *Desalination*, 287:2–18, 2012.

[2] F Moukalled, L Mangani, M Darwish, et al. *The finite volume method in computational fluid dynamics*. Springer, 2016.

[3] André Bakker. Lecture 5-solution methods applied computational fluid dynamics, 2002.

[4] Kevin W Lawson and Douglas R Lloyd. Membrane distillation. *Journal of membrane Science*, 124(1):1–25, 1997.

[5] Einar Matthiasson and Björn Sivik. Concentration polarization and fouling. *Desalination*, 35:59–103, 1980.

[6] Sandeep K Karode and Ashwani Kumar. Flow visualization through spacer filled channels by computational fluid dynamics i.: Pressure drop and shear rate calculations for flat sheet geometry. *Journal of Membrane science*, 193(1):69–84, 2001.

[7] MSMF Shakaib, SMF Hasani, and M Mahmood. Cfd modeling for flow and mass transfer in spacer-obstructed membrane feed channels. *Journal of Membrane Science*, 326(2):270–284, 2009.

[8] Ali E Anqi, Nawaf Alkhamis, and Alparslan Oztekin. Numerical simulation of brackish water desalination by a reverse osmosis membrane. *Desalination*, 369:156–164, 2015.

[9] Ali E Anqi, Nawaf Alkhamis, and Alparslan Oztekin. Computational study of desalination by reverse osmosisthree-dimensional analyses. *Desalination*, 388:38–49, 2016.

[10] Ali E Anqi, N Alkhamis, MF Alrehili, and A Oztekin. Numerical study of brackish water desalination using reverse osmosis. *Proc. IDA World Congr. Desalin. Water Reuse, San Diego*, 2015, 2015.

[11] Mustafa Usta, Ali E Anqi, and Alparslan Oztekin. Reverse osmosis desalination modules containing corrugated membranes–computational study. *Desalination*, 416:129–139, 2017.

[12] Marian G Marcovecchio, Nicolás J Scenna, and Pío A Aguirre. Improvements of a hollow fiber reverse osmosis desalination model: Analysis of numerical results. *Chemical Engineering Research and Design*, 88(7):789–802, 2010.

[13] R Ghidossi, JV Daurelle, D Veyret, and P Moulin. Simplified cfd approach of a hollow fiber ultrafiltration system. *Chemical Engineering Journal*, 123(3):117–125, 2006.

[14] A Villafafila and IM Mujtaba. Fresh water by reverse osmosis based desalination: simulation and optimisation. *Desalination*, 155(1):1–13, 2003.

[15] Afshin Pak, Toraj Mohammadi, SM Hosseinalipour, and Vida Allahdini. Cfd modeling of porous membranes. *Desalination*, 222(1-3):482–488, 2008.

[16] Ali E Anqi, Mohammed Alrehili, Mustafa Usta, and Alparslan Oztekin. Numerical analysis of hollow fiber membranes for desalination. *Desalination*, 398:39–51, 2016.

[17] Seyed Pouria Motevalian, Ali Borhan, Hongyi Zhou, and Andrew Zydney. Twisted hollow fiber membranes for enhanced mass transfer. *Journal of Membrane Science*, 514:586–594, 2016.

[18] May May Teoh, Sina Bonyadi, and Tai-Shung Chung. Investigation of different hollow fiber module designs for flux enhancement in the membrane distillation process. *Journal of membrane science*, 311(1-2):371–379, 2008.

[19] MS El-Bourawi, Z Ding, R Ma, and Mohammed Khayet. A framework for better understanding membrane distillation separation process. *Journal of membrane science*, 285(1-2):4–29, 2006.

[20] Mohamed Khayet and Takeshi Matsuura. Preparation and characterization of polyvinylidene fluoride membranes for membrane distillation. *Industrial & engineering chemistry Research*, 40(24):5710–5718, 2001.

[21] Mohamed Khayet and Takeshi Matsuura. Pervaporation and vacuum membrane distillation processes: modeling and experiments. *AIChE Journal*, 50(8):1697–1712, 2004.

[22] RW Schofield, AG Fane, and CJD Fell. Heat and mass transfer in membrane distillation. *Journal of Membrane Science*, 33(3):299–313, 1987.

[23] RW Schofield, AG Fane, CJD Fell, and R Macoun. Factors affecting flux in membrane distillation. *Desalination*, 77:279–294, 1990.

[24] RW Schofield, AG Fane, and CJD Fell. Gas and vapour transport through microporous membranes. i. knudsen-poiseuille transition. *Journal of Membrane Science*, 53(1-2):159–171, 1990.

[25] Marek Gryta and Marta Barancewicz. Influence of morphology of pvdf capillary membranes on the performance of direct contact membrane distillation. *Journal of Membrane Science*, 358(1-2):158–167, 2010.

[26] Liming Song, Baoan Li, Kamalesh K Sirkar, and Jack L Gilron. Direct contact membrane distillation-based desalination: novel membranes, devices, larger-scale studies, and a model. *Industrial & engineering chemistry research*, 46(8):2307–2323, 2007.

[27] A Mourgues, N Hengl, MP Belleville, D Paolucci-Jeanjean, and J Sanchez. Membrane contactor with hydrophobic metallic membranes: 1. modeling of coupled mass and heat transfers in membrane evaporation. *Journal of Membrane Science*, 355(1-2):112–125, 2010.

[28] M Qtaishat, T Matsuura, B Kruczek, and M Khayet. Heat and mass transfer analysis in direct contact membrane distillation. *Desalination*, 219(1-3):272–292, 2008.

[29] L Martinez and JM Rodríguez-Maroto. Effects of membrane and module design improvements on flux in direct contact membrane distillation. *Desalination*, 205(1-3):97–103, 2007.

[30] Alessandra Criscuoli, Maria Concetta Carnevale, and Enrico Drioli. Evaluation of energy requirements in membrane distillation. *Chemical Engineering and Processing: Process Intensification*, 47(7):1098–1105, 2008.

[31] Mostafa Abd El-Rady Abu-Zeid, Yaqin Zhang, Hang Dong, Lin Zhang, Huan-Lin Chen, and Lian Hou. A comprehensive review of vacuum membrane distillation technique. *Desalination*, 356:1–14, 2015.

[32] Caroliene M Guijt, Imre G Racz, Jan Willem van Heuven, Tom Reith, and AndréB de Haan. Modelling of a transmembrane evaporation module for desalination of seawater. *Desalination*, 126(1-3):119–125, 1999.

[33] GL Liu, C Zhu, CS Cheung, and CW Leung. Theoretical and experimental studies on air gap membrane distillation. *Heat and mass transfer*, 34(4):329–335, 1998.

[34] BL Pangarkar, SK Deshmukh, VS Sapkal, and RS Sapkal. Review of membrane distillation process for water purification. *Desalination and Water Treatment*, 57(7):2959–2981, 2016.

[35] Edith Hoffmann, DM Pfenning, Elke Philippsen, Petra Schwahn, M Sieber, R Wehn, D Woermann, and G Wiedner. Evaporation of alcohol/water mixtures through hydrophobic porous membranes. *Journal of membrane science*, 34(2):199–206, 1987.

[36] Grazyna Zakrzewska-Trznadel, Marian Harasimowicz, and Andrzej G Chmielewski. Concentration of radioactive components in liquid low-level radioactive waste by membrane distillation. *Journal of Membrane Science*, 163(2):257–264, 1999.

[37] MC Garcıa-Payo, MA Izquierdo-Gil, and C Fernández-Pineda. Air gap membrane distillation of aqueous alcohol solutions. *Journal of Membrane Science*, 169(1):61–80, 2000.

[38] Yanbin Yun, Runyu Ma, Wenzhen Zhang, AG Fane, and Jiding Li. Direct contact membrane distillation mechanism for high concentration nacl solutions. *Desalination*, 188(1-3):251–262, 2006.

[39] S Al-Asheh, F Banat, M Qtaishat, and M Al-Khateeb. Concentration of sucrose solutions via vacuum membrane distillation. *Desalination*, 195(1-3):60–68, 2006.

[40] Marek Gryta, Maria Tomaszewska, and Krzysztof Karakulski. Wastewater treatment by membrane distillation. *Desalination*, 198(1-3):67–73, 2006.

[41] A Criscuoli, J Zhong, A Figoli, MC Carnevale, R Huang, and E Drioli. Treatment of dye solutions by vacuum membrane distillation. *Water research*, 42(20):5031–5037, 2008.

[42] Nazely Diban, Oana Cristina Voinea, Ane Urtiaga, and Inmaculada Ortiz. Vacuum membrane distillation of the main pear aroma compound: Experimental study and mass transfer modeling. *Journal of Membrane Science*, 326(1):64–75, 2009.

[43] Zanshe Wang, Zhaolin Gu, Shiyu Feng, and Yun Li. Application of vacuum membrane distillation to lithium bromide absorption refrigeration system. *international journal of refrigeration*, 32(7):1587–1596, 2009.

[44] Zhi-Ping Zhao, Chun-Yan Zhu, Dian-Zhong Liu, and Wen-Fang Liu. Concentration of ginseng extracts aqueous solution by vacuum membrane distillation 2. theory analysis of critical operating conditions and experimental confirmation. *Desalination*, 267(2-3):147–153, 2011.

[45] Alessandra Criscuoli, Patrizia Bafaro, and Enrico Drioli. Vacuum membrane distillation for purifying waters containing arsenic. *Desalination*, 323:17–21, 2013.

[46] Jingwen Chen, Yaqin Zhang, Yafei Wang, Xiaosheng Ji, Lin Zhang, Xigeng Mi, and He Huang. Removal of inhibitors from lignocellulosic hydrolyzates by vacuum membrane distillation. *Bioresource technology*, 144:680–683, 2013.

[47] MA Izquierdo-Gil and G Jonsson. Factors affecting flux and ethanol separation performance in vacuum membrane distillation (vmd). *Journal of membrane science*, 214(1):113–130, 2003.

[48] JI Mengual, M Khayet, and MP Godino. Heat and mass transfer in vacuum membrane distillation. *International Journal of Heat and Mass Transfer*, 47(4):865–875, 2004.

[49] Na Tang, Huanju Zhang, and Wei Wang. Computational fluid dynamics numerical simulation of vacuum membrane distillation for aqueous nacl solution. *Desalination*, 274(1-3):120–129, 2011.

[50] Hui Yu, Xing Yang, Rong Wang, and Anthony G Fane. Analysis of heat and mass transfer by cfd for performance enhancement in direct contact membrane distillation. *Journal of membrane science*, 405:38–47, 2012.

[51] Hossein Hayer, Omid Bakhtiari, and Toraj Mohammadi. Simulation of momentum, heat and mass transfer in direct contact membrane distillation: A computational fluid dynamics approach. *Journal of Industrial and Engineering Chemistry*, 21:1379–1382, 2015.

[52] Lei Zhang, Jun Xiang, Peng Gao Cheng, Na Tang, Huaiyuan Han, Lina Yuan, Huanju Zhang, Songxiao Wang, and Xuekui Wang. Three-dimensional numerical simulation of aqueous nacl solution in vacuum membrane distillation process. *Chemical Engineering and Processing: Process Intensification*, 87:9–15, 2015.

[53] Boyue Lian, Yuan Wang, Pierre Le-Clech, Vicki Chen, and Greg Leslie. A numerical approach to module design for crossflow vacuum membrane distillation systems. *Journal of Membrane Science*, 510:489–496, 2016.

[54] Hsuan Chang, Jian-An Hsu, Cheng-Liang Chang, Chii-Dong Ho, and Tung-Wen Cheng. Simulation study of transfer characteristics for spacer-filled membrane distillation desalination modules. *Applied Energy*, 185:2045–2057, 2017.

[55] Aikaterini Katsandri. A theoretical analysis of a spacer filled flat plate membrane distillation modules using cfd: Part i: velocity and shear stress analysis. *Desalination*, 408:145–165, 2017.

[56] Aikaterini Katsandri. A theoretical analysis of a spacer filled flat plate membrane distillation modules using cfd: Part ii: Temperature polarisation analysis. *Desalination*, 408:166–180, 2017.

[57] Guangzhi Zuo, Guoqiang Guan, and Rong Wang. Numerical modeling and optimization of vacuum membrane distillation module for low-cost water production. *Desalination*, 339:1–9, 2014.

[58] Yonggang Zhang, Yuelian Peng, Shulan Ji, and Shaobin Wang. Numerical simulation of 3d hollow-fiber vacuum membrane distillation by computational fluid dynamics. *Chemical Engineering Science*, 152:172–185, 2016.

[59] Jean-Pierre Mericq, Stephanie Laborie, and Corinne Cabassud. Vacuum membrane distillation of seawater reverse osmosis brines. *Water Research*, 44(18):5260–5273, 2010.

[60] Jun Liu, Qin Wang, Lei Han, and Baoan Li. Simulation of heat and mass transfer with cross-flow hollow fiber vacuum membrane distillation: The influence of fiber arrangement. *Chemical Engineering Research and Design*, 119:12–22, 2017.

[61] Hendrik Tennekes, John Leask Lumley, JL Lumley, et al. *A first course in turbulence*. MIT press, 1972.

[62] Stefan Wallin and Arne V Johansson. An explicit algebraic reynolds stress model for incompressible and compressible turbulent flows. *Journal of Fluid Mechanics*, 403:89–132, 2000.

[63] Florian R Menter. Two-equation eddy-viscosity turbulence models for engineering applications. *AIAA journal*, 32(8):1598–1605, 1994.

[64] Joseph Smagorinsky. General circulation experiments with the primitive equations: I. the basic experiment. *Monthly weather review*, 91(3):99–164, 1963.

[65] James W Deardorff. A numerical study of three-dimensional turbulent channel flow at large reynolds numbers. *Journal of Fluid Mechanics*, 41(2):453–480, 1970.

[66] Franck Nicoud and Frédéric Ducros. Subgrid-scale stress modelling based on the square of the velocity gradient tensor. *Flow, turbulence and Combustion*, 62(3):183–200, 1999.

[67] Akira Yoshizawa and Kiyosi Horiuti. A statistically-derived subgrid-scale kinetic energy model for the large-eddy simulation of turbulent flows. *Journal of the Physical Society of Japan*, 54(8):2834–2839, 1985.

[68] Won-Wook Kim and Suresh Menon. A new dynamic one-equation subgrid-scale model for large eddy simulations. In *33rd Aerospace Sciences Meeting and Exhibit*, page 356, 1995.

[69] Johannes G Wijmans and Richard W Baker. The solution-diffusion model: a review. *Journal of membrane science*, 107(1-2):1–21, 1995.

[70] Tomoyuki Okada and Takeshi Matsuura. A new transport model for pervaporation. *Journal of membrane science*, 59(2):133–149, 1991.

[71] Lilian Malaeb and George M Ayoub. Reverse osmosis technology for water treatment: state of the art review. *Desalination*, 267(1):1–8, 2011.

[72] Donald R Paul. Reformulation of the solution-diffusion theory of reverse osmosis. *Journal of Membrane Science*, 241(2):371–386, 2004.

[73] C Fritzmann, J Löwenberg, T Wintgens, and T Melin. State-of-the-art of reverse osmosis desalination. *Desalination*, 216(1-3):1–76, 2007.

[74] GC Sarti, C Gostoli, and S Matulli. Low energy cost desalination processes using hydrophobic membranes. *Desalination*, 56:277–286, 1985.

[75] Bruce E Poling, John M Prausnitz, O'Connell John Paul, and Robert C Reid. *The properties of gases and liquids*, volume 5. Mcgraw-hill New York, 2001.

[76] RW Schofield. *Membrane Distillation*. PhD thesis, The University of New South Wales, 1989.

[77] Kevin W Lawson and Douglas R Lloyd. Membrane distillation. i. module design and performance evaluation using vacuum membrane distillation. *Journal of membrane science*, 120(1):111–121, 1996.

[78] Takeshi Matsuura. *Synthetic membranes and membrane separation processes*. CRC press, 1993.

[79] RD Present. *Kinetic theory of gases*. McGraw-Hill, New York, 1958.

[80] Surapit Srisurichan, Ratana Jiraratananon, and AG Fane. Mass transfer mechanisms and transport resistances in direct contact membrane distillation process. *Journal of Membrane Science*, 277(1-2):186–194, 2006.

[81] Maciej Matyka, Arzhang Khalili, and Zbigniew Koza. Tortuosity-porosity relation in porous media flow. *Physical Review E*, 78(2):026306, 2008.

[82] L Martınez, FJ Florido-Dıaz, A Hernandez, and P Pradanos. Characterisation of three hydrophobic porous membranes used in membrane distillation: modelling and evaluation of their water vapour permeabilities. *Journal of membrane science*, 203(1-2):15–27, 2002.

[83] Suhas V Patankar. A calculation procedure for two-dimensional elliptic situations. *Numerical heat transfer*, 4(4):409–425, 1981.

[84] Suhas Patankar. *Numerical heat transfer and fluid flow*. CRC press, 1980.

[85] Suhas V Patankar and D Brian Spalding. A calculation procedure for heat, mass and momentum transfer in three-dimensional parabolic flows. In *Numerical Prediction of Flow, Heat Transfer, Turbulence and Combustion*, pages 54–73. Elsevier, 1983.

[86] Raad I Issa. Solution of the implicitly discretised fluid flow equations by operator-splitting. *Journal of computational physics*, 62(1):40–65, 1986.

[87] Ruey-Hor Yen and Chen-Hua Liu. Enhancement of the simple algorithm by an additional explicit corrector step. *Numerical Heat Transfer, Part B Fundamentals*, 24(1):127–141, 1993.

[88] Shengwei Ma and Lianfa Song. Numerical study on permeate flux enhancement by spacers in a crossflow reverse osmosis channel. *Journal of Membrane Science*, 284(1-2):102–109, 2006.

[89] MNA Hawler, JC Ho, and A Malek. An experimental and analytical study of permasep b10 separation characteristics. *Journal of membrane science*, 87(1-2):1–21, 1994.

[90] Clifford K Ho, Susan J Altman, Howland DT Jones, Siri S Khalsa, Lucas K McGrath, and Paul G Clem. Analysis of micromixers to reduce biofouling on reverse-osmosis membranes. *Environmental Progress & Sustainable Energy*, 27(2):195–203, 2008.

[91] Ali E Anqi, Mustafa Usta, Mohammed Alrehili, Nawaf Alkhamis, and Alparslan Oztekin. Reverse osmosis desalination module: Three dimensional, transient analyses. In *ASME 2016 International Mechanical Engineering Congress and Exposition*, pages V007T09A033–V007T09A033. American Society of Mechanical Engineers, 2016.

[92] Sajjad H Maruf, Melissa Rickman, Liang Wang, John Mersch IV, Alan R Greenberg, John Pellegrino, and Yifu Ding. Influence of sub-micron surface patterns on the deposition of model proteins during active filtration. *Journal of membrane science*, 444:420–428, 2013.

[93] Sajjad H Maruf, Alan R Greenberg, John Pellegrino, and Yifu Ding. Fabrication and characterization of a surface-patterned thin film composite membrane. *Journal of Membrane Science*, 452:11–19, 2014.

[94] Jehad A Kharraz, MR Bilad, and Hassan A Arafat. Flux stabilization in membrane distillation desalination of seawater and brine using corrugated pvdf membranes. *Journal of Membrane Science*, 495:404–414, 2015.

[95] CP Koutsou, SG Yiantsios, AJ Karabelas, and Anastasios J Karabelas. Membrane module performance optimization using cfd simulation of flow through

narrow channels with spacers. *Proc. IDA World Congr. Desalin. Water Reuse*, pages 21–26, 2007.

[96] CP Koutsou, SG Yiantsios, and AJ Karabelas. Direct numerical simulation of flow in spacer-filled channels: effect of spacer geometrical characteristics. *Journal of membrane science*, 291(1-2):53–69, 2007.

[97] Takahiro Tsukahara, Yohji Seki, Hiroshi Kawamura, and Daisuke Tochio. Dns of turbulent channel flow at very low reynolds numbers. In *TSFP Digital Library Online*. Begel House Inc., 2005.

[98] Mohammad Mahdi A Shirazi, Ali Kargari, and Meisam Tabatabaei. Evaluation of commercial ptfe membranes in desalination by direct contact membrane distillation. *Chemical Engineering and Processing: Process Intensification*, 76:16–25, 2014.

Biography

Mustafa Usta was born in Beysehir, Turkey in 1988, the son of Meryem and Nazım Usta. After completing his work at Selcuklu High School, he attended to the Yıldız Technical University in Istanbul where he received his Bachelor of Science with honor degree in Mechanical Engineering in January 2012. Mustafa began pursuing his Master of Science in Mechanical Engineering at Lehigh University in 2013. After completing his MS degree, he kept studying at Lehigh for his Ph.D. study. During his graduate study at Lehigh, he worked both as a teaching assistant and research assistant under the supervision of Professor Alparslan Oztekin. During his time as a graduate student, Mustafa computationally studied various problems including desalination from fluid dynamics aspect and co-authored to the number of publications. Mustafa successfully defended this dissertation and graduated with the degree Doctor of Philosophy in Mechanical Engineering in August 2018.